Doctoral Dissertation

博士論文

# Studies of exoplanets

# with high resolution spectroscopy

（高分散分光による系外惑星の観測的研究）

Department of Astronomy, Graduate School of Science,
The University of Tokyo

東京大学大学院 理学系研究科

天文学専攻

Masato Ishizuka

石塚　将斗

**Abstract**

High resolution spectroscopy is one of the powerful techniques to probe the atmospheres of exoplanets. Since the radial velocity of the planet changes rapidly during the observations due to the planet's orbital motion, it is possible to distinguish the planetary signal from other signals such as stellar spectrum or telluric absorption. The cross-correlation technique enables us to sum up all weak signals of the planetary atmospheres effectively and leads to robust detection of chemical species. Chemical species in the planetary atmospheres are important information to understand formation processes and atmospheric structure of exoplanets. Fortunately, the line lists of various species have been constantly improved till now. Therefore, now is the good timing to employ high resolution spectroscopy to study exoplanetary atmospheres.

The aim of this thesis is to characterize atmospheres of hot-Jupiters. Hot-Jupiters are a class of exoplanets which do not exist in our solar system. Owing to the high temperature and inflated atmospheres, hot-Jupiters are suitable for studies of planetary atmospheres. Particularly, hotter hot-Jupiters (called Ultra Hot-Jupiters, UHJs) are promising targets because their extremely high temperatures hinder cloud formation. The formation processes and atmospheric structure of hot-Jupiters are still not understood well. Thus hot-Jupiters are important targets to understand planetary formation and atmospheric structure of exoplanets. Transmission spectrum is not sensitive to the temperature strucuture of planetary atmospheres, therefore transmission spectroscopy is an appropriate method to investigate the chemical composition of planetary atmospheres.

In this thesis, we present results of high resolution transmission spectroscopy for UHJs in two systems at visible wavelengths. The targets are HD149026b and WASP-33b. We remove the systematic components in the transmission spectra to search for weak planetary signals. We also make the model transmission spectra of several neutral metals and molecular species and calculate the cross-correlation of the residual and model spectra to search for chemical species. We have detected a signal of neutral titanium and a marginal signal of neutral iron in the atmosphere of HD149026b. Assuming chemical equilibrium, titanium tends to form titanium oxide (TiO) at the expected atmospheric temperature of HD149026b. The non-detection of TiO implies a supersolar C/O ratio, which suggests that HD149026b was formed outside the $H_2O$ snowline and migrated to the current orbit.
On the other hand, we have detected TiO in the atmosphere of WASP-33b. Due to the variable line profile of the central star, it is difficult to search for metals in the atmosphere of WASP-33b. This is because there are also absorption lines of metals in

the spectrum of the central star. Thus, we focus on TiO for WASP-33b. Since there has been a problem of line list accuracy for TiO, we use three kinds of TiO line lists and check the accuracy of them with an M-dwarf spectrum. Two line lists provided by Plez (1998) and McKemmish et al. (2019) are confirmed to be accurate at visible wavelengths, and we detect TiO with the two line lists. Our results strongly support the previous detection of TiO by Nugroho et al. (2017), which reported the detection of TiO in the dayside thermal emission spectrum of WASP-33b. Since transmission spectroscopy probes the terminator region atmosphere, TiO is likely to be widely distributed in the atmosphere of WASP-33b combined with the previous detection by Nugroho et al. (2017). TiO has been considered as a key molecule for thermal inversion in the atmosphere of hot-Jupiters, though there are only a few examples of detection. Considering the detection of emission lines of TiO by Nugroho et al. (2017), our robust detection of TiO by transmission spectroscopy shows that TiO really exists in planetary atmospheres and cause thermal inversion.

Our results show the rich diversity of atmospheres of hot-Jupiters combined with previous studies of hot-Jupiters, especially recent high resolution spectroscopy of UHJs. Our results also prove the capability of high resolution spectroscopy to characterize exoplanetary atmospheres. Investigation of metal and their compounds is a promising approach to study exoplanetary atmospheres, because their abundance reflects atmospheric environments such as temperature or C/O ratio. Future extremely large telescopes and/or improvement of the accuracy of molecular line lists will enable us to observe fainter hot Jupiters and more various lines and thus to understand exoplanetary atmospheres more comprehensively.

# Contents

# List of Figures

*LIST OF FIGURES*

# List of Tables

# Acknowledgments

# Chapter 1

# Introduction

In 1995, a planet orbiting a main-sequence star was firstly discovered (Mayor & Queloz 1995). From that time on, this science field has developed rapidly. Figure1.1 shows the mass and orbital period of exoplanets discovered so far. More than 4000 exoplanets have been discovered, and several unique methods have been developed to observe exoplanets. In this section, we introduce how to detect and characterize exoplanets.

## 1.1 Detection Methods of Exoplanets

### 1.1.1 Radial Velocity Method

The first exoplanet around a main-sequence star was discovered with the radial velocity method. Both the star and the planet orbit around their common center of mass, thus we can detect unseen planets by measuring periodical radial velocity variation of the star. The semi-amplitude of radial velocity variation of the star $K_s$ is

$$K_s = \frac{M_p \sin i}{\sqrt{1 - e^2}} \sqrt{\frac{G}{(M_p + M_s)a}} \tag{1.1}$$

where $M_p$ and $M_s$ is the mass of the planet and the star, respectively, $e$ and $a$ is the eccentricity and semi-major axis of the planetary orbit, respectively, $i$ is the planetary orbital inclination, and $G$ is the gravitational constant. According to this equation, the radial velocity method is suitable for detecting close-in, massive planets. If the mass of the star is known, we can calculate the minimum mass of the planet ($M_p \sin i$) with this equation. We can measure the radial velocity of the star by high dispersion
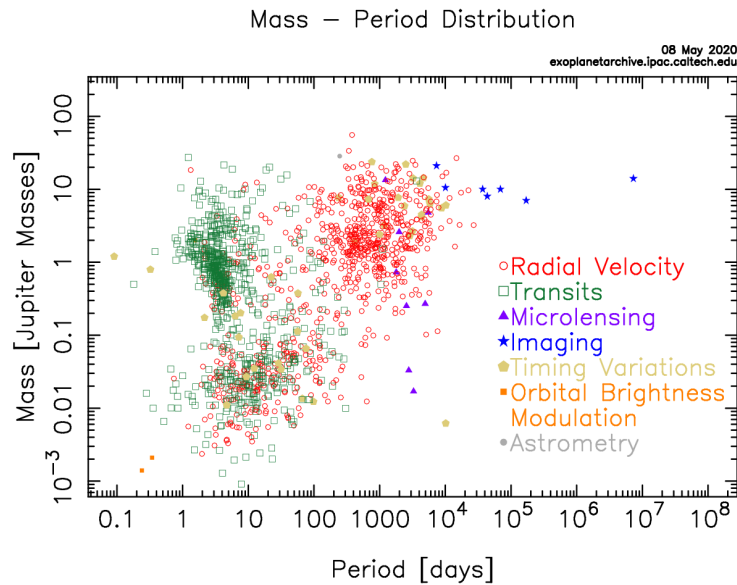
**Figure 1.1**: Mass and orbital period of exoplanets discovered so far. Color coding is used to show the detection method. The most of exoplanets were discovered by the radial velocity method and the transit method. This figure is taken from
`https://exoplanetarchive.ipac.caltech.edu/`
.

spectroscopy. Precise measurements of the Doppler shift of absorption lines in the stellar spectrum tell us the radial velocity of the star. Since the first detection of the exoplanet around a main-sequence star in 1995, the radial velocity method is one of the most powerful tools to search for exoplanets (e.g. Vogt et al. 2000, Fischer et al. 2004, Butler et al. 2006 and Figure 1.1). However, if we aim to detect low mass exoplanets like Earth, the amplitude of the radial velocity variation caused by planets is significantly small (typically a few m s$^{-1}$ or less). Therefore, some very stable high dispersion spectrographs for the precise radial velocity method have been developed (e.g. HARPS, Mayor et al. 2003, IRD, Kotani et al. 2014).

## 1.1.2 Transit Method

For a population of stars which host planets, some fraction of them have their planets on edge-on or nearly edge-on orbits. In such systems, dimming of star occurs when the planet passes between the star and the Earth; periodical dips appear in the observed variation of stellar brightness (it is called a light curve). Detecting and characterizing exoplanets with this phenomenon is called the transit method. Figure 1.2 shows the

schematics of the transit method.
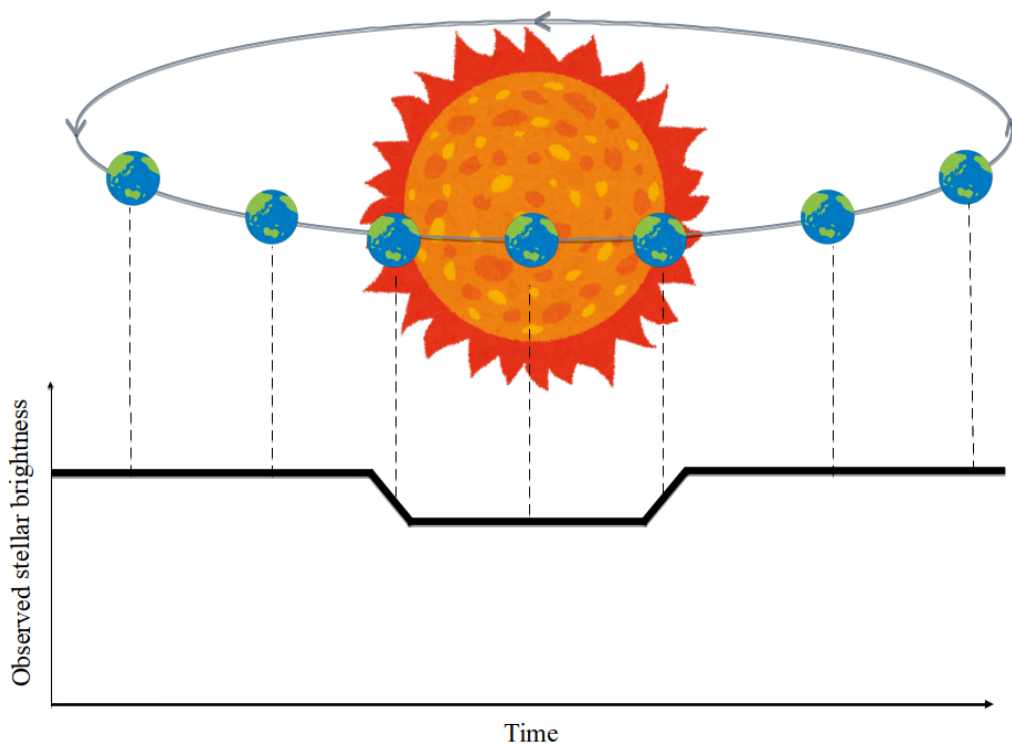


**Figure 1.2**: The schematic view of the transit method. The upper diagram shows the schematic view of how exoplanets block the light from the central star. The lower diagram shows the variation of the observed stellar brightness.

The transit probability $p_t$ and the transit depth $\Delta L$ are given by

$$p_t = \frac{R_p + R_s}{a} \qquad (1.2)$$

$$\Delta L = \frac{R_p^2}{R_s^2} \qquad (1.3)$$

where $R_p$ and $R_s$ is the radius of the planet and the star, respectively. According to these equations, the transit method is suitable to detect planets which orbit close to the star. Besides, larger planets cause deeper dimming, thus they are easier to detect. This feature in sensitivity is similar to that of the radial velocity method.

This technique is currently the most effective method to detect exoplanets because we can monitor many stars simultaneously. Planetary transit was firstly observed by Charbonneau et al. (2000) in HD209458 system. Since then, several transit surveys

have been conducted with space telescopes such as Kepler (Borucki et al. 2010, Howell et al. 2014), or CoRoT (Baglin et al. 2006) and ground telescopes such as WASP (Pollacco et al. 2006), or KELT (Pepper et al. 2007). Currently, the transit method has succeeded to detect more than 3000 exoplanet candidates, and this number is expected to increase by TESS satellite (Ricker et al. 2015).

The transit method is not only a successful approach to search for exoplanets, but a powerful tool for characterizing exoplanets. For example, we can derive the angle between stellar spin axis and planetary orbit axis with high dispersion spectroscopy (Rossiter-McLaughlin effect, e.g. Queloz et al. 2000, Hirano et al. 2020).

### 1.1.3   Transit timing variations

The period of planetary transit is not always constant. If there is another planet in the same system as a transiting planet, the transit mid-time is varied by the gravitational perturbation by the another planet. Transit timing variation (TTV) method is a detection method of exoplanets by observing mid-transit time variation. The advantage of TTV method is we can detect low-mass planets in near mean-motion resonance (e.g. Steffen & Agol 2005). TTV by another planet was firstly confirmed by Holman et al. (2010) in Kepler-9 system. The first planet detected by the TTV method is Kepler-19c (Ballard et al. 2011).

We note that there are some other mechanisms to cause TTV. If the central star has a companion star, the time of mid-transit is periodical because the optical path length from Earth to the central star varies (Irwin 1959). Tidal dissipation can also change the transit period (Watson & Marsh 2010).

### 1.1.4   Gravitational Microlensing

Gravitational lens is a phenomenon that the light from a background star was bent or focused by the gravitational force by a foreground star. When the foreground "lens" object is small such as a star, we can only observe the time variation of the luminosity. This phenomenon is called gravitational microlensing. If the lens object is only a star, the light curve caused should be symmetrical with respect to the time. However, if the lens star has a planet, anomaly appears in the light curve. Detecting exoplanets by this phenomenon is called gravitational microlensing method. One of the advantages of this method is that we can detect low-mass planets at a distance ($\sim$ several kilo parsecs). However, it is difficult to characterize detected planets because follow-up observations are almost impossible.

## 1.1.5    Direct Imaging

Exoplanets are very faint compared with stars and angular separation between stars and planets is so small, therefore it is difficult to observe the light from exoplanets directly. However, thanks to the recent high-contrast imaging technique such as coronagraph or adaptive optics, the light from several tens of planets have been observed (e.g. HR8799 bcde - Marois et al. 2008, 2010, $\beta$ Pic b - Lagrange et al. 2010, GJ504b - Kuzuhara et al. 2013). Direct imaging is suitable for observing wide-orbit ($\leq 10$ AU) and self-luminous (age $\lesssim$ a few hundred Myr) planets, therefore this technique is complementary to the radial velocity method and the transit method. One of the most famous planetary systems directly observed is HR 8799 system. Figure 1.3 shows the directly imaged four planets in the HR8799 system. If we can spatially resolve planets, we can access the information of exoplanetary atmospheres by spectroscopic observations (e.g. Snellen et al. 2014).
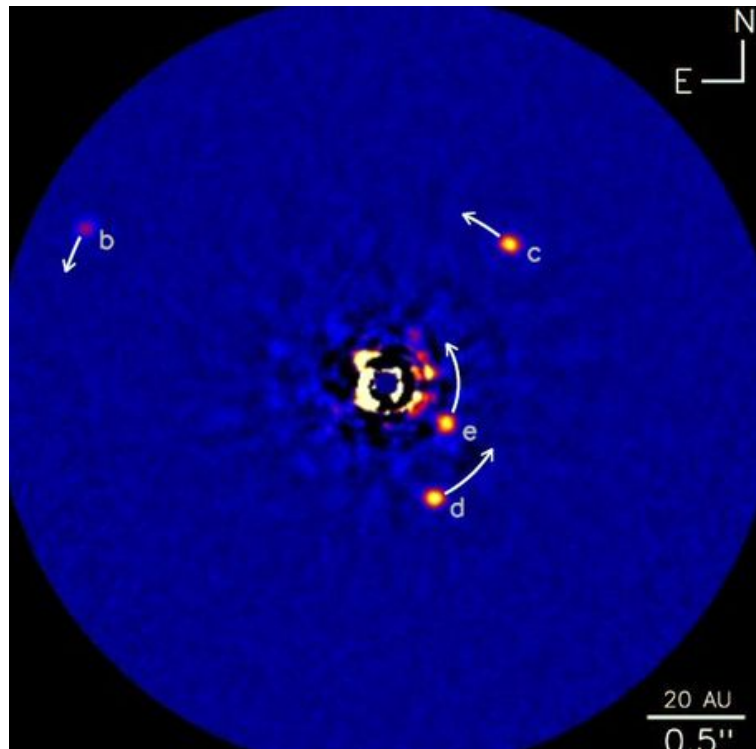


**Figure 1.3**: Four directly observed planets in HR8799 system. This image was taken by Keck telescope (Marois et al. 2010)

## 1.2  Characterization of Exoplanetary Atmospheres

Here we briefly describe the observation history of exoplanetary atmospheres. Owing to variety of observation methods described in Section 1.1, it is clear that planets are universal in our universe and have diverse physical properties. Now we are moving into a new era of characterization of exoplanets from detection of exoplanets.. However, observations of exoplanetary atmospheres are difficult, because exoplanets are much fainter than the central stars, and the angular separation between the central star and planet is quite small. Therefore, currently most of targets for exoplanetary atmosphere observations are "hot-Jupiters". Hot-Jupiters are a kind of exoplanet which does not exist in our solar system. They are gas giants like Jupiter, though they orbit close to the central star (typical orbital period is a few days). Since they are strongly irradiated by their central stars, their atmospheres have extremely high temperatures and are highly inflated. These properties make them easy to observe their atmosphere. Charbonneau et al. (2002) firstly observed the atmosphere of a hot-Jupiter HD 209458b by Hubble Space Telescope (HST). The transit depth in the sodium doublet band was deeper than in adjacent bands, and this is considered to be caused by absorption of sodium in the atmosphere of HD 209458b. Characterizing exoplanetary atmosphere by observations of transit depths at different wavelengths has been called transmission spectroscopy (Figure 1.4). If there is absorption in the planetary atmospheres at a certain wavelength, the amount of stellar flux blocked by the planet increases. This means that the effective radius of planet at the wavelength increases. Transmission spectroscopy is one of the most successful methods to characterize chemistry and structure in exoplanetary atmospheres. HST has played an important role in this field, such as $H_2O$ detection in the atmosphere of multiple exoplanets (e.g. Deming et al. 2013).

On the other hand, the thermal emission and reflection spectra from the planet have been observed. When the planet is at an orbital phase before or after being occulted by the star, we observe not only stellar spectrum but also the thermal emission and reflection spectrum from the planet. We can obtain the latter by subtracting the stellar spectrum, which is observed when the planet is completely occulted by the star (secondary eclipse). Deming et al. (2005) and Charbonneau et al. (2005) firstly observed the thermal emission from the dayside of the planet by *Spitzer* space telescope.
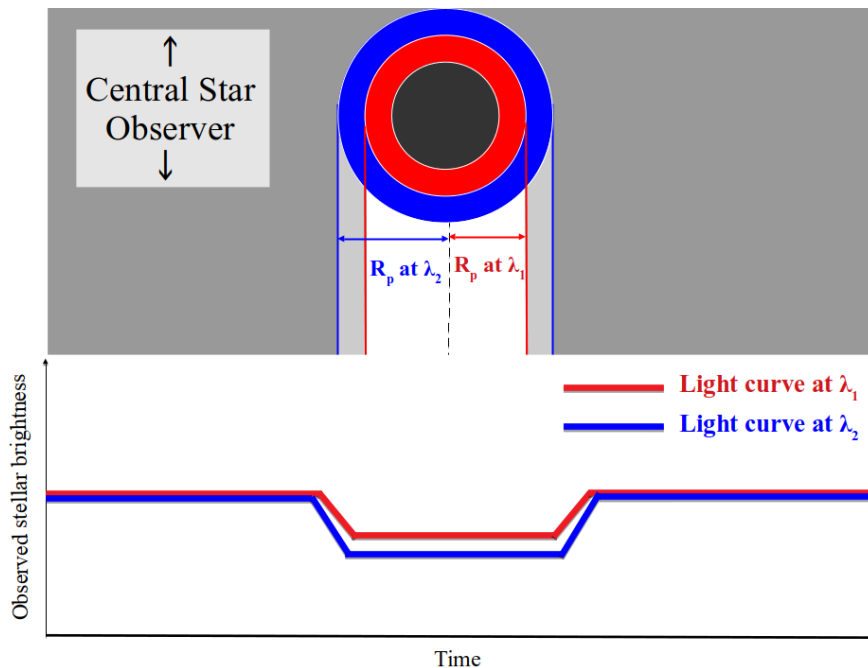
**Figure 1.4**: Schematic view of transmission spectroscopy. The upper diagram shows the difference of stellar flux amount blocked by planets at different wavelengths. Gray shade represents the flux from the central star. The lower diagram shows the light curves at different wavelengths.

## 1.3 Atmospheres of Hot-Jupiters

As described in Section 1.2, hot-Jupiter is one of the most extensively studied kinds of exoplanets. Hot-Jupiters are interesting and useful test-beds for exoplanetary atmospheres; they are easier to observe their atmosphere than other kinds of exoplanets, and they provide us clues for important problems in planetary science. In this section, we introduce the current situations of studies of hot-Jupiters' atmospheres.

### 1.3.1 Atmospheric Chemistry

Chemical composition of exoplanetary atmosphere powerfully affects the atmospheric structure and spectral features, therefore it is important for modeling of exoplanetary atmosphere. Hot-Jupiters are considered to have atmospheres composed largely of hydrogen and helium, similar to Jupiter and Saturn in the solar system. It is customary to assume solar abundance of elements for atmospheric modeling, though this

might not be suitable in some case. For example, some studies showed the formation history of a planet strongly affects the element abundance in the atmosphere of the planet (see Section 1.3.3). The abundance of each chemical species in the atmospheres of hot-Jupiters is often estimated by assuming chemical equilibrium. In this assumption, the chemical composition at a certain temperature $T$ and a pressure $P$ and a given elemental abundance is determined by minimizing the Gibbs free energy (e.g. Burrows & Sharp 1999).

While chemical equilibrium is a reasonable starting point for modeling planetary atmosphere, some physical phenomena can deviate the planetary atmosphere from the chemical equilibrium.
Non-equilibrium chemistry mainly has been studied in the contexts of photo-chemistry, vertical mixing, and clouds/hazes. Photochemical reactions are important at upper atmosphere where the flux from the central star is strong. Vertical mixing caused by atmospheric turbulence can drive the planetary atmosphere away from the chemical equilibrium. Clouds/hazes are also important because their existence affects the transmission/thermal emission spectrum of planets and abundance of elements in a gas phase. These are ubiquitous phenomena in atmospheres of planets in the solar system. For example, $O_3$ is photo-chemically generated from $O_2$ in the upper atmosphere of Earth. While clouds in Earth are composed of $H_2O$, clouds/hazes in hot-Jupiter's atmospheres are considered to be composed of various chemical species such as metal elements, silicates, carbon, and sulphur (e.g. Helling 2019). Non-equilibrium effects such as photochemistry and vertical mixing in the hot-Jupiter's atmosphere have been investigated often as case-studies for famous hot-Jupiters: Cooper & Showman (2006) for HD209458b, Line et al. (2010) for HD189733b, Moses et al. (2011) for HD189733b and HD20458b, Venot et al. (2012) for HD189733b and HD209458b, Kopparapu et al. (2012) for WASP-12b, Moses et al. (2013) for WASP-12b, CoRoT-2b, XO-1b and HD189733b, Kitzmann et al. (2018) for KELT-9b, and Molaverdikhani et al. (2020) for HAT-P-7b. Generally, in regions of pressure is $\sim 1$ mbar to $1 \sim$ bar, non-equilibrium effects are significant at lower temperatures $\lesssim 1300$ K and become less significant at higher temperatures $\gtrsim 2000$ K (Madhusudhan et al. 2014b). This is because high temperatures lead to high chemical reaction rate constants, thus chemical equilibrium becomes dominant. The effect of cloud is also significant at lower temperatures, since cloud is formed where the atmospheric temperature is below the condensation temperature of the chemical species.

If the atmospheric temperature is sufficiently high, the exoplanetary atmosphere can contain vaporized transition metals (e.g. Kitzmann et al. 2018). Such hot Jupiters have been called ultra hot Jupiters (UHJs), whose dayside temperatures $\gtrsim 2000$K (e.g.

| Planet | Dayside temperature (K) | Detected heavy metals and molecules | Reference |
|--------|------------------------|-------------------------------------|-----------|
| KELT-9b | ∼5050 | Fe I, Fe II, Ti II, Cr I, Cr II Sc II, Y II, Co I, Sr II | a,b |
| WASP-33b | ∼3300 | TiO | c |
| KELT-20b | ∼2900 | Fe I, Fe II | d,e,f |
| WASP-121b | ∼2800 | Fe I, Fe II, V I, Cr I, $H_2O$ | g,h,i,j |
| WASP-76b | ∼2700 | Fe I | k |
| HD149026b | ∼2150 | Ti I, (Fe I) | l |

Table 1.1:: Detected transition metals and molecules in UHJ atmospheres. To calculate the dayside temperatures, we assumed instantaneous re-radiation (no day–night heat distribution) with Bond albedo = 0.1.

a: Hoeijmakers et al. (2018), b: Hoeijmakers et al. (2019), c: Nugroho et al. (2017), d: Casasayas-Barris et al. (2018), e: Casasayas-Barris et al. (2019), f: Nugroho et al. (2020), g: Evans et al. (2017), h: Sing et al. (2019), i: Gibson et al. (2020), j: Ben-Yami et al. 2020, k: Ehrenreich et al. (2020), l: Ishizuka et al., submitted

Fortney et al. 2008, Parmentier et al. 2018). Recent observations reported metals in exoplanetary atmosphere (see Table 1.1). Chemical composition of exoplanetary atmosphere reflects the atmospheric conditions and formation history of the planet (e.g. Madhusudhan et al. 2014a, see Section 1.3.3), and metal and its compounds play an important role in atmospheric structure (e.g. thermal inversion, Fortney et al. 2008, Lothringer & Barman 2019, see Section 1.3.2). Therefore, characterizing exoplanetary atmospheres with metal is a fruitful approach.

The high temperature of UHJs suggests that their atmospheres are cloud-free. Clouds in the planetary atmospheres make the transmission spectrum featureless and make it difficult to detect chemical species in atmospheres. The high temperature also means signals of both thermal emission and transmission are large, because atmospheric scale height increased with temperature. Therefore, UHJs are suitable targets for atmospheric characterization and attracting a lot of attention.

## 1.3.2   Temperature-Pressure Structure and Thermal Inversion

Temperature-pressure (T-P) profile of the planetary atmosphere strongly affects the thermal emission spectrum from the planet. Therefore, understanding T-P profiles of hot-Jupiter is quite important to interpret observed spectra. In a thermal inversion layer (also called stratosphere) the temperature of air increases with an increase in altitude. In the atmosphere of Earth, there is a thermal inversion layer caused by $O_3$. $O_3$ absorbs ultra-violet (UV) light from the Sun and deposits much energy in the upper atmosphere. This $O_3$ layer protects us from the UV radiation from the Sun.

How about in exoplanetary atmospheres?

**Importance of TiO/VO**

In hot-Jupiter's atmosphere, titanium oxide (TiO) and vanadium oxide (VO) have been considered as important visible absorbers (e.g. Hubeny et al. 2003). TiO/VO can be in a gas phase at high temperatures, and absorb visible and near-infrared light well. These molecules commonly exist in the spectra of M-dwarfs, whose temperatures are similar to those of hot-Jupiters.
Fortney et al. (2008) investigated the importance of TiO/VO in hot-Jupiters' atmospheres. They classified hot-Jupiters in two groups: pM class and pL class, whose relationship is similar to that of M-type stars and L-type stars. The classification was mainly based on the incident flux from the star. In the atmosphere of pM class hot-Jupiters, TiO/VO can be in a gas phase owing to the large incident flux from the star (i.e. high temperature). Gaseous TiO/VO create a thermal inversion layer, thus emission features of molecules appear in the thermal emission spectra of the planet rather than absorption features (see Figure 1.5). On the other hand, the temperature is lower in the atmosphere of pL class hot-Jupiters. In this case, TiO/VO condensate and fall in deeper atmosphere, thus a thermal inversion layer would not be formed. For example, HD 209458b, which is one of the most-famous exoplanets, was considered to be a lower limit of pM class.
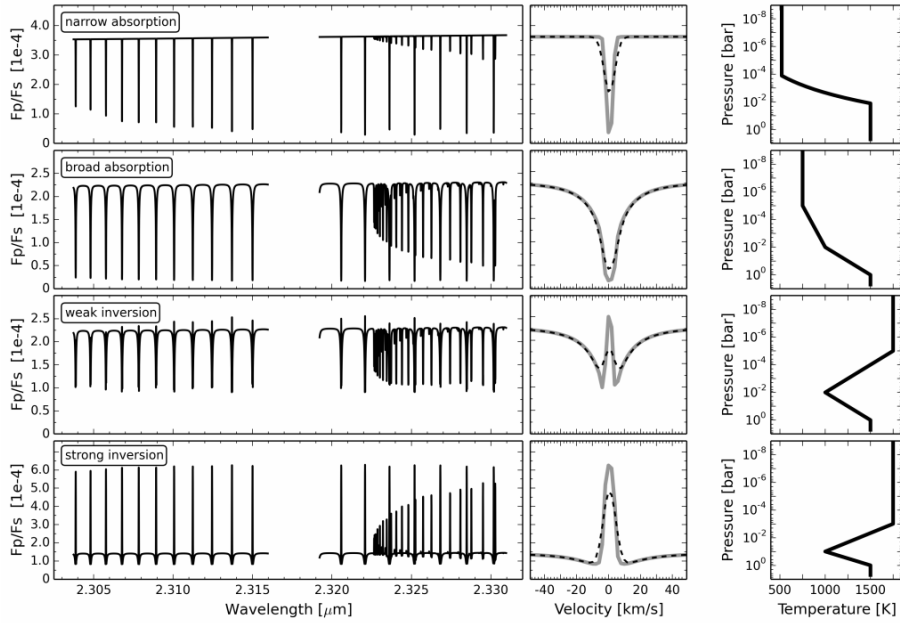
**Figure 1.5**: Theoretical line profile with various T-P profiles. The left column shows the model thermal emission spectra for carbon monoxide of HD209458b. The middle column zooms in a single line both before the convolution of instrumental spectral resolution (solid) and after (dashed). The right column displays the corresponding T-P profile. This figure is taken from Schwarz et al. (2015).

**Observational studies of thermal inversion and TiO**

Thermal inversion induces emission features of molecules in the thermal emission spectrum from the dayside of the planet. By spectrophotometry of a secondary eclipse with Spitzer telescope, Knutson et al. (2008) firstly reported thermal inversion in the atmosphere of HD 209458b based on detection of flux excess at 4.5 $\mu$m and 5.8 $\mu$m from the black body continuum. The detected excess was mainly explained by $H_2O$. Similarly, thermal inversion was reported in the atmosphere of other hot-Jupiters by Spitzer spectrophotometry (e.g. HAT-P-1b, Todorov et al. 2010, TrES-2b, O'Donovan et al. 2010, WASP-1b, Wheatley et al. 2010).

However, Hansen et al. (2014) showed that the uncertainty of Spitzer spectrophotometry for the secondary eclipse with a single event had been underestimated by a factor of 3, and previous detection of thermal inversion might be doubtful. In addition, Diamond-Lowe et al. (2014) re-investigated the secondary eclipse of HD 209458b with additional data and a new data reduction method to correct intra-pixel effects,

and they could not find the evidence of thermal inversion. Therefore, recent observational studies use broadband data by combining HST, Spitzer, or ground-based data for more robust discussion.

Haynes et al. (2015) reported thermal inversion in the dayside atmosphere of WASP-33b from the low-resolution thermal emission spectrum by combining data obtained by HST, Spitzer, and a ground-based telescope. The top of Figure 1.6 shows the observed spectrum and three model spectra (with thermal inversion, without thermal inversion, and isothermal model spectrum). The best-fit model seems to be the one with thermal inversion. They also showed that excess at near infrared wavelengths in the observed spectrum was best explained by emission features of TiO. The bottom of Figure 1.6 shows the effects of TiO and $H_2O$ in the model spectra with thermal inversion. The observed spectrum was best explained by the model spectrum including TiO and $H_2O$ with thermal inversion. However, since the TiO features were not resolved due to the low spectral resolution, the existence of TiO was not conclusive.

For other hot-Jupiters with higher equilibrium temperature than HD209458b, despite many attempts by spectrophotometry, TiO features had not been detected (e.g. WASP-12b by Sing et al. 2013, WASP-18b by Sheppard et al. 2017, HAT-P-32b by Gibson et al. 2013, WASP-17b by Bento et al. 2014). Sedaghati et al. (2017) claimed TiO detection in the atmosphere of WASP-19b by low-resolution transmission spectroscopy with VLT/FORS2, though this is controversial; Espinoza et al. (2019) reported non-detection of TiO by low-resolution transmission spectroscopy with Magellan/IMACS. What is the cause of non-detection of TiO? For example, clouds or haze at upper atmosphere make transmission spectrum featureless and obscure TiO features. Titanium depletion caused by the cold-trap effect (Spiegel et al. 2009, see Figure 1.7) is also a possible explanation for non-detection of TiO. In the cooler region under the thermal inversion, TiO/VO are effectively removed from upper atmosphere and not re-supplied, thus TiO/VO are not detected. Even in the case of UHJs (the dayside temperature is enough high at all altitude), strong winds of tidally locked hot-Jupiters can transport molecules in the upper atmosphere from dayside to nightside. If the growth timescale + settling timescale of Ti-bearing condensates is shorter than advective time scale, TiO can be trapped in the nightside and depleted in a gas phase (day-to-night trap, Parmentier et al. 2013). Meanwhile, if the C/O ratio of planetary atmospheres $\gtrsim 1$, TiO/VO are naturally under-abundant (Madhusudhan 2012).

The first robust detection of thermal inversion in planetary atmospheres was reported by Evans et al. (2017). Evans et al. (2017) reported the 5 $\sigma$ detection of $H_2O$ emission features in the thermal emission spectrum of WASP-121b with HST. Currently,
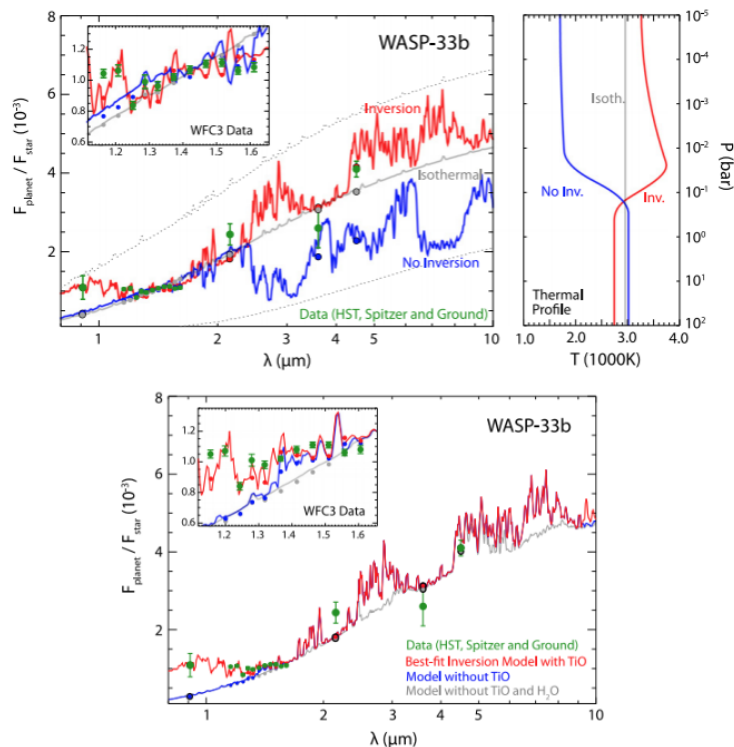
**Figure 1.6**: Dayside thermal emission spectrum of WASP-33b obtained by HST, Spitzer, and the the William Herschel Telescope. (Upper left) The observed spectrum and three model spectra with thermal inversion (red), without thermal inversion (blue), and isothermal (gray). Gray dotted lines show two black body spectra at temperatures of 1600 and 3800K. (Upper right) Temperature-pressure (T-P) profile for model spectra shown in the upper left diagram. (bottom) The observed data points and model spectra showing the effect of TiO and $H_2O$. Model spectra include the TiO opacity (red), no TiO (blue), and no TiO and $H_2O$ (gray). All model spectra assume the T-P profile with a thermal inversion. This figure is taken from Haynes et al. (2015).

thermal inversion has been reported in several ultra hot-Jupiters (Table 1.2).

However, a recent study by high resolution spectroscopy reported non-detection of TiO/VO in the atmosphere of WASP-121b (Merritt et al. 2020). Their detection limits were log of volume mixing ratio (logVMR) of TiO < -9.3 and logVMR of VO < -7.9. Since their detection limits depend on the scattering properties of atmosphere and the accuracy of VO linelist is unsure, the absence of TiO/VO in the atmosphere of WASP-121b is not conclusive. However, the conventional idea that TiO/VO exist and cause thermal inversion in the planetary atmospheres seems questionable now.
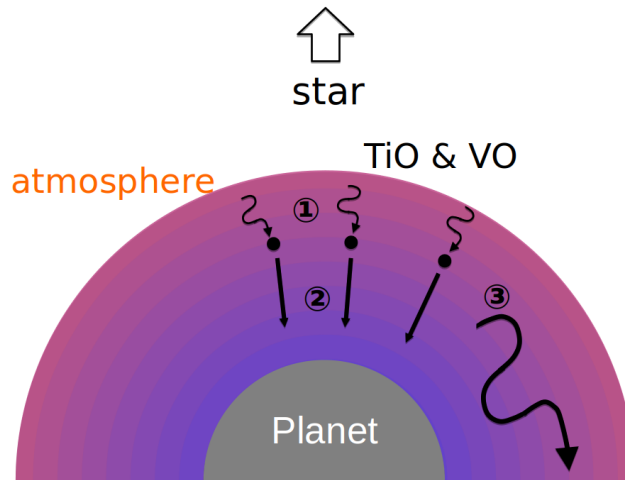
**Figure 1.7**: A schematic chart of the cold-trap effect. In the cooler regions below the inversion, TiO and VO condensates (①) and are removed from the atmosphere by rainfall (②). Furthermore, strong winds in the atmosphere of the tidally rocked hot-Jupiters might transport TiO/VO (③) to the night side of the planet. Thus, TiO/VO cannot be redistributed to the upper atmosphere and then TiO/VO might not persist in an upper atmosphere.

One big problem to search for TiO features with high resolution spectroscopy is the line list accuracy. Hoeijmakers et al. (2015) searched for TiO signatures in the atmosphere of HD209458b with high resolution transmission spectroscopy data taken by High Dispersion Spectrograph (HDS,Noguchi et al. 2002) on the Subaru telescope, though they could not find. However, they found that the line list which they used was not accurate for high resolution spectroscopy. They investigated the line list accuracy by cross-correlation of TiO transmission spectrum of HD209458b and an M dwarf (Barnard's star) spectrum, whose spectrum at visible wavelengths is dominated by TiO absorption features. Figure 1.8 shows their result. They generated model TiO transmission spectrum by the line list based on Schwenke (1998), and also made M-dwarf model spectrum by PHOENIX (Husser et al. 2013) which used the line list from Plez (1998). The transmission model spectrum seems to be in good agreement with the M-dwarf model spectrum, though is not correlated with observed M-dwarf spectrum at shorter wavelengths. This means that the line list used in Hoeijmakers et al. (2015) was not accurate for high resolution spectroscopy at shorter wavelengths.

| Planet | Dayside temperature (K) | Method | Reference |
|---|---|---|---|
| KELT-9b | ∼5050 | HRS | a |
| WASP-33b | ∼3300 | SP, HRS | b,c |
| WASP-103b | ∼3100 | SP | d |
| WASP-18b | ∼3000 | SP | e,f |
| WASP-121b | ∼2800 | SP | g |
| HAT-P-7b | ∼2800 | SP | h,i |

Table 1.2:: Planets reported in recent studies to have a thermal inversion layer. In the method column, the detection methods (SP: SpectroPhotometry, HRS: High Resolution Spectroscopy) are shown. a: Pino et al. (2020), b: Haynes et al. (2015), c: Nugroho et al. (2017), d: Kreidberg et al. (2018), e: Sheppard et al. (2017), f: Arcangeli et al. (2018), g: Evans et al. (2017), h: Wong et al. (2016), i: Mansfield et al. (2018)

Meanwhile, Nugroho et al. (2017) conducted high spectral resolution observations for thermal emission spectrum of WASP-33b with Subaru/HDS inspired by the detection of thermal inversion by Haynes et al. (2015), and reported TiO detection in the atmosphere of WASP-33b. They used line list from Plez (1998), and checked line list accuracy in each order in the similar manner as Hoeijmakers et al. (2015) (Figure 1.9) and they used only the wavelength range which were confirmed to be accurate. Since the wavelength range of their data is redder than that of Hoeijmakers et al. (2015), the line list seems to be relatively accurate. They assumed three kinds of T-P profiles; non-inversion (NI) model, full-inversion (FI) model, and the T-P profile from Haynes et al. (2015) (H-model) including a thermal inversion (see the top right diagram of Figure 1.6). They detected positive signals with FI model and H-model and negative signals with NI model. This means that there are TiO emission features in the thermal emission spectrum of WASP-33b.

Considering that TiO detection by Sedaghati et al. (2017) is controversial (Espinoza et al. 2019), currently Nugroho et al. (2017) is the only detection report of TiO in the planetary atmospheres.

**TiO line list problem**

However, even if Nugroho et al. (2017) have checked the accuracy of the line list, there is still a problem with line lists. Since TiO is an important compound for astronomy
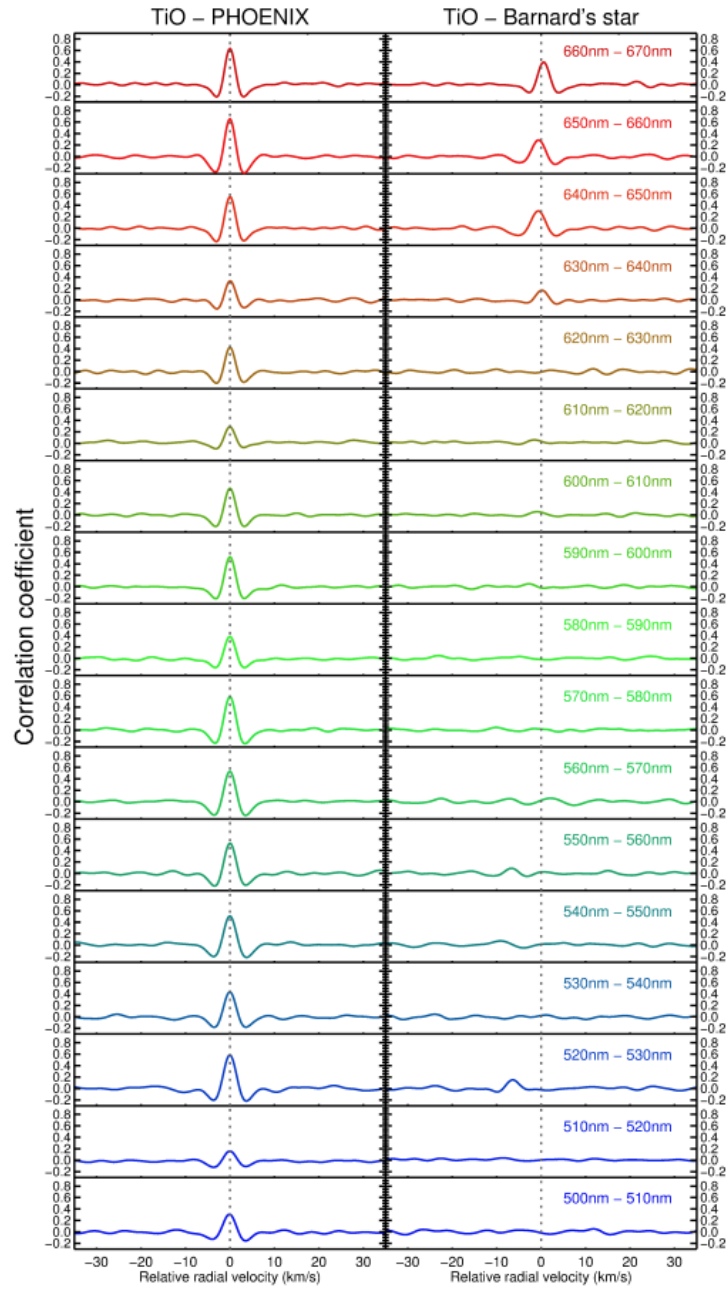
**Figure 1.8**: TiO line list accuracy check by Hoeijmakers et al. (2015). The left diagrams show the cross correlation function of the TiO model transmission spectrum the HD209458b and M-dwarf model spectrum at each wavelength range. The right diagrams show the cross correlation function of the TiO model transmission spectrum the HD209458b and observed M-dwarf spectrum at each wavelength range. This figure is taken from Hoeijmakers et al. (2015).
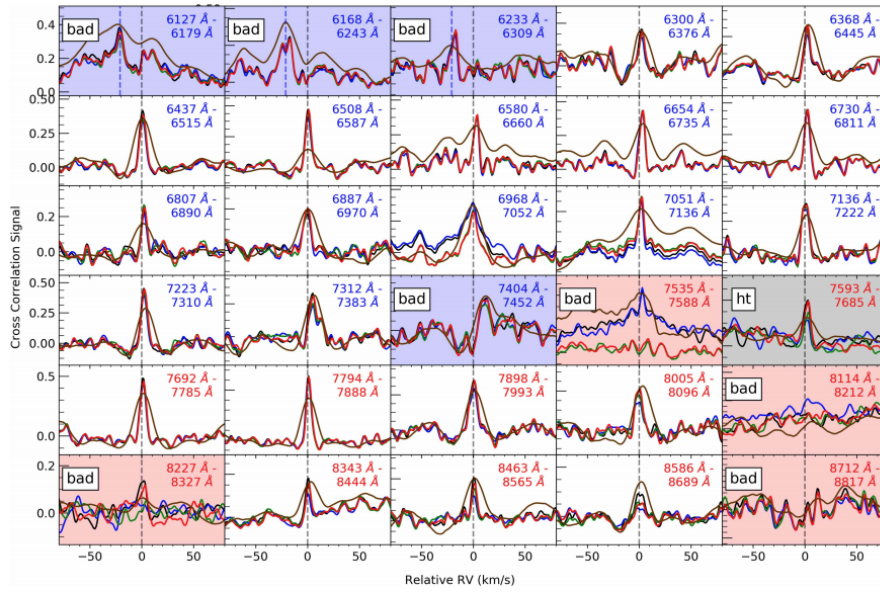
**Figure 1.9**: TiO line list accuracy check by Nugroho et al. (2017). They made a M-dwarf model spectrum using the same line list (Plez 1998) for TiO model transmission spectrum of WASP-33b. They also observed five M-dwarfs at the same instrumental setup as the WASP-33b thermal emission spectroscopy observation, and check line list accuracy by cross-correlating them: Barnard' star (black line), HD95735 (blue line), GI752A (green line), HD173739 (red line), and Proxima Centauri (brown line). All cross correlation functions were shifted to the relative radial velocity of 0 km s$^{-1}$. The result of their check was shown by the color of the each diagram. White panels stand for good orders, red and blue orders stand for bad orders, and the gray panel was masked due to heavy telluric contamination. This figure is taken from Nugroho et al. (2017).

as described in this section, some research groups have tried to improve the accuracy of the TiO line list. The line list of Plez (1998) had been improved until 2012. He had updated his line list to include updated molecular constants and laboratory transition frequencies. This updated line list has been known as the best line list for high resolution spectroscopy. On the other hand, recently McKemmish et al. (2019) also published a new TiO line list. McKemmish et al. (2019) reported that these two new line lists were more accurate than older line lists, thus it is expected that updating the line list will lead to more robust detection of TiO. In this thesis, we denote the original line list from Plez (1998) as **Plez-1998**, the updated version of Plez-1998 as **Plez-2012**, and the line list from McKemmish et al. (2019) as **Toto**.

Interestingly, Nugroho et al. (2019) reported that the detection significance of TiO was not improved by using the new line lists. Figure 1.10 shows the result of three TiO line lists. They used Plez-1998 in Nugroho et al. (2017), and found the TiO signal. However, when they tried the new line lists, the signal became weak. One of possible explanations for this problem is that the difference comes from the sensitivity of thermal emission spectra in the properties of model atmospheres. As shown in 1.5, the line profile of thermal emission spectrum strongly depends on the T-P profile of the model atmosphere. In Nugroho et al. (2019) they used the T–P profile from Haynes et al. (2015), which was derived by model fitting to HST spectrophotometry observations (see Figure 1.6). Since the cross-correlation technique is sensitive to the line profile, the difference between T-P profile of model atmosphere and actual T–P profile may result in the different detection significances with different line lists. As seen in Figure 1.11, variations of VMR or continuum absorption also affects the emission spectrum. This is because the observed emission spectrum at wavelength of $\lambda$ is roughly corresponds to the black body radiation from the atmospheric layer with $\tau_\lambda \sim 1$, where $\tau_\lambda$ is the optical depth at the wavelength of $\lambda$.

These factors make it significantly complex to model thermal emission spectra of hot-Jupiters.
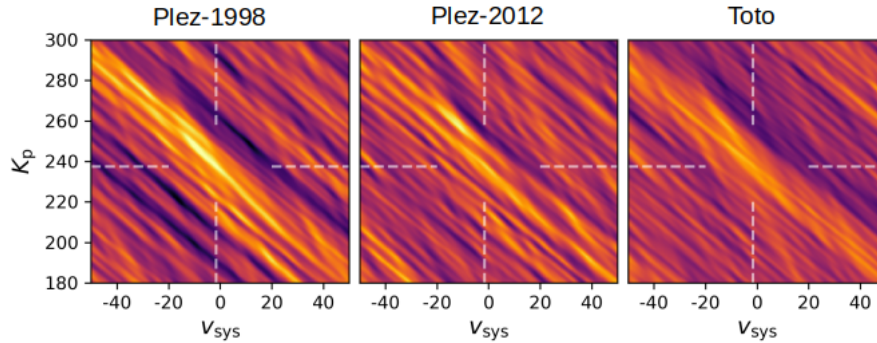


**Figure 1.10**: Results of thermal emission spectroscopy of WASP-33b with three TiO line lists. These figures are S/N maps calculated from the cross-correlation of the observed spectrum and model spectrum. The left figure is the result with Plez-1998 which was the line list used in Nugroho et al. (2017). The middle figure is the result with Plez-2012, and the right figure is the result with Toto. Figure courtesy Stevanus K. Nugroho.
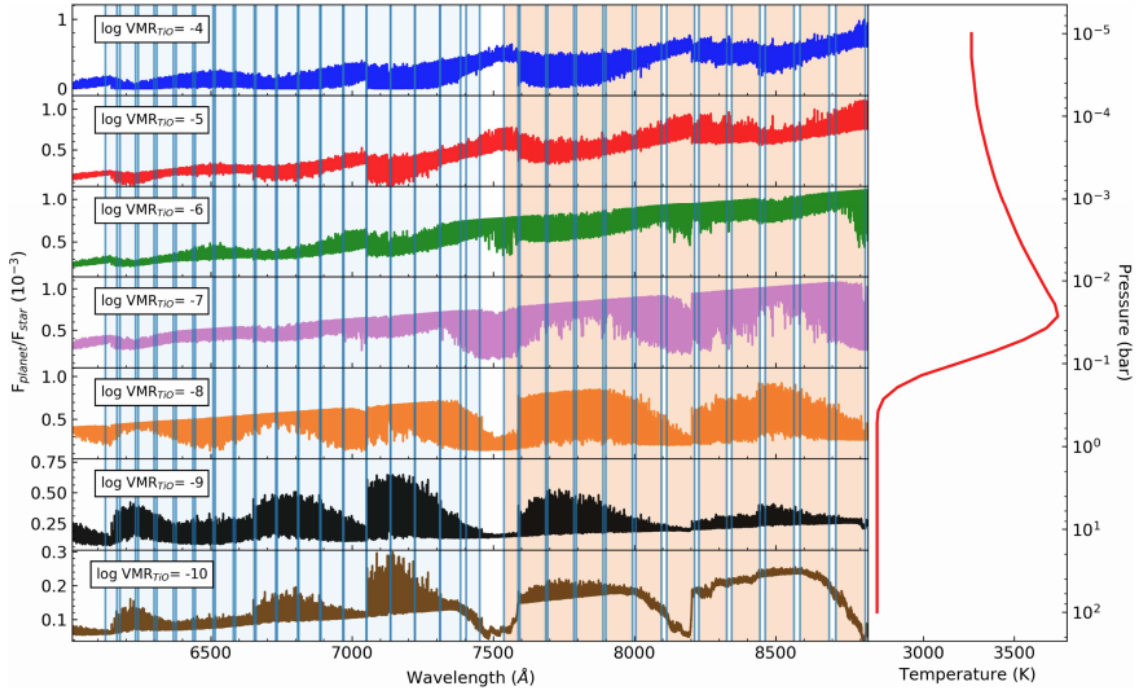
**Figure 1.11**: Thermal emission spectrum of WASP-33b with various VMR. Only optical depth from TiO was considered. The vertical axis is the planet to star flux constant. The T-P profile used in the calculation is shown in the right panel (Haynes et al. 2015). This figure is taken from Nugroho et al. (2017).

### 1.3.3 Atmospheric Compositions and Formation History

One of important advantages of characterizing chemical compositions of exoplanetary atmosphere is that we can infer the formation history of the planet. Here we briefly describe the formation theory of hot-Jupiters and theoretical predictions of chemical compositions with different formation history.

Planet formation theories were originally developed to explain the formation process of the solar system (e.g. Hayashi et al. 1985). However, since the first detection of exoplanets around a main-sequence star in 1995, more than 4000 exoplanets have been discovered and some of them have significantly different physical or orbital properties from that of planets in the solar system, such as hot-Jupiters (e.g. Mayor & Queloz 1995) or planets which have high orbital eccentricity (e.g. Holman et al. 1997). It was difficult to explain how these "strange" planets were formed by the conventional planet formation theory. Therefore, many studies of planet formation have been con-

ducted to explain the diversity of discovered exoplanets. Currently, there are mainly two scenarios for formation of hot-Jupiters: migration and *in-situ* formation.

## Migration

Migration is a promising scenario for formation of hut-Jupiters and several migration mechanisms have been proposed. In this scenario, a gas giant plant is formed in outer protoplanetary disk and migrated to inward direction. If a forming planet is massive enough to make a gap in the protoplanetary disk, a planet is considered to migrate inward following gas accretion onto the star (type Ⅱ migration, e.g. Lin & Papaloizou 1986, D'Angelo et al. 2003). Figure 1.12 shows a simulated disk structure with a Jupiter-mass planet.

Dynamical interactions with other celestial bodies may also induce inward migration. By Kozai-Lidov mechanism, planetary orbit can attain high eccentricity and inclination. Kozai-Lidov mechanism is a astrophysical phenomenon in a third-body system (Kozai 1962, Lidov 1962). Let us assume a system which consists of a central star, a planet orbiting around the star, and another outer objects. If the orbital inclination angle of the outer object relative to the orbital plane of the inner planet is larger than $\sim 39.2°$ (Kozai angle), the eccentricity and inclination of inner planet's orbit oscillate with the conservation of $L_z$, which is the z-component of angular momentum described as

$$L_z = \sqrt{1 - e^2} \cos i \tag{1.4}$$

During the phase of high eccentricity, tidal dissipation near the periastron can decay the orbit of the inner planet by decreasing the angular momentum and the energy, and might result in the formation of hot-Jupiters (e.g. Fabrycky & Tremaine 2007). When the orbit of the outer body is eccentric, the orbital elements of the inner body change intricately and hot Jupiters in retrograde orbits might be formed (Naoz et al. 2011). One good example is HAT-P-7b. HAT-P-7b is a hot-Jupiter with a retrograde orbit (Pál et al. 2008, Winn et al. 2009, Narita et al. 2009). Narita et al. (2012) reported that the central star has a companion star HAT-P-7B by imaging and confirmed another planet HAT-P-7c by radial velocity measurements. Currently, the cause of retrograde orbit of HAT-P-7b is considered the Kozai-Lidov mechanism with either or both of HAT-P-7B or HAT-P-7c.

Kozai-Lidov mechanism is considered in a limited third body system, and dynamical planet-planet scattering can also cause planetary migration. Rasio & Ford (1996) showed that a system with two gas giant planets becomes dynamically unstable and
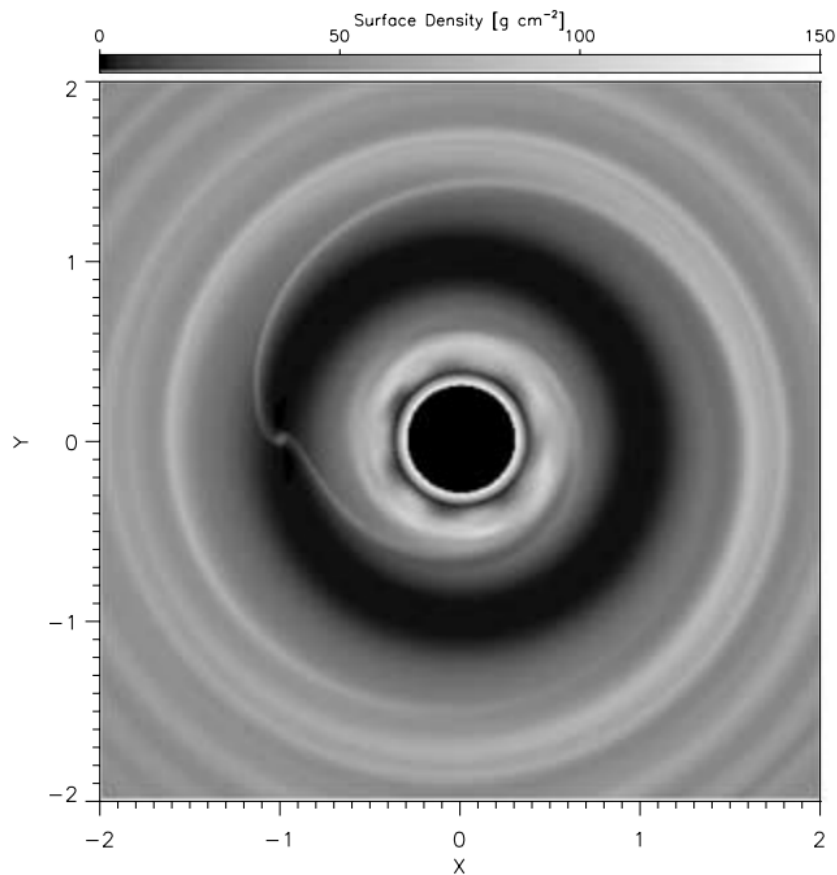
**Figure 1.12**: A simulated gap structure in a gaseous protoplanetary disk created by a Jupiter-mass forming planet. This figure is taken from Bate et al. (2003)

can lead to the formation of a hot-Jupiter. The existence of other massive planets in the same system usually results in ejection of some planets and increase of eccentricity of remaining planets (Nagasawa et al. 2008).

### *In-situ* formation

For hot-Jupiters, *in-situ* formation has been considered to be unlikely, because it is difficult to explain how gas giant is formed close to the star by both gravitational instability model and core accretion model.

The criterion $Q$ to estimate whether the system is gravitationally stable was showed

by Toomre (1964) as

$$Q = \frac{\kappa C_s}{\pi G \Sigma} \tag{1.5}$$

where $\kappa$ is epicyclic frequency, $C_s$ is the speed of sound, and $\Sigma$ is the surface density of the disk. When $Q \lesssim 1$, the gas can become unstable and contract rapidly, which leads to planet formation. However, the condition at the location of hot-Jupiters' orbit would not meet $Q \lesssim 1$ (e.g. Rafikov 2005).

Core accretion model was developed to explain the planet formation in the solar system (Pollack et al. 1996). In this model, dust grains in a protoplanetary disk accrete and grow up to planetesimals. Planetesimals move to near coplanar orbits and grow up to planetary cores. When the cores become massive enough to accrete gas ($\sim 10\,\mathrm{M}_\oplus$, e.g. Mizuno 1980, Ikoma et al. 2000), the cores grow up to gas giants by a runaway gas accretion. For *in-situ* formation of hot-Jupiters, a order of magnitude enhancement of dust surface density is required in the inner region of the disk (e.g. D'Angelo & Bodenheimer 2016). However, recent studies investigated the possibility of *in-situ* formation (e.g. Boley et al. 2016) motivated by the abundance of super-Earths with short orbital periods (e.g. Howard et al. 2010).

Several hot-Jupiters have been reported to have unusual massive cores, such as HD149026b (Sato et al. 2005), Kepler-424b (Endl et al. 2014), and WASP-59b (Hébrard et al. 2013). The formation processes of such hot-Jupiters are also still in debate. Ikoma et al. (2006) suggested possibility that HD149026b was formed via giant impact events. Batygin et al. (2016) showed that *in-situ* formation of a hot-Jupiter is possible by a planetary core like super-Earths. Batygin et al. (2016) also showed that a hot-Jupiter formed near the star can have a massive core in systems with multiple super-Earths by collisions of them induced by dynamical interactions of them inspired by the fact that a super-Earth often occurs in multi-planet systems (Lissauer et al. 2012). On the other hand, Kanagawa et al. (2018) showed that a hot-Jupiter with a massive core can be formed in a "dust ring" which is expected to be formed at outer edge of a gap created by another giant planet in the protoplanetary disk.

As described above, various scenarios have been proposed to explain the formation of hot-Jupiters. Because the atomic and molecular species in the planetary atmosphere reflects the abundance of the chemical elements and environment of place where they grew, the atmospheric composition is an important clue to investigate these scenarios (e.g., Madhusudhan et al. 2014a, Ali-Dib et al. 2014). For example, Öberg et al. (2011) showed that C/O ratio of the planets would depend on the place where the core of the planet accreted a gaseous envelope in the core acrretion scenario. Since the

condensation temperature for main carbon carriers and oxygen carriers are different ($\sim 135$ K for $H_2O$, $\sim 47$ K for $CO_2$, $\sim 20$ K for CO from Table 1 of Öberg et al. 2011), the abundance ratio of carbon and oxygen in a gaseous phase differs at a certain radius of the disk. If a gas giant accretes most of its atmosphere from gas in the disk region which is outside of the $H_2O$ snowline but inside of the CO snowline and the pollution of atmospheres by accretion of solids is small, the C/O ratio of the atmosphere of the planet will be enhanced to $\sim 1$ (cf. the C/O value in solar abundance is $\sim 0.55$).

## 1.4 Aims and Outline

As described in this chapter, atmospheres of hot-Jupiters are diverse and interesting testbeds. The chemical composition is fundamental and important information of exoplanetary atmospheres, and provides us clues for the formation process or temperature structures. High resolution spectroscopy is a suitable method to search for chemical species in planetary atmospheres, because the individual atomic or molecular lines are resolved, which leads to robust detection of them.

High resolution spectroscopy has been conducted mainly at near infrared wavelengths, because the main targets have been CO or $H_2O$ and they have strong absorption lines at near infrared wavelengths. However, recent detection of metals in planetary atmospheres (e.g. Hoeijmakers et al. 2018, see Table 1.1) showed that visible wavelengths are also interesting. Many transition metals have plenty of absorption lines at visible wavelengths. TiO, which is an important molecule for the T–P profile of planetary atmospheres and also has absorption features at visible wavelengths. Chemical composition affects structures of planetary atmospheres significantly and provides us important information of formation history of planets. Unlike thermal emission spectra, transmission spectra are not sensitive to the T–P profile of exoplanetary atmospheres (e.g. see Figure 2 in Herman et al. 2020). Thus, high resolution transmission spectroscopy is a suitable method to detect chemical species in exoplanetary atmospheres.

In this thesis, we characterize the atmospheres of two ultra hot-Jupiters, HD149026b and WASP-33b by searching for metal with high resolution transmission spectroscopy at visible wavelengths. HD149026b is a Saturn-sized planet with a massive core (Sato et al. 2005). The dayside temperature of HD149026b is $\sim 2150$ K and moderately lower than those of UHJs which have been observed with high resolution spectroscopy (see Section 1.3.1). The chemical compositions of UHJs with dayside temperature < 2500 K has not been studied well by high resolution spectroscopy at visible wave-

lengths. In addition, HD149026b is considered to have a massive core (Sato et al. 2005, Ikoma et al. 2006). These physical properties make HD149026b an especially interesting target. WASP-33b is known as one of the hottest exoplanets ever found. Haynes et al. (2015) reported a thermal inversion in the atmosphere of WASP-33b, and Nugroho et al. (2017) detected TiO emission features by high resolution spectroscopy. However, there is a line list problem as described in Section 1.3.2. Since transmission spectra are insensitive to the T–P profile, it is a suitable method to follow up their results. We utilized archive data (SMOKA, Baba et al. 2002) taken by High Dispersion Spectrograph (HDS, Noguchi et al. 2002) on the Subaru telescope. The author led entire data analysis and interpretation in this thesis.

The outline of this thesis is below. In Chapter 2, we describe high resolution spectroscopy as a technique to probe exoplanetary atmosphere and our method. Chapter 3 presents the detection of neutral metals in the atmosphere of HD149026b. Chapter 4 presents the detection of titanium oxide in the terminator region atmosphere of WASP-33b. Chapter 5 contains the discussion with the results of Chapter 3 and 4, summary of this thesis, and future prospects of this field of science.

# Chapter 2

# High Resolution Spectroscopy to Characterize Exoplanetary Atmospheres

High resolution spectroscopy has been recognized as one of the most powerful methods to characterize exoplanetary atmosphere. Each absorption or emission line of atomic or molecular species is resolved in high resolution spectroscopy, which leads to robust detection of them. In this chapter, we will introduce our method for high resolution spectroscopy to characterize exoplanetary atmospheres with cross-correlation technique. First we will start with the general explanation of of this method.

This technique has succeeded to detect molecules such as CO, $H_2O$, TiO, and HCN (e.g., Snellen et al. 2010, Brogi et al. 2012, 2013, Birkby et al. 2013, de Kok et al. 2013, Brogi et al. 2014, Birkby et al. 2017, Nugroho et al. 2017, Hawker et al. 2018, Brogi et al. 2018, Sánchez-López et al. 2019, Alonso-Floriano et al. 2019). As described in Chapter 1, if the atmospheric temperature is sufficiently high, equilibrium chemistry predicts the existence of vaporized metals in the atmosphere of hot-Jupiters. These hot-Jupiters have been called ultra hot-Jupiters (UHJs), and recent high resolution observations have also detected vaporized transition metals in the atmosphere of UHJs.

For both of transmission and emission spectroscopy, the observed spectra are dominated by stellar signals and telluric absorption lines. Therefore, removal of them is required to search for signals from the planet, and we can utilize the orbital motion of the planet. The planetary signal is expected to be Doppler-shifted due to its orbital motion; $RV_p(t)$, which is the radial velocity of the planet at a given time $t$, is

calculated as

$$RV_p(t) = K_p \sin\left(2\pi\phi(t)\right) + V_{sys} \tag{2.1}$$

where $K_p$ is the semi-amplitude of the orbital velocity, $\phi$ is the orbital phase, and $V_{sys}$ is the systemic velocity. On the other hand, the dominant stellar signals and telluric absorption are (quasi-) static during the observation. Therefore, removing static signals only is an effective method to search for faint planetary signals.

However, even if the static noise is effectively removed, the signal from a single line is too weak to detect for both of emission spectroscopy and transmission spectroscopy in most cases. Therefore, the cross-correlation technique has been used to effectively sum up all signals from many lines and to detect chemical species robustly. In this thesis, we used SYSREM algorithm to remove static components in the observed spectra. We also made model transmission spectra, and calculated cross-correlation of them and the processed data to search for chemical species in the atmosphere of hot-Jupiters.

## 2.1  SYSREM algorithm

SYStematic REMoval (SYSREM) developed by Tamuz et al. (2005) is an algorithm to remove systematic components in large numbers of transit light curves. This technique has also been used to remove static components, which is obstructive to detect planetary signals as described above, in high resolution spectroscopy (e.g., Birkby et al. 2013, 2017, Nugroho et al. 2017, Hawker et al. 2018, Gibson et al. 2020, Merritt et al. 2020). SYSREM is based on the principal-component analysis. If we assume the same uncertainty for all data points, SYSREM reduces to the principal component analysis. Let us consider the time series of transmission or emission spectra $S$ with wavelength bin number $m$ and frame number $n$. Systematic components in $S$ are fitted by effective extinction coefficient $c$ and airmass $a$. At first, the effective extinction coefficient at $i$-th wavelength bin is determined by minimizing

$$S_i = \sum_j^n \frac{(r_{ij} - c_i a_j)^2}{\sigma_{ij}^2} \tag{2.2}$$

where $r_{ij}$ is the magnitude of average-subtracted flux of the wavelength bin $i$, $c_i$ is the effective extinction coefficient of the wavelength bin $i$, $a_j$ is the airmass of the $j$-th frame, and $\sigma_{ij}$ is the uncertainty of the wavelength bin $i$ of the $j$-th frame. We took bin width of 1 pixel ($\sim 0.9$ km s$^{-1}$) of HDS. This yields the first estimation of $c_i$ as

$$c_i = \sum_j^n \left(\frac{r_{ij} a_j}{\sigma_{ij}^2}\right) \Bigg/ \sum_j^n \left(\frac{a_j^2}{\sigma_{ij}^2}\right) \tag{2.3}$$

However, extinction may also depend not only on airmass but on other factors, such as weather conditions. Therefore, we can estimate the 'effective' airmass by minimizing

$$S_j = \sum_i^m \frac{(r_{ij} - c_i a_j)^2}{\sigma_{ij}^2} \tag{2.4}$$

then the effective airmass is derived as

$$a_j = \sum_i^m \left( \frac{r_{ij} c_i}{\sigma_{ij}^2} \right) \Big/ \sum_j^m \left( \frac{c_i^2}{\sigma_{ij}^2} \right) \tag{2.5}$$

using the previously derived $c_i$. Then we can calculate a new best-fitting airmass $a_j$. By iterating this calculations, we obtain two sets $\bar{c}_i$ and $\bar{a}_j$ which are the best account for the systematic component. This iterative process converges to the same $\bar{c}_i$ and $\bar{a}_j$ regardless of the initial value (Tamuz et al. 2005, Mazeh et al. 2007). As shown above, $\bar{c}_i$ and $\bar{a}_j$ minimize

$$S = \sum_{ij} \frac{(r_{ij} - c_i a_j)^2}{\sigma_{ij}^2} \tag{2.6}$$

thus, finally derived $\bar{c}_i$ and $\bar{a}_j$ do not necessarily represent the true extinction coefficient and airmass; $\bar{c}_i$ and $\bar{a}_j$ represent the first order of systematic components in the data. Therefore, SYSREM algorithm can remove not only the telluric and stellar absorption lines but also other systematic effects (e.g. variations in pixel sensitivity) by iterating the SYSREM reduction to the residual.

## 2.2   Theoretical Transmission Spectrum

In this thesis, we use transmission spectroscopy to characterize the atmospheres of hot-Jupiters. To calculate model transmission spectra for cross correlation technique, we assumed 1-D, isothermal plane parallel atmosphere with 100 layers which were evenly spaced in log pressure from 10 to $10^{-15}$ bar. We calculated the altitude of each layer by assuming hydro-static equilibrium. At first, we calculated the optical depth, then converted them to the model transmission spectra.

**Optical depth calculation**

Optical depth $\tau$ is a quantity which represents the transparency of a medium. When flux $I_0(\nu)$ enters a medium with optical depth $\tau(\nu)$, flux after passing through the medium $I(\nu)$ is

$$I(\nu) = I_0(\nu) \, e^{-\tau(\nu)} \tag{2.7}$$

where $\nu$ is the wavenumber. When a photon travels a distance $s$, optical depth is defined as

$$\tau(\nu, s) = \int_0^s \alpha(\nu, s')ds' \tag{2.8}$$

where $\alpha$ is the volume absorption coefficient. In this thesis, to calculate model transmission spectrum for one kind of atom or molecule (hereafter we denote M) we assumed the absorption by M and Rayleigh scattering by H (Kurucz 1970) and $H_2$ (Dalgarno & Williams 1962), and continuum absorption by $H^-$ (John 1988). Then $\alpha(\nu, s)$ is described as

$$\alpha_v(s) = \sum_i^{M,\ H^-} \sigma_i(\nu, s)n_i(\nu, s) + \sum_i^{H,\ H_2} \sigma_{Rayleigh,i}(\nu, s)n_i(\nu, s) \tag{2.9}$$

where $\sigma$ is the absorption cross section, $\sigma_{Rayleigh}$ is the Rayleigh scattering cross section, and $n$ is the number density.

$\sigma_M$ was calculated by the summation of all lines in the considered wavelength range. The cross section of each single line $\sigma_{\text{single}}$ at the temperature of $T$ is calculated by

$$\sigma_{\text{single}}(\nu; \hat{\nu}, S, \gamma) = S(T) \cdot g(\nu; \hat{\nu}, \gamma) \tag{2.10}$$

where $\hat{\nu}$ is the wavenumber of the line center, $S(T)$ is the line strength at the temperature of $T$, $\gamma$ is the line broadening half width at half maximum (HWHM), and $g$ represents the line profile with $\int_{-\infty}^{\infty} g(\nu; \hat{\nu}, \gamma) = 1$.

Atomic and molecular data to calculate the cross section is provided by several databases. For example, in HITRAN[1], $S(T_0)$, namely line strength of each line at reference temperature $T_0$, is provided. Line strength at temperature $T$ is calculated by using the equation (11) of Sharp & Burrows (2007),

$$S(T) = S(T_0)\frac{Q(T_0)}{Q(T)}e^{E_{\text{low}}(hc/k_BT_0 - hc/k_BT)}\frac{1 - e^{-hc\hat{\nu}/kT}}{1 - e^{-hc\hat{\nu}/kT_0}} \tag{2.11}$$

where $Q$ is the partition function, $E_{\text{low}}$ is the energy of the lower state in cm$^{-1}$, $h$ is the Planck constant, $c$ is the speed of light, and $k_B$ is the Boltzmann constant.

The transition energy of atom or molecules is not monochromatic. There are some mechanisms which broaden the absorption line. In this thesis, we considered natural broadening and thermal broadening for line broadening mechanisms.

---

[1]https://hitran.org/

Each line has intrinsically a broadening width caused by Heisenberg's uncertainty principle

$$\Delta E \Delta t = \frac{h}{2\pi} \tag{2.12}$$

where $\Delta E$ and $\Delta t$ are the uncertainty in the energy and lifetime of states, respectively. The line profile of natural broadening is given by a Lorentzian function

$$g_L(\nu) = \frac{\gamma_L/\pi}{(\nu - \hat{\nu})^2 + \gamma_L^2} \tag{2.13}$$

where $\gamma_L$ is the Lorentz half width (HWHM).
In the gas with a certain temperature of $T$ atoms/molecules have the velocity distribution expressed by Boltzmann-distribution. Therefore, each line has also broadening width caused by the Doppler shift of all atomic or molecular particles. The line profile of thermal broadening is given by a Gaussian function

$$g_D(\nu) = \frac{1}{\gamma_D}\sqrt{\frac{\ln 2}{\pi}} \cdot \exp\left(-\ln 2\left(\frac{\nu - \hat{\nu}}{\gamma_D}\right)^2\right) \tag{2.14}$$

The HWHM of the gaussian fuction $\gamma_D$ is determined by the line position $\hat{\nu}$ , the temperature $T$ , and the molecular mass $m$ as

$$\gamma_D = \hat{\nu}\sqrt{\frac{2\ln 2 \ k_B T}{mc^2}} \tag{2.15}$$

The combined line profile of both a Lorentzian profile and a Gaussian profile can be derived by convolutions of them. This line profile is called a Voigt line profile and expressed as

$$\begin{aligned}
g_V(\nu, \hat{\nu}, \gamma_L, \gamma_D) &= K(x,y) = \frac{y}{\pi}\int_{-\infty}^{\infty}\frac{e^{-t^2}}{(x-t)^2 + y^2} \\
x &= \sqrt{\ln 2}\,\frac{\nu - \hat{\nu}}{\gamma_D} \\
y &= \sqrt{\ln 2}\,\frac{\gamma_L}{\gamma_D}
\end{aligned} \tag{2.16}$$

We note that we did not consider pressure broadening in this thesis. For transmission spectroscopy we probe the upper atmosphere with low pressure, thus the effect of pressure broadening is less significant compared with other broadening mechanisms (e.g, Nugroho et al. 2020, Gibson et al. 2020). This assumption enables us to reduce computational times significantly.

**Model Transmission Spectrum**
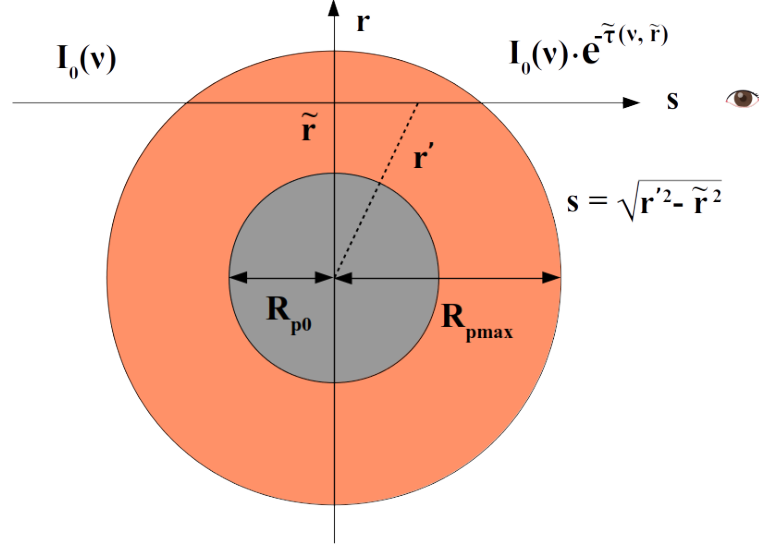


**Figure 2.1**: Illustration of transmission spectrum calculation.

Since the transparency of exoplanetary atmosphere depends on the wavelength, the transit radius of the planet varies with the wavelength. Figure 2.1 illustrates the geometry of transmission spectroscopy. The symbols with tildes indicate physical quantities in the transmission chord direction. At the planetary radius of $\tilde{r}$, the flux from the star is reduced by the planetary atmosphere by a factor of $\exp(-\tilde{\tau}(\nu, \tilde{r}))$. $\tilde{\tau}(\nu, \tilde{r})$ is calculated from the delta opacity of 1-D plane parallel atmosphere $\Delta\tau(\nu, r')$ as

$$
\begin{aligned}
\tilde{\tau}(\nu, \tilde{r}) &= 2\int_0^\infty \sigma(s)ds \\
&= 2\int_{\tilde{r}}^\infty \sigma(r')\frac{r'}{\sqrt{r'^2 - \tilde{r}^2}}dr' \\
&\simeq \sum_{r'=\tilde{r}}^{R_{\mathrm{pmax}}} \Delta\tau(\nu, r')\frac{2}{\sqrt{1 - \tilde{r}^2/r'^2}}
\end{aligned}
\tag{2.17}
$$

Then, the planetary radius at a frequency of $\nu$, $R_p(\nu)$, and the model transmission spectrum $Tr(\nu)$ are calculated as

$$
\begin{aligned}
R_p^2(\nu) &= R_{\text{p0}}^2 + \Delta R_{\text{p}}^2(\nu) \\
&= R_{\text{p0}}^2 + 2 \int_{R_{\text{p0}}}^{R_{\text{p0}}+R_{\text{pmax}}} (1 - \exp(-\tilde{\tau}_{\nu,\tilde{r}})) \tilde{r} d\tilde{r}
\end{aligned}
\tag{2.18}
$$

$$
Tr(\nu) = 1 - \left(\frac{R_p(\nu)}{R_s}\right)^2
\tag{2.19}
$$

where $R_{\text{p0}}$ is the planetary radius with white light, $R_{\text{pmax}}$ is the maximum height of the model atmosphere, and $R_s$ is the stellar radius.

# Chapter 3

# Neutral Metals in the Atmosphere of HD149026b

In this Chapter we will introduce our results of optical transmission spectroscopy of a ultra-hot Jupiter HD149026b to detect neutral metals in its planetary atmosphere. This chapter is based on a collaborative research with Hajime Kawahara, Stevanus K. Nugroho, Yui Kawashima, Teruyuki Hirano and Motohide Tamura.

Recently, UHJs (ultra-hot Jupiters) are attracting great attentions because they are an excellent laboratory for exoplanet atmospheric studies. The high temperature of UHJs should lead to their atmospheres being cloud-free. Clouds in the planetary atmosphere make the transmission spectrum featureless and make it difficult to detect chemical species in the atmosphere. The high temperature should also lead to a large amount of emission and their atmospheres being inflated, thus the signal of UHJ is large in both emission spectroscopy and transmission spectroscopy. Therefore, UHJs are suitable targets for investigating the chemical compositions of planetary atmospheres.

The UHJs that have been well studied to date have dayside temperatures $\geq 2500$ K, while the atmospheric characterization of UHJs cooler than 2500 K at visible wavelengths have not been conducted well. In this chapter, we report the results of the high dispersion transmission spectroscopy of HD149026b, whose dayside temperature is $\sim 2150$ K. HD 149026 is a subgiant G0 IV star with a radius of 1.4 $R_\odot$ and a mass of 1.4 $M_\odot$. Sato et al. (2005) discovered a Saturn-sized planet around the star by transit and radial velocity measurements. The high density suggests a large and massive core with a mass of $\sim 67$ $M_\oplus$. The process of its formation with such a large core is still in debate. The temperature of HD149026b is high enough for it to have

vaporized metals in the atmosphere, though it is cooler than the other UHJs well studied so far. Table 3.1 shows the physical parameters of the HD149026 system.

We describe the observations and data reduction in Section 3.1. The cross-correlation technique we applied is explained in Section 3.2. In Section 3.3, we present the results of the analysis. Section 3.4 is devoted to discussions and a summary of this chapter.

## 3.1 Observations and Data Reduction

This study is based on the high-resolution optical transmission spectra using the High Dispersion Spectrograph (HDS, Noguchi et al. 2002) on the Subaru telescope. We conducted basic reductions by IRAF tools and the cl script provided by HDS team. Since the signal of exoplanetary atmospheres is weak, we removed systematic noise (e.g., stellar spectrum or telluric absorption) from the spectra by SYSREM algorithm as described in Chapter 2. Generally, stable spectrographs such as HARPS (Mayor et al. 2003) or CARMENES(Quirrenbach et al. 2014) have been used for high resolution spectroscopy at visible wavelengths (e.g, Hoeijmakers et al. 2018, 2019, Casasayas-Barris et al. 2019). Since HDS is not thermally stabilized, the effect of instrumental instability is more significant. Thus, we conducted additional reductions before doing SYSREM to correct noise which might be caused by instrumental instability. In this section, we describe the observations and each reduction step.

### 3.1.1 Subaru observations

We analyzed the archival data for transmission spectroscopy of HD149026b, which were taken from the SMOKA system (Baba et al. 2002). The data were obtained on the night of May 11th, 2009, with HDS. A total of 41 frames were observed using the standard I2a mode with no iodine cell. The exposure time ranged from 480 to 720 seconds and the mean was $\sim 550$ seconds. The slit width was 0.2 mm (corresponds to 0.4 arcsec), which yields a wavelength resolution of R $\sim 90000$. The spectra were taken by two (blue and red) CCDs, which contained 26 and 17 orders and covered the wavelengths of 4923–6227 Å and 6340–7660 Å, respectively. Table 3.2 shows the basic information of analyzed data.

| Parameter | Value |
|---|---|
| **HD149026** | |
| Radius ($R_\odot$) | $1.41\pm^{0.03}_{0.03}$ [a] |
| Mass ($M_\odot$) | $1.42\pm^{0.33}_{0.33}$ [a] |
| $T_{\mathrm{eff}}$ (K) | $6179\pm^{15}_{15}$ [a] |
| log g | $4.37\pm^{0.04}_{0.04}$ [a] |
| Spectral type | G0IV [c] |
| vsin $i$ (km s$^{-1}$) | $6.0\pm^{0.5}_{0.5}$ [c] |
| [Fe/H] | $0.36\pm^{0.05}_{0.05}$ [c] |
| **HD149026b** | |
| Radius ($R_{\mathrm{Jup}}$) | $0.74\pm^{0.02}_{0.02}$ [a] |
| Mass ($M_{\mathrm{Jup}}$) | $0.38\pm^{0.014}_{0.012}$ [a] |
| $T_0$ (BJD) | $2454597.70713\pm^{0.00016}_{0.00016}$ [b] |
| Period (days) | $2.8758916\pm^{0.000002}_{0.000002}$ [b] |
| Inclination (deg) | $84.55\pm^{0.58}_{0.58}$ [a] |
| $K_p$ (km s$^{-1}$) | $169\pm^{20}_{20}$ |
| $T_{\mathrm{day}}$ (K) | $\sim 2150$ |

Table 3.1:: Basic parameters of HD149026 and HD149026b. $K_p$ means the semi-amplitude of radial velocity variation of HD149026b. We assumed no day–night heat distribution with Bond albedo = 0.1 to calculate the dayside temperature of HD149026b.

*a*: Stassun et al. (2017), *b*: Bonomo et al. (2017), *c*: Sato et al. (2005)

| File name | Exposure (s) | Start time (MJD) |
|---|---|---|
| HDSA00055831 | 480 | 54962.29704334 |
| HDSA00055833 | 480 | 54962.30337836 |
| HDSA00055835 | 600 | 54962.30971364 |
| HDSA00055837 | 480 | 54962.31745743 |
| HDSA00055839 | 480 | 54962.32379511 |
| HDSA00055841 | 480 | 54962.33013677 |
| HDSA00055843 | 480 | 54962.33647522 |
| HDSA00055845 | 480 | 54962.34281280 |
| HDSA00055847 | 480 | 54962.34915528 |
| HDSA00055849 | 480 | 54962.35550530 |
| HDSA00055851 | 480 | 54962.36184060 |
| HDSA00055853 | 480 | 54962.36818508 |
| HDSA00055855 | 480 | 54962.37452281 |
| HDSA00055857 | 480 | 54962.38085815 |
| HDSA00055859 | 600 | 54962.38720292 |
| HDSA00055861 | 480 | 54962.39493975 |
| HDSA00055863 | 480 | 54962.40128478 |
| HDSA00055865 | 480 | 54962.40762454 |
| HDSA00055867 | 480 | 54962.41397173 |
| HDSA00055869 | 720 | 54962.42031659 |
| HDSA00055871 | 720 | 54962.42944007 |
| HDSA00055873 | 600 | 54962.43856665 |
| HDSA00055875 | 600 | 54962.44630786 |
| HDSA00055877 | 600 | 54962.45405335 |
| HDSA00055879 | 480 | 54962.46179602 |
| HDSA00055881 | 480 | 54962.46814106 |
| HDSA00055883 | 480 | 54962.47448413 |
| HDSA00055885 | 480 | 54962.48082638 |
| HDSA00055887 | 480 | 54962.48717696 |
| HDSA00055889 | 600 | 54962.49352117 |
| HDSA00055891 | 600 | 54962.50125502 |
| HDSA00055893 | 600 | 54962.50899376 |
| HDSA00055895 | 600 | 54962.51674261 |
| HDSA00055897 | 600 | 54962.52448522 |
| HDSA00055899 | 600 | 54962.53222867 |
| HDSA00055901 | 750 | 54962.53996915 |
| HDSA00055903 | 750 | 54962.54943807 |
| HDSA00055905 | 780 | 54962.55890530 |

| HDSA00055907 | 600 | 54962.56872568 |
| HDSA00055909 | 600 | 54962.57646697 |
| HDSA00055911 | 600 | 54962.58420571 |

Table 3.2:: Basic information of analyzed data. Since two fits files (blue and red CCDs) are generated with one exposure in HDS observations, the listed frame IDs were every other numbered. The weather was fine and the atmospheric seeing was $\sim 0.6$ arc-seconds according to the summit log on the observation night.

### 3.1.2 Standard data reduction

We conducted a standard reduction of the data by IRAF tools and *hdsql*, provided by the team of HDS[1]. First, we performed an overscan correction, removed the bias, and converted the analog digital unit to electron numbers. Mask frames of the bad columns were made for each CCD. These processes were performed by *hdsql*. Scattered light was then subtracted by the IRAF task *apscatter*. Using 50 flat frames, we generated a median flat frame with a non-linearity correction (Tajitsu et al. 2010). We also corrected the non-linearity in object frames. To remove the fringe pattern on the spectrum, we normalized the flat frame by *apnormalize* and divided the object frames by the normalized flat frame. Then we extracted a 1-D spectrum by *apall*. The grid of the wavelength was derived by the IRAF task *ecidentify* using thorium–argon arc lump spectra, which were taken at the beginning and end of the night. We assigned the wavelength grid to each object frame by *refspectra* and *dispcor*. We conducted these reductions to the median flat frame as well as the object frames to estimate the blaze function of each order. We divided the object spectra by the estimated blaze function using *sarith*. The spectrum contains several regions affected by bad columns that were not completely removed by the reduction with the CL script. Because these bad regions can be problematic for analysis, we identified the bad regions by visual inspection and masked them.

### 3.1.3 Correction for variations of blaze function

As described in previous research, the blaze function of HDS varies during an observation due to instrumental instability (e.g., Winn et al. 2004, Narita et al. 2005). To

---

[1]https://www.naoj.org/Observing/Instruments/HDS/hdsql-e.html
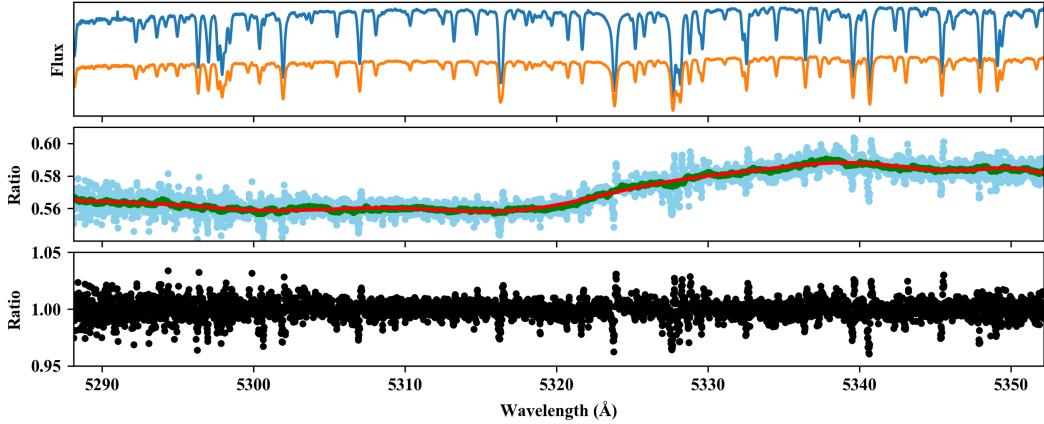
**Figure 3.1**: Correction for blaze function variation. The top panel shows the spectrum of the first frame and the reference frame (orange: 1st frame, blue: reference frame) of echelle order 112. The flux difference of these frames was mainly due to the difference in exposure time (480 seconds and 720 seconds, respectively). The middle panel shows the flux ratio for these two spectra. The light blue dots are the raw ratio and the green dots are after 3-sigma clipping and smoothing. The red line is a fit with the Chebyshev 15th order function. We used this fitted ratio as a compensator for the blaze function variation. The bottom panel shows the flux ratio for the corrected 1st frame and the reference frame.

correct for this variation, we conducted the following procedure.

First, we divided the spectrum of each frame by that of a reference frame. We used the 21st frame as the reference frame because its signal to noise ratio (S/N) was the highest. We took the raw ratio of each spectrum and the reference spectrum, and its change during the observation (Figure 3.1). Then we performed a 3-sigma clipping and smoothing of the ratio to remove the effects of residual absorption lines. After that, we fitted the clipped and smoothed ratio with the Chebyshev 15th order function. The fitted ratio determined in this way represents the variation of the blaze function for the frame compared with the reference frame. We multiplied the reference spectrum by the raw ratio and divided it by the fitted ratio, which was a spectrum with the same blaze function as the reference spectrum. Finally, we derived the continuum spectrum of the reference spectrum and normalized it by the IRAF task *continuum*. Because the spectra of all the frames have the same blaze function, we normalized the spectra of the other frames by this continuum spectrum.

### 3.1.4 Transmission spectrum matrix

As described in section 3.1.3, we obtained the normalized raw spectra $S_{\mathrm{raw}}$ for 41 frames. For further analysis, we converted $S_{\mathrm{raw}}$ to the transmission spectrum matrix in both the Earth and stellar rest frames with common wavelength grids (denoted by $F_{\mathrm{Earth}}$ and $F_{\mathrm{stellar}}$, respectively).

Instrumental instability during the observation causes a time varying shift of the spectrum on the detector. We used the telluric absorption lines in $S_{raw}$ to measure the instrumental shift relative to the reference frame. The shift was estimated from the peak of the cross-correlation between $S_{\mathrm{raw}}$ and the model telluric transmission spectrum[2] for each echelle order [3]. The cross-correlation function (CCF) was computed from the velocity difference of $-20$ km s$^{-1}$ to 20 km s$^{-1}$ with a 0.1 km s$^{-1}$ step. The peak of the CCF was derived by fitting a Gaussian to the CCF. The instrumental shift derived by the above procedure is shown in Figure 3.2. The shift seemed to be correlated with the variations of temperature inside the dome of the Subaru telescope, though the real cause of this shift is not clear. We shifted $S_{\mathrm{raw}}$ with cubic spline interpolation. We conducted a 5-sigma clipping to remove bad pixels and cosmic rays and obtained $F_{\mathrm{Earth}}$.

Then, we generated $F_{\mathrm{stellar}}$ by a cross-correlation analysis of $F_{\mathrm{Earth}}$ with the theoretical stellar spectrum. The detailed procedure is as follows. We measured the apparent radial velocity of the star in each frame by the CCF with the stellar model spectrum (Coelho et al. 2005). We fitted a Gaussian to the CCF and used the center position of the best-fit Gaussian as the stellar radial velocity in each frame. The apparent radial velocity variation is $\sim 600$ m s$^{-1}$ between the first and last frames, which is consistent with the barycentric radial velocity variation of the Earth toward HD149026. Then we shifted the spectra according to the stellar radial velocity of each frame. We note that this correction includes the correction of barycentric velocity of the Earth and the Rossiter-McLaughlin (RM) effect. The amplitude of radial velocity variation of HD149026 caused by the RM effect is $\sim 10$ m s$^{-1}$ (Wolf et al. 2007). It is difficult to obtain this level of accuracy of the stellar radial velocity measurements by HDS without iodine cell. Therefore, we just aligned each spectrum using the apparent stellar radial velocity, which includes the barycentric velocity of the Earth, RM effect, and shifts by other error factors (see Section 3.1.5). Since the expected change in

---

[2]https://www.eso.org/observing/etc/skycalc/skycalc.htm

[3]We found that only five orders in the red CCD have sufficiently strong and clear telluric absorption lines. We used these orders to measure the instrumental shift. The weighted median of the central variations of these orders was used.

velocity of HD149026b is much larger ($> 40$ km s$^{-1}$ during transit), this will not affect the detection of planetary signal (Gibson et al. 2020). We also obtained the systemic radial velocity in this reduction. The systemic radial velocity used throughout this study is $-17.92 \pm 0.11$ km s$^{-1}$.
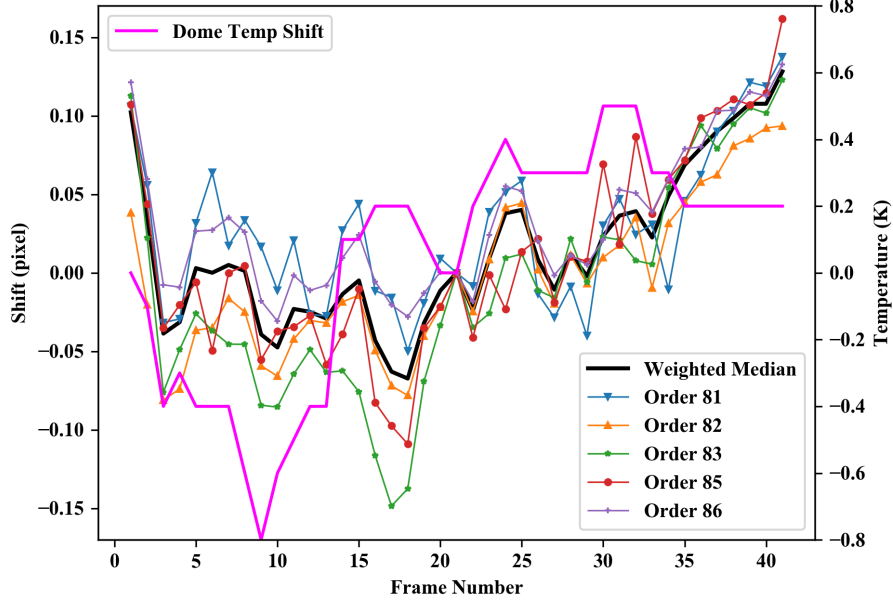


**Figure 3.2**: Relative shift owing to instrumental variation. The black solid line is the weighted median shift of the five orders where a sufficient telluric line exists. The magenta line shows the variations of the dome temperature. The relative shift is correlated with the temperature variation in the dome of Subaru.

### 3.1.5 Removal of stellar spectrum and telluric absorption

We performed a correction of the stellar line profile and detrending of the quasi-static signals by the SYSREM algorithm as follows. In the transmission spectrum matrix, the dominant signal is the stellar lines. We calculated a cross-correlation function matrix (CCF matrix) $C$ of the transmission spectrum matrix. $C$ is a function of the transmission spectrum matrix $F_{\mathrm{xxx}}$ and the stellar model spectrum $M_{st}$, and is defined as

$$C^{st}_{\mathrm{xxx}}[i, \delta v] = F_{\mathrm{xxx}}[i] \star M_{st}(\delta v), \tag{3.1}$$

where $i$ denotes the frame number, $\star$ is the cross-correlation operator, and $M(\delta v)$ is the model spectrum shifted by $\delta v$. We used a grid with steps of 1 km s$^{-1}$ as $\delta v$. We

denote $F_{\text{stellar}}$ normalized by the mean of the out-transit as $F_{\text{norm}}$. This quantity ideally becomes the transmission spectrum matrix without the stellar signals. However, we found significant residuals originating from stellar signals in $F_{\text{stellar}}$. Figure 3.3 shows the CCF matrices, $C^{st}_{\text{stellar}}$ and $C^{st}_{\text{norm}}$. Residuals remain in $C^{st}_{\text{norm}}$ at the stellar radial velocity. The strong residuals in $C^{st}_{\text{norm}}$ were correlated with the mean count and the resolution of each frame (Figure 3.4). Therefore, we assumed the line profile for the stellar spectrum was time-varying and these residuals originate from an imperfect correction of the non-linearity of the CCD and instrumental profile (IP) variations. These residuals are problematic for detecting planetary signals because the stellar radial velocity is close to that of the planet in the planetary radial velocity–systemic velocity plane.

As a first step to correct these residuals, we performed a deconvolution of the IP in $S_{\text{raw}}$. We estimated the IP of the observation night by a flat frame with an iodine cell, obtained just before the observation of the targets (Sato et al. 2002). This technique has been originally developed for the precise radial velocity method for exoplanet detection. We applied this technique to remove stellar signals. We shifted each deconvolved spectrum and aligned them to the stellar rest frame in the same manner described in Section 3.1.4. Then, we generated a template stellar spectrum by averaging the shifted spectra. We fitted

$$a\,[T * \text{IP}](\lambda) \tag{3.2}$$

to each row of $F_{\text{stellar}}$, where $a$ is a scaling factor, $T$ is the template stellar spectrum, and $*$ indicates the convolution operator. The scaling factor $a$ (for the non-linearity) and the IP are free parameters in this fitting. The IP was modeled by nine satellite Gaussian functions (Valenti et al. 1995). The positions and widths of the Gaussian functions were fixed. The only free parameters were their amplitudes. We normalized each spectrum by dividing each frame by the fitted template spectrum. The iodine cell generates numerous deep and sharp absorption lines in the 5000–5800 Å region in the nineteen echelle orders (100 to 118). We made this correction to these nineteen orders only. For the other orders, we normalized them by dividing by the mean spectrum. We denote the transmission spectrum matrix generated by this procedure by $F_{\text{IP}}$. Figure 3.3 also shows $C^{st}_{\text{IP}}$, which is a CCF matrix generated from $F_{\text{IP}}$ and the model stellar spectrum. As shown, the correction suppressed the noise at the stellar radial velocity.

Next, we used the SYSREM algorithm to remove the residuals from the stellar and telluric absorptions (Tamuz et al. 2005, Mazeh et al. 2007, see Chapter 2). We applied SYSREM to $F_{\text{IP}}$ with fifteen iterations. Thus, we obtained 3-dimensional $F_{\text{SYS}}[s, i, \lambda]$

for all of the echelle orders, with dimensions of sixteen (denoted by $s$ and ranging from 0 to 15 SYSREM iterations) $\times$ 41 (frame number, denoted by $i$) $\times$ the number of wavelength bins.

The center position of the planetary absorption lines changes during observations according to the orbital motion, while the dominant noises from the stellar and telluric absorption lines are quasi-static; SYSREM removes this static noise, leaving the planetary signals. However, the planetary signals are also eliminated as the iterations proceed too much (e.g, Birkby et al. 2017). Therefore, when the S/N reaches the highest value, we regarded the iteration number to be the optimized value. The method of S/N calculation is described in Section 3.2. Because the noise level may be different for each order, the optimal SYSREM iteration number might be different for each order. The injection of artificial planetary signals was often employed (e.g., Birkby et al. 2017, Nugroho et al. 2017) to find the optimal iteration number for each order, although this method may result in some bias. Cabot et al. (2019) reported that optimizing the SYSREM iteration number by injected signal at specific velocity might overestimate the detection significance. We also checked the validity of optimization of SYSREM iteration numbers by the injection of artificial planetary signals on our own as below. When we optimize SYSREM iteration number by the injection method, the model template spectrum is injected to the raw data ($F_{\mathrm{IP}}$) according to the expected $K_p$ and $V_{sys}$ of the planet. We need the injection of signals because the S/N of planetary signals in a single echelle order is too weak to determine the best iteration number. The SYSREM iteration number with the highest S/N is regarded as the "optimized" iteration number for each order, and the determined iteration number for each order is used for raw data. Generally, this optimization enhances the S/N of detected planetary signals. As seen in Figure 3.5, there are some spurious peaks of noise in the S/N map in the $K_p$–$V_{sys}$ plane. We found that the S/N of a noise peak was also enhanced when we did optimization at the $K_p$ and $V_{sys}$ of the noise peak. Although the origin of spurious peaks of noise in the S/N map is unknown, this result suggests that the optimization of SYSREM iteration number by the injection of artificial signals may lead to the overestimation of the significance of detected signals. Therefore, we determined a common iteration number for all the orders with the highest S/N (e.g., Turner et al. 2020, Nugroho et al. 2020). As described above, the optimal SYSREM iteration number might not be common for all orders, thus this method may result in residual noise in some orders or elimination of planetary signals in some orders. However, the difference of a few times iterations is not significant when the S/N of detected signals is high as seen in the blue line (neutral titanium) of Figure 3.6. From these considerations we chose this conservative method to avoid the overestimation of S/N of detected signals.
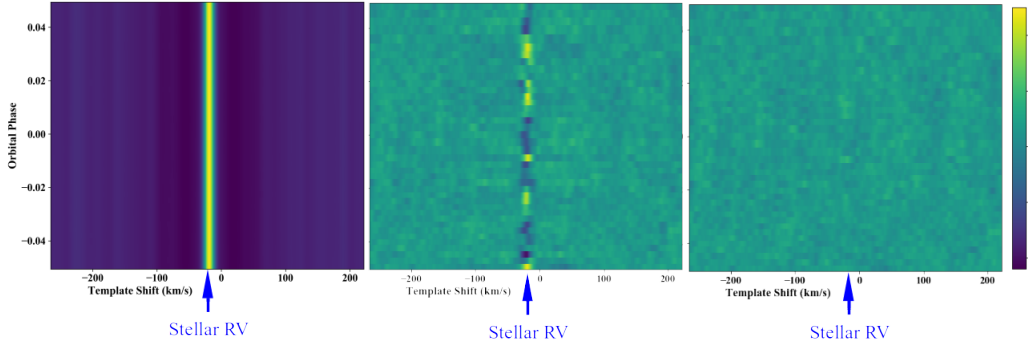
**Figure 3.3**: CCF matrix of the model stellar spectrum in each reduction step described Section 3.1.5. The left figure is $C^{st}_{\text{stellar}}$, namely, the CCF matrix of the transmission spectrum matrix $F_{\text{stellar}}$ and the stellar model spectrum. The middle figure shows $C^{st}_{\text{norm}}$, the CCF matrix of $F_{\text{stellar}}$ normalized by out-transit spectra. The value of $C^{st}_{\text{norm}}$ at the stellar radial velocity is shown in Figure 3.4. The right figure shows $C^{st}_{\text{IP}}$, the CCF matrix of $F_{\text{stellar}}$ with IP correction. Since this is a cross-correlation, the scale is arbitrary, but the middle and right figure are shown with the same color scale for comparison.

## 3.2 Cross-Correlation Analysis

### 3.2.1 Model spectra for the cross-correlation analysis

We generated the model transmission spectra for the cross-correlation template of Sc I, Ti I, V I, Cr I, Mn I, Fe I, and Co I for atomic species, and TiO for molecular species. These atoms/molecules have many absorption lines in the wavelength range of our data. Each model spectrum included absorption by a single atom or molecule plus continuum absorption. We included a continuum absorption cross section of $H^-$ and Rayleigh scattering by H and $H_2$.

We assumed a 1-D plane-parallel atmosphere with one hundred layers, which were evenly spaced in the log pressure scale from 10 to $10^{-15}$ bar. A cloud-free, isothermal atmosphere at a temperature of 2000 K was assumed. The cross sections of atomic species were calculated by *Python for Computational ATmospheric Spectroscopy* (Py4CAtS, Schreier et al. 2019) . We used partition functions taken from Barklem & Collet (2016) with a spline interpolation to obtain the partition function at the atmospheric temperature. The used line lists are given by Kurucz (2018). For TiO, we used HELIOS-K (Grimm & Heng 2015) to compute the cross section. We
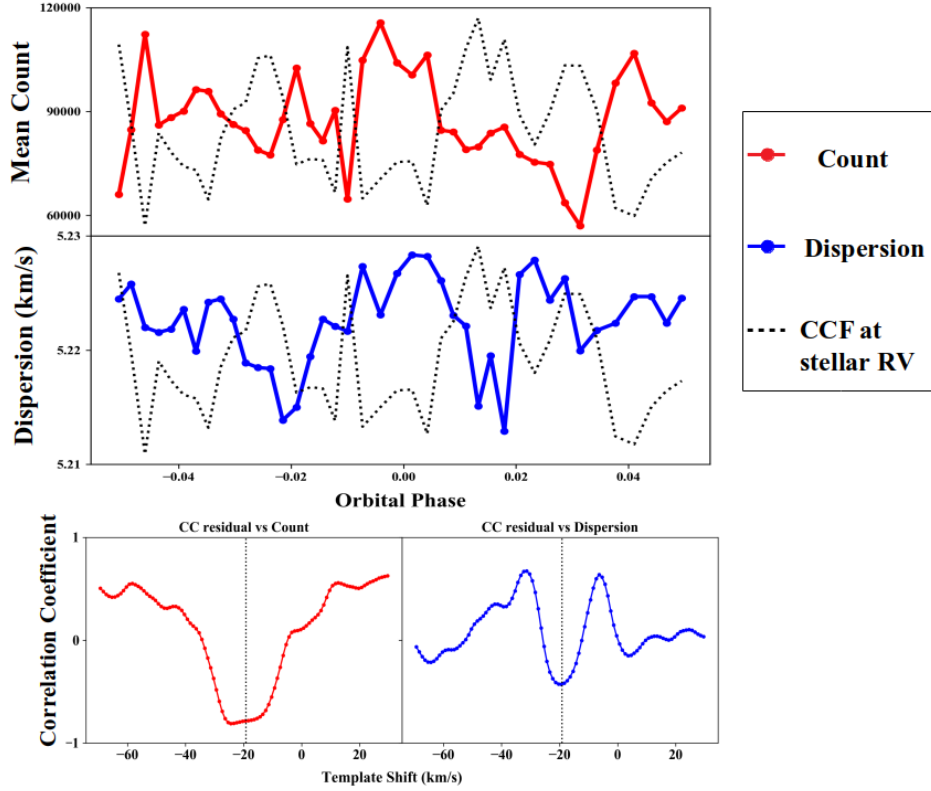
**Figure 3.4**: Relationship between mean counts or dispersion in each frame and $C^{st}_{\mathrm{norm}}$. The top and middle panels show the mean count (red) in 1 pixel (in 1-D spectrum) and dispersion (blue) in each frame. We fitted a Gaussian function to each row of $C^{st}_{\mathrm{stellar}}$ and used the width of the fitted Gaussian function as the dispersion in each frame. $C^{st}_{\mathrm{norm}}[i, \mathrm{RV}_{\mathrm{sys}}]$, namely, the value of $C^{st}_{\mathrm{norm}}$ at the stellar radial velocity, is also plotted as a black-dotted line. The bottom figure shows the correlation coefficient for $C^{st}_{\mathrm{norm}}[i, \delta v]$ and the mean count (red) and dispersion (blue). $C^{st}_{\mathrm{norm}}$ at the stellar radial velocity were strongly correlated with the mean count, and $C^{st}_{\mathrm{norm}}$ around the stellar radial velocity have correlations with the variations of the dispersion in each frame.

used two different line lists for TiO, provided by Plez (1998) (updated and corrected in 2012, hereafter Plez-2012) and McKemmish et al. (2019) (hereafter Toto). We considered the five most abundant isotopes, $^{46}\mathrm{Ti}^{16}\mathrm{O}$, $^{47}\mathrm{Ti}^{16}\mathrm{O}$, $^{48}\mathrm{Ti}^{16}\mathrm{O}$, $^{49}\mathrm{Ti}^{16}\mathrm{O}$, $^{50}\mathrm{Ti}^{16}\mathrm{O}$ and combined them with the natural isotope ratio.

The abundance of each atom and molecule in each layer was calculated using *FastChem* (Stock et al. 2018), which calculates the abundances of atoms and molecules in the

chemical equilibrium. We assumed a metallicity of 0.36 (Sato et al. 2005). The line profile based on the Voigt profile was calculated with natural broadening and thermal broadening. The delta optical depth of each layer was calculated from the cross sections of the target atom/molecule and continuum. Finally, as described in Chapter 2, We calculated the theoretical transmission spectrum $Tr(\lambda)$ as

$$
\begin{aligned}
\tilde{\tau}(\lambda, \tilde{r}) &= \sum_{r'=\tilde{r}}^{R_{\mathrm{pmax}}} \Delta\tau(\lambda, r') \frac{2}{\sqrt{1 - \tilde{r}^2/r'^2}} \\
R_p^2(\lambda) &= R_{\mathrm{p0}}^2 + 2 \int_{R_{\mathrm{P0}}}^{R_{\mathrm{P0}}+R_{\mathrm{pmax}}} (1 - \exp(-\tilde{\tau}_{\lambda,\tilde{r}})) \tilde{r} d\tilde{r} \\
Tr(\lambda) &= 1 - \left(\frac{R_p(\lambda)}{R_s}\right)^2
\end{aligned}
$$

$Tr(\lambda)$ is convoluted with a Gaussian function to mock the instrumental spectral resolution.

## 3.2.2 Cross-correlation and S/N map

We generated model spectra with a radial velocity shift from $-262.5$ km s$^{-1}$ to 224.5 km s$^{-1}$ with a step size of 1 km s$^{-1}$, corresponding to a systemic velocity ($V_{sys}$ ranging from $-120$ km s$^{-1}$ to 80 km s$^{-1}$ and the semi-amplitude of the planetary radial velocity ($K_p$) from $-100$ to 300 km s$^{-1}$ (see equation 2.1).

$C^{\mathrm{atom}}[s, i, \delta v]$ was computed as a function of $F_{\mathrm{SYS}}$ and a shifted model spectrum of each atom (denoted by $M_{\mathrm{atom}}$). We applied two high-pass filters to the spectrum of each frame to remove the effects of low-order variations before computing the cross-correlation. The cross-correlation was computed by

$$
C^{\mathrm{atom}}[s, i, \delta v] = \sum_k \frac{F_{\mathrm{SYS}}[s, i, k] M_{\mathrm{atom}}(\delta v)[k]}{\sigma_k^2}, \tag{3.3}
$$

where $\sigma_k$ is the error value at the $k$-th wavelength bin. $\sigma_k$ was calculated by taking the square root of the sum of the variance of each wavelength bin and frame of $F_{\mathrm{norm}}$. Then, we summed $C^{\mathrm{atom}}$ for the orders in which the planetary signal is strong. The criterion for this selection process is that the strongest line depth in the order is deeper than 2e$^{-5}$ to the continuum, which corresponds to $dR_p \sim \frac{H}{2}$ in equation 2.18, where $H$ is the scale height of the planetary atmosphere. In this way, we obtained $C^{\mathrm{atom}}$, whose dimensions are 41 (frame number) $\times$ 488 (radial velocity from $-262.5$ km s$^{-1}$ to 224.5 km s$^{-1}$) for each SYSREM iteration number. Then, we computed

the CCF map in the $K_p$–$V_{sys}$ plane as follows: we integrated $C^{\mathrm{atom}}[s]$ (in the frame - radial velocity plane) along the path of expected planetary radial velocity $RV_p$ using equation 2.1

$$
\begin{aligned}
RV_p &= K_p \, \sin(2\pi\phi(t)) + V_{sys} \\
\phi(t) &= \frac{t - T_o}{P},
\end{aligned}
\tag{3.4}
$$

where $\phi(t)$ is the orbital phase of the planet, $t$ is the Barycentric Julian Day (BJD) of each exposure. Only the in-transit frames were used for this calculation. The orbital phase of each frame was calculated by the orbital parameters shown in Table 3.1. We also calculated the expected amount of starlight blocked by the planet for each frame by *batman* python software (Kreidberg 2015), and used it as a weighting coefficient with a $K_p$–$V_{sys}$ integration. To make the S/N ($\sigma$) map, we divide the CCF map by its standard deviation after excluding the expected position of the planetary signal and region with $|K_p| < 50$ km s$^{-1}$, since the signal with low $|K_p|$ approaches zero as SYSREM iteration proceeds.

We also calculated the detection significance (hereafter $\sigma_{\mathrm{shuffle}}$) by the phase shuffling method (e.g., Esteves et al. 2017). We randomly shuffled the in-transit CCF map in the phase axis and integrated them with $K_p$ of the detected peak. We repeated this calculation 10000 times. The significance at each $V_{sys}$ was calculated by dividing the original integrated CCF value by the standard deviation of the shuffled and integrated CCF values.

| species | $K_p$ (km s$^{-1}$) | $\Delta V$ (km s$^{-1}$) | S/N | $\sigma_{\mathrm{shuffle}}$ |
|---------|---------------------|--------------------------|-----|------------------------------|
| Ti I | $147\pm^{19}_{20}$ | $-3\pm^{1}_{1}$ | 5.0 | 4.4 |
| Fe I | $162\pm^{38}_{45}$ | $-1\pm^{3}_{2}$ | 2.8 | 2.8 |

Table 3.3:: Positions, S/N, and significance of detected peaks in the $K_p$–$V_{sys}$ plane. $\Delta V$ is the difference between the systemic velocity for the detected peak and the stellar radial velocity ($-17.92$ km s$^{-1}$). The detection significance was estimated by the phase-shuffling method (Esteves et al. 2017).
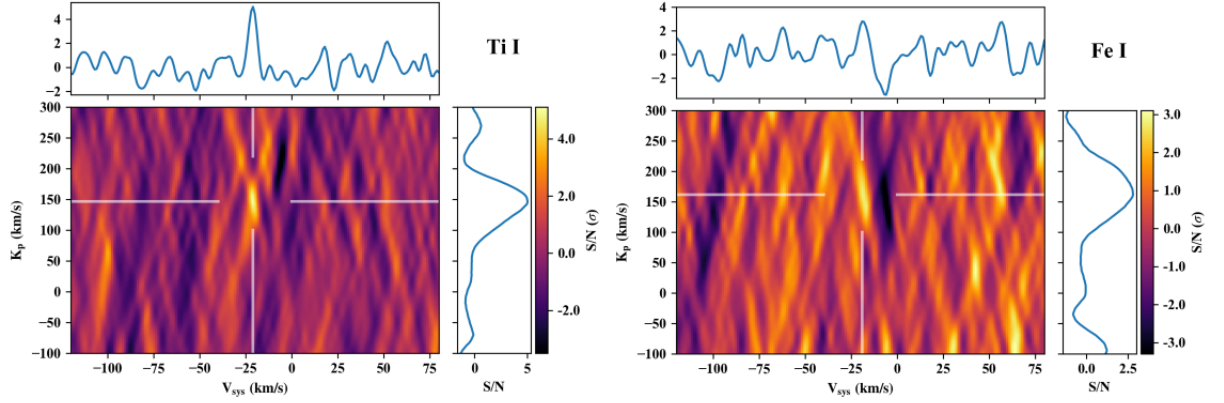
**Figure 3.5**: S/N ($\sigma$) map of Ti I and Fe I in $K_p$–$V_{sys}$ plane. 1-D cross sections along the $K_p$ and $V_{sys}$ directions are also shown.
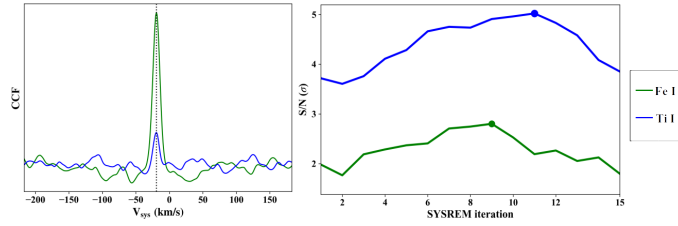


**Figure 3.6**: (left) Cross-correlation function of model transmission template spectrum and $F_{\text{stellar}}$. The black dotted line shows the stellar radial velocity. There are also absorption lines for Fe I and Ti I in the stellar spectrum, and the absorption by Fe I is stronger than that of Ti I. (right) S/N for detected peak with SYSREM iteration number. The adopted iteration numbers for the S/N ($\sigma$) map in Figure 5 (the best iteration number) are shown by dots.

## 3.3 Results

### 3.3.1 Neutral titanium and iron

We made the first detection of neutral titanium (Ti I) in a planetary atmosphere. We also detected marginal signal of neutral iron (Fe I). The S/N for the detected signals was 5.0 for Ti I and 2.8 for Fe I. The $\sigma_{\text{shuffle}}$ were 4.4 and 2.8, respectively.

Figure 3.5 shows the S/N ($\sigma$) map in the $K_p$–$V_{sys}$ plane. The peak values are $K_p = 147 \pm^{19}_{20}$ km s$^{-1}$, $\Delta V = -3 \pm^{1}_{1}$ km s$^{-1}$ for Ti I, and $K_p = 162 \pm^{38}_{45}$ km s$^{-1}$, $\Delta V = -1 \pm^{3}_{2}$
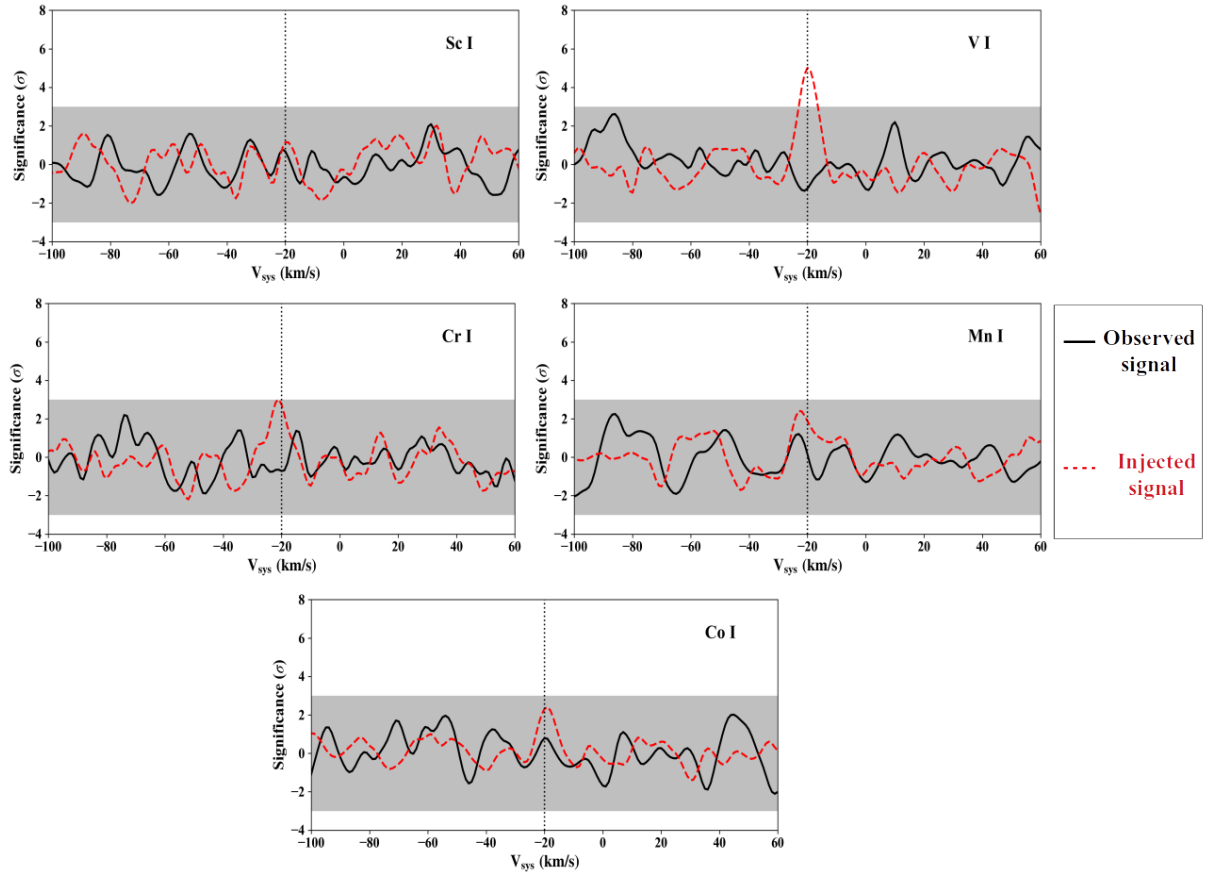
**Figure 3.7**: Observed signals and results of injection tests for non-detected atomic and molecular species except TiO. The red dotted line shows the significance of the injected signals at $K_p$ =-150 km s$^{-1}$ and $V_{sys} = -20$ km s$^{-1}$ after 10 SYSREM iterations. The black solid line shows the significance of the observed signals at $K_p = 150$ km s$^{-1}$ after 10 SYSREM iterations. The grey shading represents the $\sigma < 3$ detection limit.

km s$^{-1}$ for Fe I, respectively. The values of $\Delta V$ means the difference between the systemic velocity of the detected peak and the stellar radial velocity (-17.92 km s$^{-1}$). Note that we only used echelle orders 100 to 118 for Fe I, because the stellar noise was significant in orders without the line profile correction. We excluded the frames 22 and 23 (the two closest frames to the mid-transit) for neutral metals in order to avoid affects by the residual of the stellar signal, because the planetary signal was expected to be overlapped with the center of the stellar absorption lines in these frames. Figure 3.6 shows the S/N for the detected peak with SYSREM iteration numbers from 0 to 15. The SYSREM iteration number for the highest S/N is 9 for Fe I and 11 for Ti I. Figure 3.6 also shows the cross-correlation functions for the model transmission template spectrum and $F_{\text{stellar}}$. Figure 3.6 shows that the absorption lines for Fe I in the stellar spectrum were stronger than those for Ti I. The marginal detection of Fe I might be due to the strong contamination from stellar spectrum.

## 3.3.2 Non-detection of the other atomic/molecular species

We could not find planetary signals for any other atomic or molecular species. For the non-detected species, we conducted an injection test to investigate the detection limit in our analysis (Figure 3.7, 3.9). We injected a model template spectrum of each of the species to the spectrum matrix before SYSREM detrending. We convoluted a model spectrum with a rotation kernel to simulate line broadening by planetary tidally locked rotation by $\sim 1.3$ km s$^{-1}$ and a boxcar function to simulate smearing due to the orbital motion of the planet $\sim 2.3$ km s$^{-1}$, then injected the broadened model spectrum assuming $K_p = -150$ km s$^{-1}$ and $V_{sys} = -20$ km s$^{-1}$. To avoid the effect of unseen planetary signals from the planetary atmosphere, $K_p$ was inverted (Merritt et al. 2020). The detection significance for the injected signal was calculated by the phase shuffling method. In this study, we consider species to be undetectable if the significance of the injected signal is $\lesssim 3\ \sigma$. For Sc I, Cr I, Mn I, and Co I, the expected signal was $\lesssim 3\ \sigma$, comparable to the noise, and thus we could not confirm the existence of these atomic/molecular species. Our analysis was able to detect V I with $\gtrsim 5\ \sigma$, showing that V I is depleted in the HD149026b atmosphere with $\gtrsim 5\ \sigma$, with the assumption of a cloud-free, 2000-K isothermal atmosphere, and chemical equilibrium.
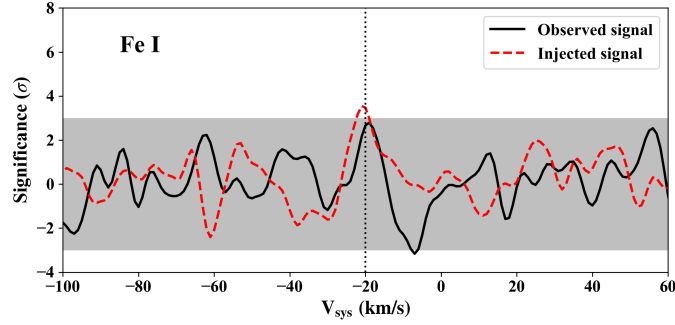
**Figure 3.8**: Observed signal and the result of an injection test of Fe I. The significance of the observed Fe I signal is 2.8.
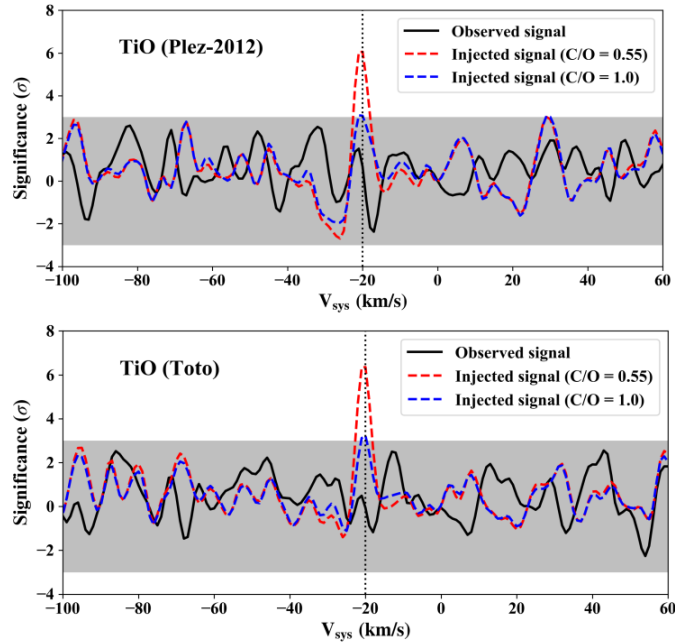


**Figure 3.9**: Results of injection test of TiO under chemical equilibrium with a C/O value of 0.55 (solar) and 1.0 after 10 SYSREM iterations. The top figure is the result with the linelist provided by Plez (1998) (updated version in 2012), and the bottom figure is the result with the linelist from McKemmish et al. (2019). This study can detect TiO with $\sigma > 6$ for both of linelists, if the abundance of TiO is the same as the calculated value with the solar C/O ratio. However, if the C/O ratio is enhanced to 1, the planetary signal is expected to be at the noise level.
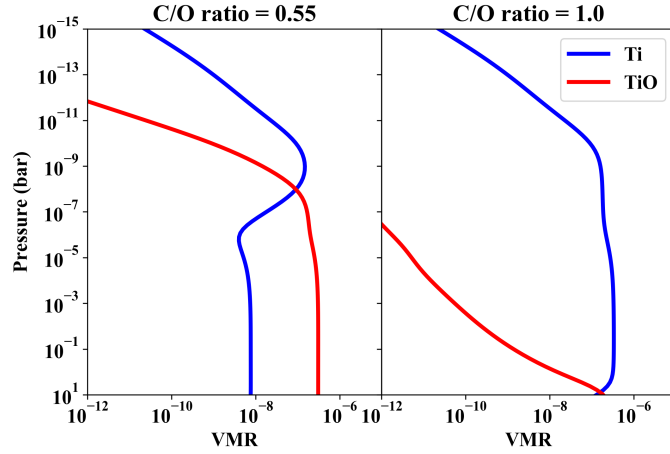
**Figure 3.10**: Volume mixing ratio of Ti I and TiO with a temperature of 2000 K calculated by *Fastchem*. We set the metallicity to 0.36.
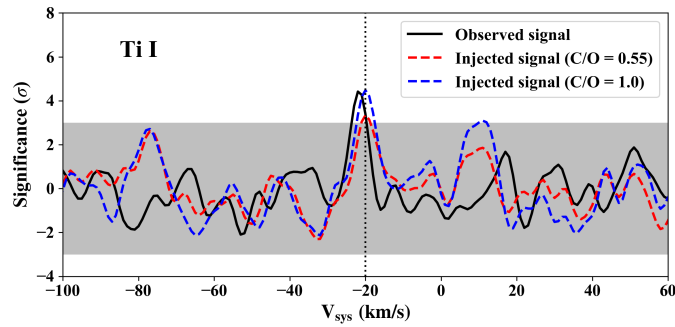


**Figure 3.11**: Observed signal and the result of an injection test of Ti I under chemical equilibrium with a C/O value of 0.55 (solar) and 1.0 after 11 SYSREM iterations. The significance of the observed Ti I signal is 4.4.

**Titanium oxide**

Assuming a solar-like abundance and chemical equilibrium, titanium mainly exists in the form of titanium oxide (TiO) at a temperature of $\sim$ 2000 K. Figure 3.10 shows the abundance of Ti I and TiO in chemical equilibrium calculated using *Fastchem*. Since there is a line list problem for TiO, we used the wavelengths range in which line lists are confirmed to be accurate by comparing with a spectrum of M-dwarf. The detail of this line list accuracy check is described in Chapter 4. We could not detect TiO signal with both of line lists. To consider the implication of the non-detection of TiO in our analysis for both line lists, Plez-2012 and Toto, we performed injection

50

tests for TiO.

As shown in Figure 3.9, if the planet had a cloud-free, 2000-K isothermal atmosphere, and chemical equilibrium, our analysis could detect TiO signals with $> 6\ \sigma$ for both line lists. This is indicative because we detected neutral titanium but not TiO. We discuss the implications in the next section in more detail.

## 3.4 Discussion and Summary

### 3.4.1 Physical properties of the atmosphere of HD149026b

Figure 3.8 shows the expected significance of the Fe I signal. Since the expected significance is not high ($\sim 3.5\ \sigma$) and the detection of Fe I is not robust ($2.8\ \sigma$), it is difficult to discuss the marginal detection of Fe I. Therefore, hereafter we discuss mainly based on the detection of Ti I. Titanium and iron can condense and take the form of clouds below the condensation temperature. The condensation temperatures for typical condensates with a pressure of 1 mbar are 1582 K for $CaTiO_3$ and 1650 K for FeO (Wakeford & Sing 2015). Our detection of titanium (and possibly iron) in a gaseous phase indicates that the temperature of HD149026b is higher than the condensation temperatures for Ti-bearing and Fe-bearing condensates. We note that the equilibrium temperature for HD149026b is $\sim 1680$ K, consistent with our results, if we assume the received energy is evenly redistributed to the whole planet and the Bond albedo $= 0.1$. This temperature is higher than the condensation temperatures for most chemical species which can form clouds (Wakeford & Sing 2015). Given this high temperature and the fact that we detected atomic species in the atmosphere, the effect of clouds would not be significant for HD 149026b. This is consistent with our assumption of a cloud-free model atmosphere. However, we cannot rule out the cloud hypothesis because several other chemical species have condensation temperatures higher than $\geq 2000$ K (e.g., see Figure 2 in Mbarek & Kempton 2016).

A possible explanation for the non-detection of TiO is a supersolar C/O ratio in the planetary atmosphere, as reported for several other hot Jupiters (Brewer et al. 2017), since the abundance of TiO strongly depends on the C/O ratio (e.g. Madhusudhan 2012). Other scenarios which have been proposed to explain the absence of TiO in the planetary atmospheres are unlikely in this case. Our detection shows that titanium is not depleted in the atmosphere of HD149026b, thus titanium depletion by cold-trap effect (Spiegel et al. 2009, Parmentier et al. 2013) would not be significant in the atmosphere of HD149026b. Strong chromospheric activity of the host star might destroy the TiO in planetary atmospheres, though the activity of HD149026 is low based

on the analysis of Ca II H & K lines (Knutson et al. 2010). Figure 3.10 also shows the VMR of Ti I and TiO with C/O values of 0.55 and 1.0. As the C/O ratio approaches $\sim 1$, the abundance of TiO significantly decreases. Figure 3.9 shows the result of an injection test assuming a C/O ratio of 0.55 and 1.0. In the case of C/O ratio = 1.0, our analysis will not detect a TiO signal with $\gtrsim 3\,\sigma$, therefore the scenario of C/O $\gtrsim$ 1 is consistent with our results. We also estimated the expected significance of the Ti I signal in the same way (Figure 3.11). The predicted significance of Ti I with a C/O value of 0.55 and 1.0 was $\sim 3.3$ and 4.5, respectively. The significance of the detected signal was 4.4, thus our result is consistent with the scenario that the C/O ratio is higher than the solar value. However, we note that the predicted significance strongly depends on the atmospheric properties such as scale height or scattering properties, because the depth of absorption lines in the model transmission spectrum is affected by these properties.

The C/O ratio for the planetary atmosphere provides information on its formation history. Some hot Jupiters have been reported to have supersolar C/O ratios (e.g., HD209458b, Madhusudhan & Seager 2009). A supersolar C/O ratio suggests that the planet swept up a large portion of its atmosphere from the gas in the protoplanetary disk outside the water snowline (gaseous oxygen is reduced); that is, the planet formed outside the water snowline and migrated to the current orbit (e.g., Öberg et al. 2011). Therefore, our detection of Ti I and non-detection of TiO suggest that HD149026b formed outside the disk and migrated to the current orbit. We note that the reported C/O ratio of HD149026 is 0.48 (Brewer & Fischer 2016). HD149026b is considered to have a massive core ($\sim 67\ M_{\oplus}$) like WASP-59b (Hébrard et al. 2013). The formation history of hot Jupiters with massive cores is still in debate. It is considered that such hot Jupiters are formed in an environment with a high dust grain density (Ikoma et al. 2006). Kanagawa et al. (2018) showed that a planetary-induced gap in the protoplanetary disk can make a 'dust ring' at the outer edge of the disk, and a gas giant with a massive core can be formed in the dust ring. In this scenario, HD149026b would have migrated by dynamical scattering. Our detection of neutral metals and the implication of a high C/O ratio provide clues on the formation history of hot Jupiters with massive cores.

Line et al. (2014) reported that the atmospheric C/O ratio for HD149026b is 0.45 to 1.0 (68% confidence), determined by *Spitzer* photometry of a secondary eclipse. The C/O ratio of $\sim 1$ hypothesis does not contradict their results. However, the detection limit for atom/molecule abundance discussed depends on the properties of the planetary atmosphere. In our model we assumed Rayleigh scattering by H and $H_2$, continuum absorption by $H^-$, and a cloud-free, 2000K isothermal atmosphere under chemical equilibrium, and the detection limits we set should be interpreted in this

context only.

### 3.4.2   Origin of the blueshift

The detected signals were slightly blue-shifted compared with the central star. A typical wind speed from the dayside to nightside in a tidally locked hot Jupiter's atmosphere is a few km s$^{-1}$ (e.g., Kataria et al. 2016), which is consistent with the blueshift of the detected signals. However, if we assume the planet is tidally locked, the rotational velocity at the equator is $\sim 1.3$ km s$^{-1}$. The asymmetric distribution of atomic species in the terminator region atmosphere also shifts the planetary signals (Ehrenreich et al. 2020). Since the blueshift of the detected signals is also consistent with the planetary rotation, we could not confirm the cause of the blueshift of the detected signals.

### 3.4.3   Summary

In this chapter, we presented the results of high-resolution transmission spectroscopy of HD149026b at visible wavelengths using Subaru/HDS. We detected neutral titanium (4.4 $\sigma$) and iron (2.8 $\sigma$) in the atmosphere of HD149026b. Our study is the first detection of neutral titanium in planetary atmospheres.

The detection of Ti I and the non-detection of TiO suggests a supersolar C/O ratio in the atmosphere of HD149026b.

The formation scenario for hot Jupiters is of great interest in exoplanetary science. HD149026b is a hot Jupiter with a massive core, and its formation history is still controversial. Our detection of neutral metals and the implication of a supersolar C/O ratio suggest that HD149026b formed outside the water snowline and migrated to the current orbit. Our study adds important clues for understanding the unique properties of this hot-Jupiter.

# Chapter 4

# Detection of Titanium Oxide in the Terminator Region Atmosphere of WASP-33b

In this Chapter we will introduce our results of optical transmission spectroscopy of another ultra hot-Jupiter WASP-33b to search for titanium oxide in its planetary atmosphere. This chapter is based on a collaborative research with Hajime Kawahara, Stevanus K. Nugroho, and Motohide Tamura.

Titanium oxide (TiO) has been considered as a key molecule for thermal inversion in the planetary atmospheres. However, in spite of many attempts to detect TiO in the planetary atmosphere, TiO had not been detected. Up to now, Sedaghati et al. (2017) and Nugroho et al. (2017) claimed the detection of TiO in the atmosphere of WASP-19b of WASP-33b, respectively. Nevertheless, Espinoza et al. (2019) reported non-detection of TiO and featureless transmission spectrum of WASP-19b. Nugroho et al. (2017) detected the TiO in the dyaside atmosphere of WASP-33b, though this is still controversial because Nugroho et al. (2019) also reported that the significance of TiO signal reduces when they used new, more accurate line lists of TiO (see also Herman et al. 2020). The sensitivity of the thermal emission spectrum in the properties of model atmospheres might be the cause of this line list problem. Since transmission spectrum is not sensitive to the parameters of model atmosphere compared with thermal emission spectrum, it is a suitable method to detect (or confirm) chemical species in planetary atmospheres. Thus we searched for TiO in the atmosphere of WASP-33b by transmission spectroscopy. Figure 4.1 shows the orbital phase of Nugroho et al. (2017) and this study. Table 4.1 summarizes the basic physical properties of the WASP-33 system.

We describe the observations, data reduction, and removal of systematic components in Section 4.1. The accuracy of used line lists and the cross-correlation technique we applied are explained in Section 4.2. In Section 4.3, we present the results of the analysis. Section 4.4 is devoted to discussions and a summary of this chapter.
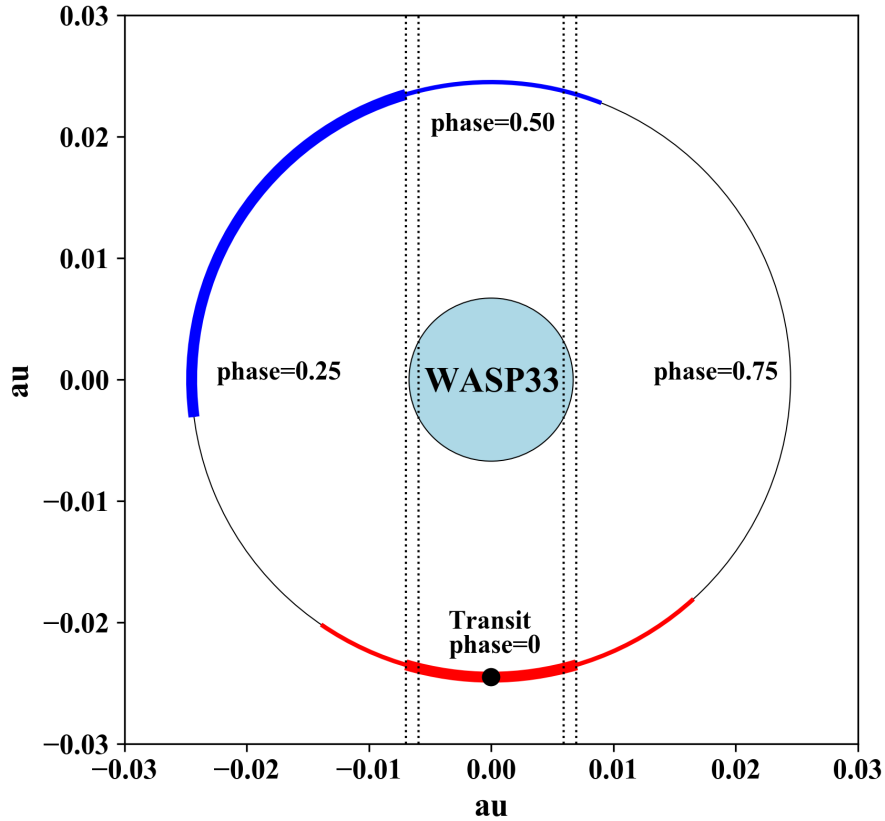


**Figure 4.1**: The orbital phase of WASP-33b observations. Red line shows the observed orbital phase of this study. Since this study is transmission spectroscopy, the planetary signal is only exists in in-transit frames. The red bold line shows the in-transit phase. The orbital phase observed by Nugroho et al. (2017) is shown by blue line. Nugroho et al. (2017) analyzed dayside thermal emission spectrum of WASP-33b, thus the planetary signal was expected to be observed except for the secondary-eclipse phase (bold blue line). Black dot lines show the ingress and egress phases.

| Parameter | Value |
|---|---|
| **WASP-33** | |
| Radius ($R_\odot$) | $1.444 \pm^{0.034}_{0.034}$ [a] |
| Mass ($M_\odot$) | $1.495 \pm^{0.031}_{0.031}$ [a] |
| $T_{\text{eff}}$ (K) | $7430 \pm^{100}_{100}$ [a] |
| log g | $4.3 \pm^{0.2}_{0.2}$ [a] |
| Spectral type | A5 [a] |
| $v \sin i$ (km s$^{-1}$) | $90 \pm^{10}_{10}$ [a] |
| [Fe/H] | $0.1 \pm^{0.2}_{0.2}$ [a] |
| **WASP-33b** | |
| Radius ($R_{\text{Jup}}$) | $1.479 \pm^{0.036}_{0.036}$ [b] |
| Mass ($M_{\text{Jup}}$) | $2.093 \pm^{0.139}_{0.139}$ [c] |
| $T_0$ (BJD) | $2454163.22449 \pm^{0.00016}_{0.00016}$ [b] |
| Period (days) | $1.219870897 \pm^{0.000000079}_{0.000000079}$ [b] |
| Inclination (deg) | $88.5 \pm^{1.1}_{-1.4}$ [b] |
| $K_p$ (km s$^{-1}$) | $232.4 \pm^{2.4}_{2.4}$ |
| $T_{\text{day}}$ (K) | $\sim 3300$ |

Table 4.1:: Basic parameters of WASP-33 and WASP-33b. $K_p$ means the radial velocity semi-amplitude.
a: Collier Cameron et al. (2010), b: Maciejewski et al. (2018), c: Chakrabarty & Sengupta (2019)

# 4.1 Observations and Standard Data Reduction

## 4.1.1 Subaru Observations

We analyzed the archival data of transmission spectroscopy of WASP-33b, which were taken from the SMOKA system (Baba et al. 2002). The data were obtained on the night of Oct 19th, 2011, with the High Dispersion Spectrograph (HDS, Noguchi et al. 2002) on the Subaru telescope. A total of 35 frames were obtained using the standard I2a mode with no iodine cell. The exposure time ranged from 480 to 600 seconds, and a total exposure time was 20760 seconds. The image slicer $\#$ 1 was used, which corresponds to a wavelength resolution of R$\sim$ 110000. The spectra were taken by two (blue and red) CCDs, which contained 26 and 17 orders and covered the wavelengths of 4923–6227 Å and 6340–7660 Å, respectively. The basic information of analyzed data is shown in Table 4.2.

| File name | Exposure (s) | Start time (MJD) |
|---|---|---|
| HDSA00078499 | 600 | 55853.31316525 |
| HDSA00078501 | 600 | 55853.32093039 |
| HDSA00078503 | 600 | 55853.32870272 |
| HDSA00078505 | 600 | 55853.33646997 |
| HDSA00078507 | 600 | 55853.34423255 |
| HDSA00078509 | 600 | 55853.35199838 |
| HDSA00078511 | 600 | 55853.35975809 |
| HDSA00078513 | 600 | 55853.36752462 |
| HDSA00078515 | 600 | 55853.37528363 |
| HDSA00078517 | 600 | 55853.38304947 |
| HDSA00078519 | 600 | 55853.39081242 |
| HDSA00078521 | 600 | 55853.39858660 |
| HDSA00078523 | 600 | 55853.40635175 |
| HDSA00078525 | 600 | 55853.41411667 |
| HDSA00078527 | 600 | 55853.42188505 |
| HDSA00078529 | 600 | 55853.42967588 |
| HDSA00078531 | 600 | 55853.43743894 |
| HDSA00078533 | 600 | 55853.44520373 |
| HDSA00078535 | 600 | 55853.45296633 |
| HDSA00078537 | 600 | 55853.46072696 |
| HDSA00078539 | 600 | 55853.46848966 |

| | | |
|---|---|---|
| HDSA00078541 | 600 | 55853.47625539 |
| HDSA00078543 | 600 | 55853.48402251 |
| HDSA00078545 | 600 | 55853.49178556 |
| HDSA00078547 | 480 | 55853.49955267 |
| HDSA00078549 | 480 | 55853.50592136 |
| HDSA00078551 | 600 | 55853.51228789 |
| HDSA00078553 | 600 | 55853.52005106 |
| HDSA00078555 | 600 | 55853.52781573 |
| HDSA00078557 | 600 | 55853.53557866 |
| HDSA00078559 | 600 | 55853.54334388 |
| HDSA00078561 | 600 | 55853.55110867 |
| HDSA00078563 | 600 | 55853.55887253 |
| HDSA00078565 | 600 | 55853.56664126 |
| HDSA00078567 | 600 | 55853.57441383 |

Table 4.2:: Basic information of analyzed data. The sky was clear and the atmospheric seeing was $\sim$ 0.6 arc-seconds according to the summit log on the observation night.

## 4.1.2 Standard data Reduction

We conducted a standard reduction of the data by IRAF tools and *hdsql*, provided by the team of HDS[1]. First, we performed an overscan correction, removed the bias, and converted the analog digital unit to electron numbers. We made mask frames of the bad columns for each CCD. These processes were performed by *hdsql*. The aperture position of each order was determined by *apall* using a flat frame taken with a narrow slit length. Scattered light was then subtracted by the IRAF task *apscatter*. We did not conduct scattered light subtraction for the flat frame of the blue CCD because the distance of orders was narrow for the flat frame of the blue CCD. Using 50 flat frames, we generated a median flat frame with a non-linearity correction (Tajitsu et al. 2010). To remove the fringe pattern on the spectrum, we normalized the flat frame by *apnormalize*. Since the data was obtained with the image slicer, we used *hdsis_ecf.cl*, which is a cl script provided by HDS team, to do flat-fielding and extract 1-D spectrum. In this script, the science and flat 2-D data are sliced along the slit directions with a width of one pixel from -16 to +13 pixels

---

[1]https://www.naoj.org/Observing/Instruments/HDS/hdsql-e.html

for the blue CCD and -15 to +13 pixels for the red CCD to the center of the each order. Each sliced spectrum was divided by the corresponding sliced flat spectrum. The profile of the image slicer along the slit length was also estimated by taking the average of sliced flat spectrum. Finally, 1-D spectrum was obtained by combining all sliced and flat-fielded spectra with the correction of the estimated profile of the image slicer. The grid of the wavelength was derived by the IRAF task *ecidentify* using thorium–argon arc lump spectra, which were taken at the beginning and end of the night. We assigned the wavelength grid to each object frame by *refspectra* and *dispcor*. We conducted these reductions to the median flat frame as well as the object frames to estimate the blaze function of each order. We divided the object spectra by the estimated blaze function using *sarith*. The spectrum contains several regions affected by bad columns that were not completely removed by the reduction with the CL script. Because these bad regions can be problematic for analysis, we identified the bad regions by visual inspection and masked them.

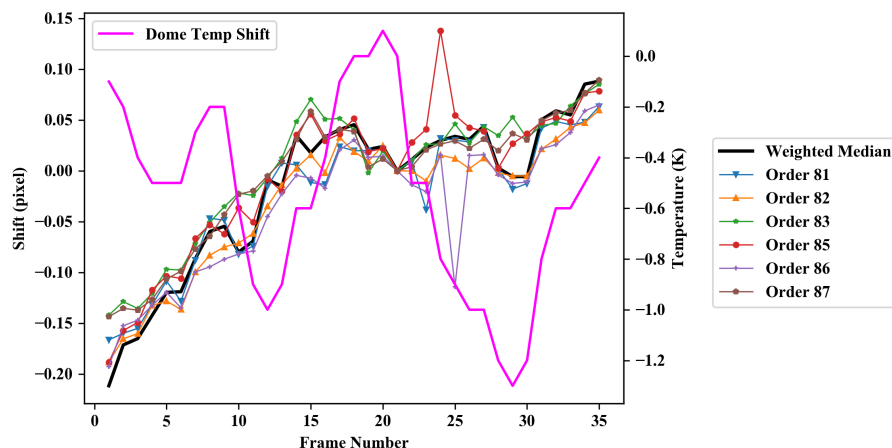### 4.1.3 Transmission spectrum matrix



**Figure 4.2**: Relative shift owing to instrumental variation. The black solid line is the weighted median shift of the five orders where a sufficient telluric line exists. The magenta line shows the variations of the dome temperature.

Since many of reduction and analysis procedures in this chapter are similar in Chapter 3, we use the same denotations as Chapter 3 in this chapter. We corrected the variations of blaze function in the same manner as Chapter 3. Then, we estimated the instrumental drift during the observation by telluric absorption lines. The cross-

correlation function was computed from the velocity difference of $-20$ km s$^{-1}$ to 20 km s$^{-1}$ with a 0.1 km s$^{-1}$ step. The peak of the CCF was derived by fitting a Gaussian to the CCF. The instrumental shift derived by the above procedure is shown in Figure 4.2. Unlike in Chapter 3, the correlation of the instrumental drift and the dome temperature was not clear. The reason is unsure, though variations of other observation conditions might induce the drift. We shifted $S_{\mathrm{raw}}$ with spline interpolation. We conducted a 5-sigma clipping to remove bad pixels and cosmic rays and obtained $F_{\mathrm{Earth}}$.

We also measured the systemic velocity of WASP-33 by cross-correlation of the model transmission spectrum. We used Coelho et al. (2005) to make the model stellar spectrum. We convoluted a Gaussian function with a width of 90 km s$^{-1}$ to take rotational broadening into account, and we measured the apparent radial velocity of WASP-33 in each frame by the CCF with the stellar model spectrum. We fitted a Gaussian to the CCF and used the center position of the best-fit Gaussian as the stellar radial velocity in each frame.

The result is shown in Figure 4.3. We obtained $V_{sys}$ = -2.58$\pm_{0.32}^{0.32}$ km s$^{-1}$, and this is consistent with the literature data from Collier Cameron et al. (2010) and Nugroho et al. (2017). In this study, we use this value as the systemic velocity of WASP-33.

The stellar radial velocities in Figure 4.3 seems to have periodical variations. This would come from the stellar pulsation, since WASP-33 is a Delta-Scuti variable. Delta-Scuti variables have both radial and non-radial pulsations, thus the stellar line profile varies over time. To check the stellar pulsations, we normalized $F_{\mathrm{Earth}}$ by its mean spectrum, and calculated CCF matrix of it with the model stellar spectrum. The definition of CCF map is the same as Chapter 3, namely

$$C[i, \delta v] = F[i] \star M(\delta v),$$

where $i$ denotes the frame number, $\star$ is the cross-correlation operator, and $M(\delta v)$ is the model spectrum shifted by $\delta v$. Figure 4.4 shows the CCF matrix. We note that we used a model stellar spectrum without a convolution of a Gaussian function for rotational broadening to make the variations of the stellar line profile clear.

We can clearly see the Doppler shadow from the upper left to the lower right. We considered that the bright signals from the lower left to the upper right were caused by stellar pulsations. We note that these strange features are not peculiar to this dataset, but similar features can be seen in other datasets (e.g. Collier Cameron et al. 2010). Due to this features, it is quite difficult to search for vaporized metals in the atmosphere of WASP-33b by transmission spectroscopy. This is because the stellar spectrum also has absorption lines of vaporized metals with the time-varying line profile. Therefore, we focus on searching for TiO in this thesis. We note that detailed
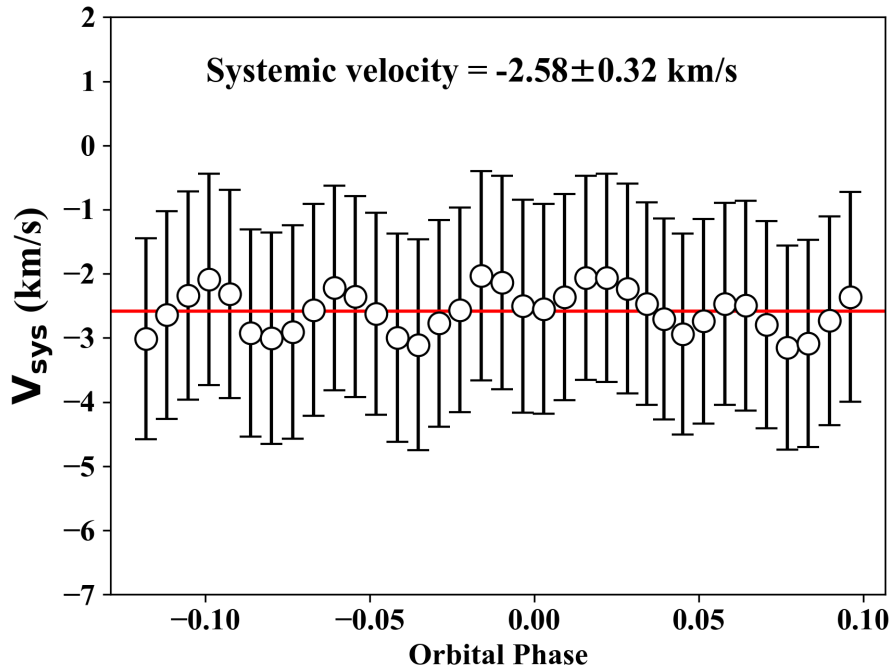
**Figure 4.3**: Systemic velocity of WASP-33. For each frame, we calculated CCF and determined the radial velocity order by order, and we used the standard error of the mean as the error bar of the radial velocity of each frame. Barycentric radial velocity of Earth and the radial velocity variation caused by WASP-33b were corrected. $V_{sys}$ was calculated by taking the weighted mean of radial velocities of all frames (red line).

modeling of the stellar line profiles might enable us to probe metals in the atmosphere of WASP-33b by transmission spectroscopy. Thermal emission spectroscopy would also be effective, because the planetary signals are shifted by $\gtrsim 100$ km s$^{-1}$ due to the orbital motion and can be distinguished from the stellar lines.

## 4.1.4 Removal of stellar signals and telluric absorption

Since it is difficult to measure the stellar radial velocity in each frame precisely due to the pulsation, we did not shift the $F_{\mathrm{Earth}}$ to the spectrum matrix in the stellar rest frame ($F_{\mathrm{stellar}}$). We used the SYSREM algorithm to remove the residuals from the stellar and telluric absorption lines (Tamuz et al. 2005, Mazeh et al. 2007). We applied SYSREM to $F_{\mathrm{Earth}}$ with fifteen iterations. Thus, we obtained 3-dimensional
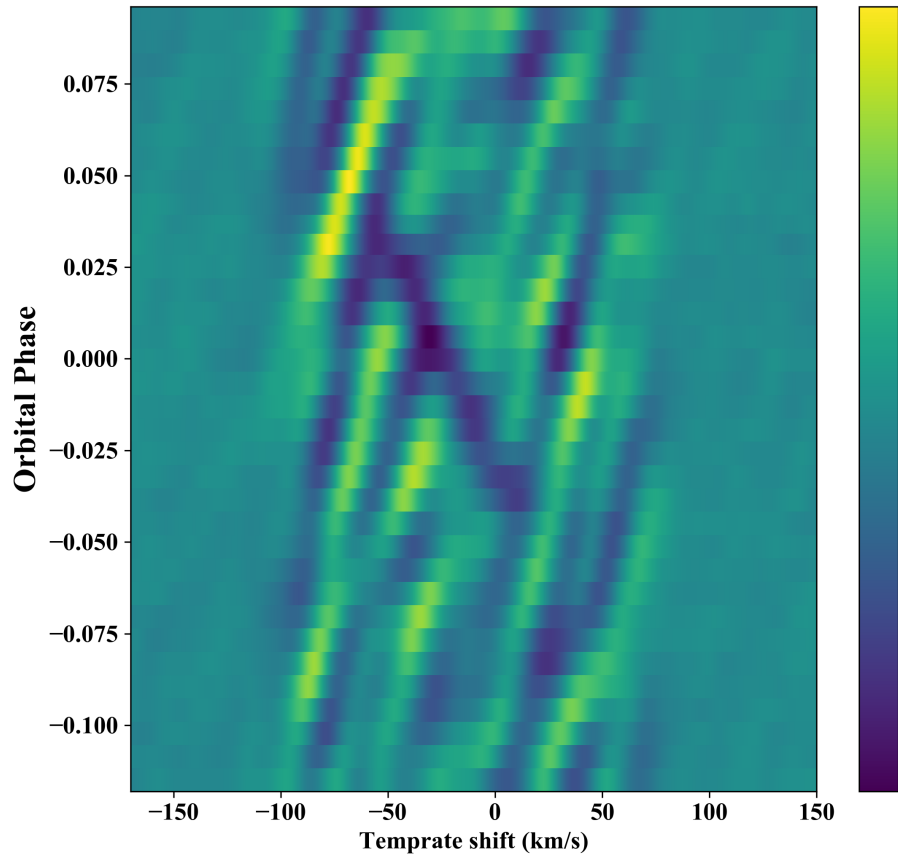
**Figure 4.4**: Pulsations of WASP-33 seen in the CCF matrix of normalized $F_{\mathrm{Earth}}$ and the model stellar spectrum. The black shadow from the upper left to the lower right is the Doppler shadow caused by WASP-33b.

$F_{\mathrm{SYS}}[s, i, \lambda]$ for all of the echelle orders, with dimensions of sixteen (denoted by $s$ and ranging from 0 to 15 SYSREM iterations) $\times$ 35 (frame number, denoted by $i$) $\times$ the number of wavelength bins.

As described in Chapter 3, a technique of injection of artificial planetary signals to find the optimal iteration number for each order might lead to biased results. Therefore, we used a common iteration number for all the orders with the highest S/N.

## 4.2 Cross-correlation analysis

### 4.2.1 Model spectra for the cross-correlation analysis

We calculated model transmission spectra in similar manner as described in Chapter 3. We generated the model transmission spectra for the cross-correlation template of TiO with three TiO line lists: the line list from Plez (1998) (Plez-1998), updated version of Plez-1998 (Plez-2012), and the line list from McKemmish et al. (2019) (Toto). We included a continuum absorption cross section of $H^-$ and Rayleigh scattering by H and $H_2$. We used HELIOS-K (Grimm & Heng 2015) to compute the cross section. We considered the five most abundant isotopes, $^{46}Ti^{16}O$, $^{47}Ti^{16}O$, $^{48}Ti^{16}O$, $^{49}Ti^{16}O$, $^{50}Ti^{16}O$ and combined them with the natural isotope ratio. We assumed the solar metallicity and element abundance, and calculated the abundance of TiO at each layer assuming chemical equilibrium by *FastChem* (Stock et al. 2018).

The typical variation of the radial velocity of WASP-33b due to the orbital motion is $\sim$ 8 km s$^{-1}$ per frame. This value is lager than the spectral resolution of this observation ($\sim$ 2.7 km s$^{-1}$). Observed planetary signal is expected to be smeared by this variation of the radial velocity. We convoluted a Gaussian function for instrumental spectral resolution and a boxcar function for the smearing effect to the model transmission spectrum.

### 4.2.2 Line List Accuracy

To confirm the accuracy of three line lists, we made model M-dwarf emission spectra with three line lists and compared with a observed M-dwarf spectrum. We assumed a 1-D plane parallel atmosphere from $P_0 = 100$ bar to $P_1 = 10^{-5}$ bar. The number of layers was 50, and layers were evenly spaced in the log pressure. The temperatures constantly lapse from $T_0 = 4000$ K at $P_0$ to $T_1 = 2600$ K at $P_1$. We assumed the local thermodynamic equilibrium and no scattering and absorption by TiO only. The model emission spectrum was calculated by integrating the Schwarzschild equation

$$I(\nu) = \sum_i B(\nu, T_i) e^{-\tau_i(\nu)} \Delta\tau, \qquad (4.1)$$

where $i$ denotes the layer number counted from the ground, $T_i$ is the temperature of $i$-th layer, and $B(\nu, T_i)$ is the black body spectrum.

We used a spectrum of HD 275122 (spectral type : M1.5, Lépine et al. 2013) obtained on the night of Oct 15th, 2012 with HDS. This spectrum was obtained with the same

wavelength resolution and I2a setting as the data of WASP-33b. The data was taken from SMOKA. We reduced the data in the same manner for data of WASP-33b, and calculated (normalized) cross correlation function (CCF) of the spectrum and the model M-dwarf emission spectrum order by order. This is a standard method to check the accuracy of line lists (e.g., Hoeijmakers et al. 2015, Nugroho et al. 2017, McKemmish et al. 2019).

Figure 4.5 to 4.7 show the result. As shown in previous research, there is no visible peak at shorter wavelength with Plez-1998; Plez-1998 is inaccurate at shorter wavelength ($\lesssim$ 6400 Å). We can also see slight shifts from the expected stellar radial velocity in orders with visible peaks. The cause of these shifts are unsure. However, given that there is no apparent shifts in other two line lists, this would also come from the inaccuracy of Plez-1998.

Both of Plez-2012 and Toto are more accurate than Plez-1998, especially at shorter wavelength. Although CCFs of some orders are featureless, we can see peaks at the expected radial velocity in many orders. We set a criteria of a normalized CCF peak value > 0.2 to determine which orders were used in further analysis (shown by blue-shaded panels). We note that the CCF peak value does not necessarily represent the accuracy of the line list. For example, CCF peak values are reduced by absorption lines of other chemical species in the observed spectrum. In addition, we used a simple model atmosphere to calculate the model M-dwarf spectrum, therefore this might also affect the CCF peak value. Thus, orders with weak CCF peak (< 0.2) might not be inaccurate compared with other orders. Considering these facts, our criteria is rather a conservative one.
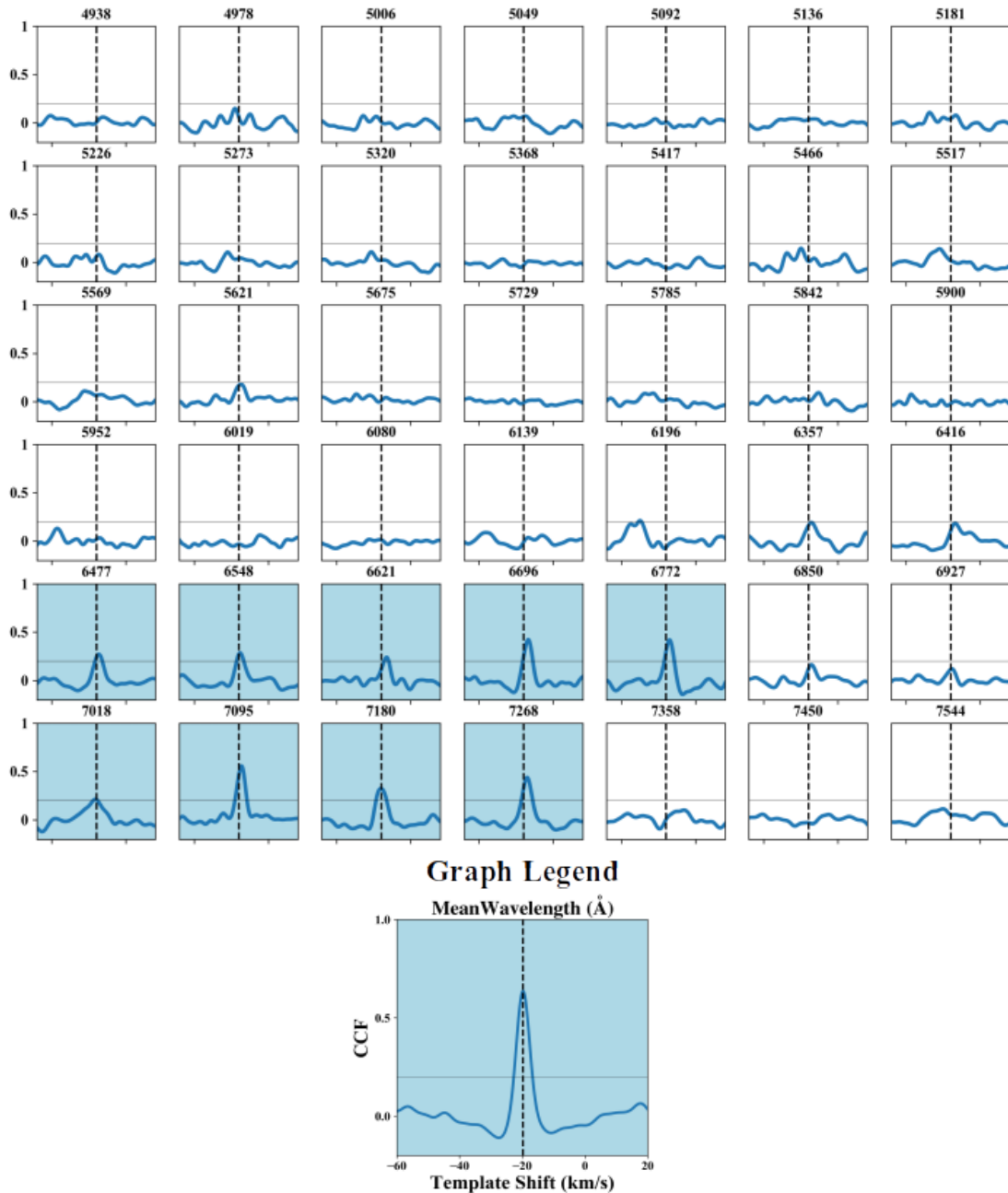
**Figure 4.5**: Line lists accuracy check for the Plez-1998 line list. Each
panel shows the cross correlation function of the model M dwarf spec-
trum and the observed M dwarf spectrum of each echelle order. The
mean wavlength of the order is shown above each panel. The vertical
black dotted lines show the expected radial velocity of HD 275122. Hor-
izontal gray lines show the criteria of 0.2. Blue-shaded panels represent
orders which were used in further analysis. We did not use the echelle
order 78 due to the heavy telluric contamination, thus this order is not
shown.
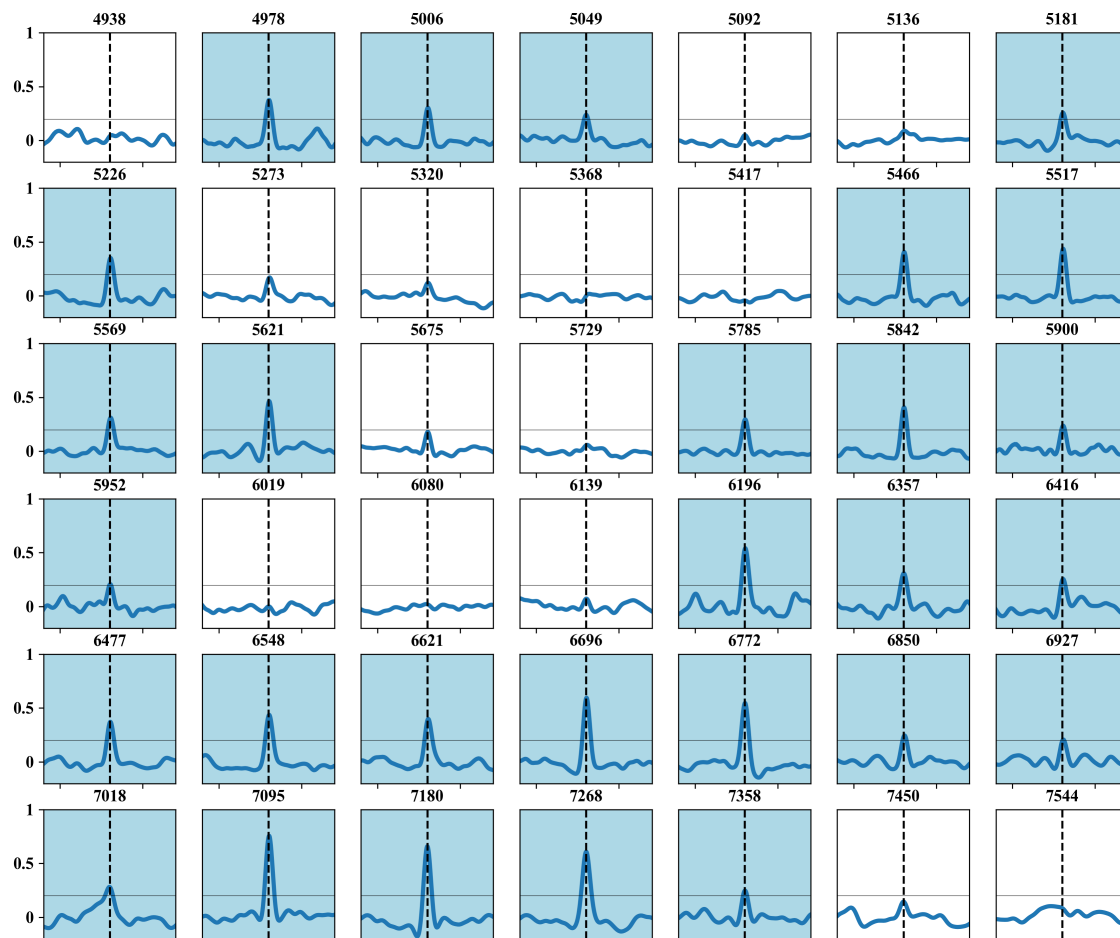
**Figure 4.6**: Line lists accuracy check for the Plez-2012 line list.
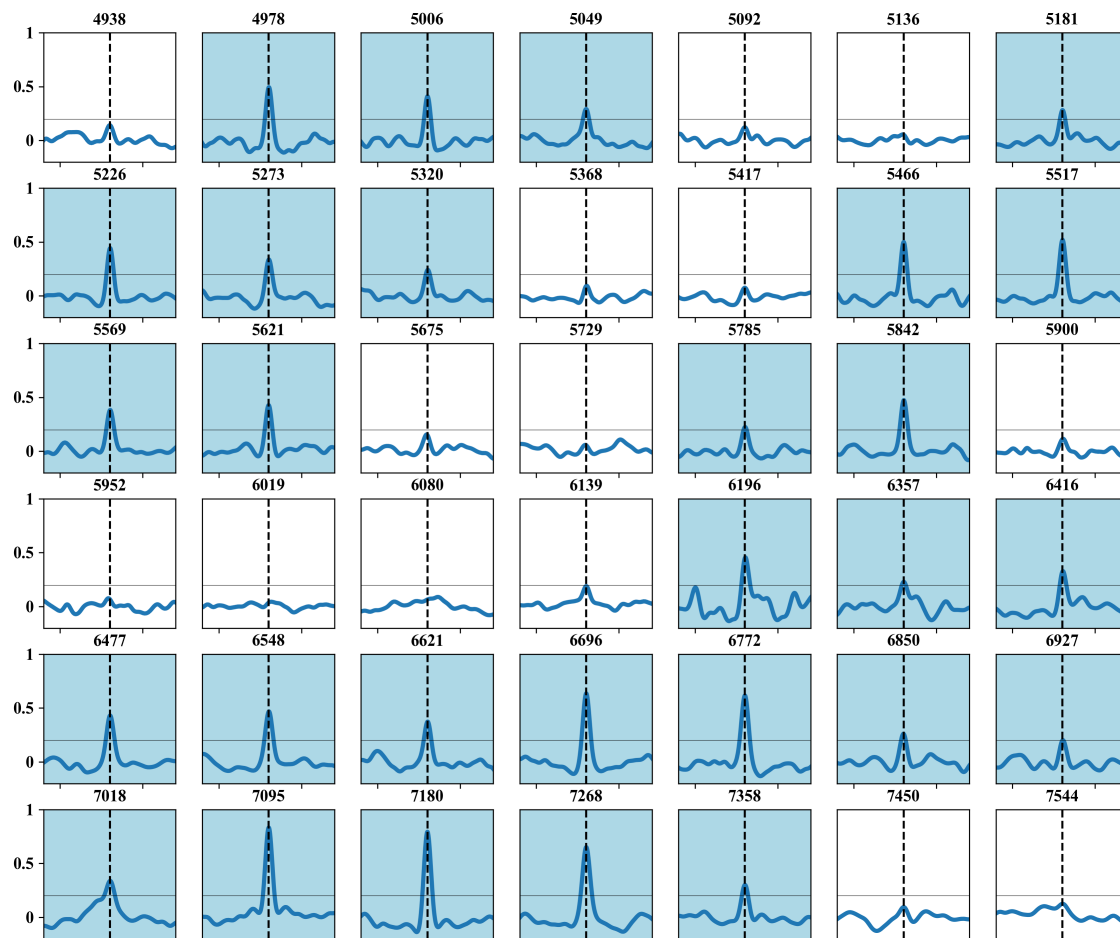
**Figure 4.7**: Line lists accuracy check for the Toto line list.

### 4.2.3 Cross-correlation and SN map

We shifted the model spectra from $-426.5$ km s$^{-1}$ to $369.5$ km s$^{-1}$ with a step size of 1 km s$^{-1}$, corresponding to a systemic velocity ($V_{sys}$ ranging from $-100$ km s$^{-1}$ to $100$ km s$^{-1}$ and the semi-amplitude of the planetary radial velocity ($K_p$) from 0 to $350$ km s$^{-1}$ .

We computed $C^{\mathrm{model}}[s, i, \delta v]$ as a function of $F_{\mathrm{SYS}}$ and a shifted model spectrum of each template spectrum (denoted by $M_{\mathrm{model}}$) as described in Chapter 3 as

$$C^{\mathrm{model}}[s, i, \delta v] = \sum_k \frac{F_{\mathrm{SYS}}[s, i, k] M_{\mathrm{model}}(\delta v)[k]}{\sigma_k^2},$$

.

Then, we summed $C^{\mathrm{model}}$ for the orders which were determined for each line list in the previous section.

We obtained $C^{\mathrm{atom}}$, whose dimensions are 35 (frame number) $\times$ 797 (radial velocity from $-426.5$ km s$^{-1}$ to $369.5$ km s$^{-1}$) for each SYSREM iteration number. Then we computed the CCF map in the $K_p$-$V_{sys}$ plane as follows: we integrated $C^{\mathrm{model}}[s]$ (in the frame - radial velocity plane) along the path of expected planetary radial velocity $RV_p$ using

$$RV_p = K_p \ \sin(2\pi\phi(t)) + V_{sys} + \delta_{rvor},$$

where $\delta_{rvor}$ is the calculated barycentric radial velocity of Earth.

As described in Chapter 3, we also calculated the expected amount of starlight blocked by the planet for each frame by *batman*(Kreidberg 2015), and used it as a weighting coefficient with a $K_p$–$V_{sys}$ integration. We divided the CCF map by the standard deviation of the map after excluding the expected position of the planetary signal to make the S/N map and region with $|K_p| < 100$ km s$^{-1}$. We also calculated the detection significance by the phase shuffling method (e.g., Esteves et al. 2017).

## 4.3 Results

We detected TiO signal with model spectra using Plez-2012 and Toto. Figure 4.8 shows the S/N of detected signal with SYSREM iteration number. The highest signal was detected with a model spectrum with Plez-2012 line list with 8 SYSREM iteration. Therefore, hereafter we use 8 SYSREM iteration to compare the results of three line lists.
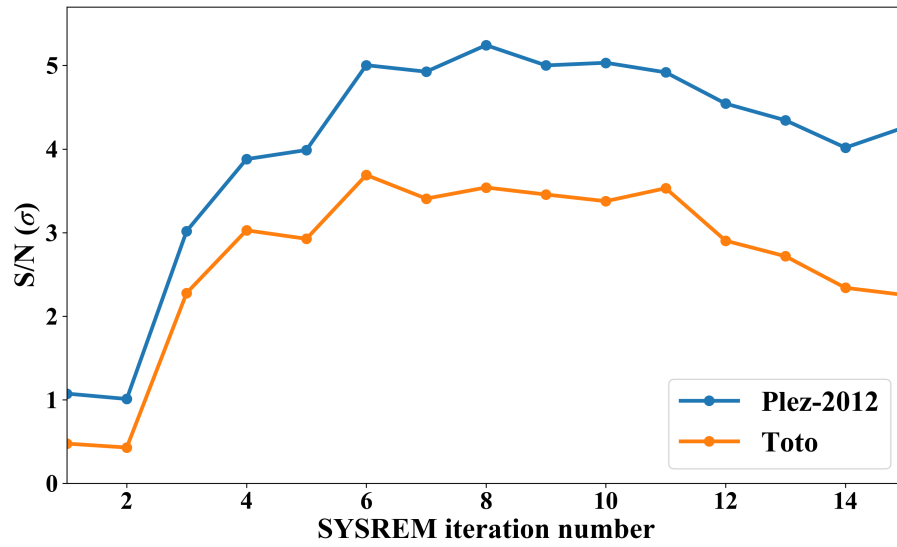
**Figure 4.8**: S/N of detected signal with SYSREM iteration number.
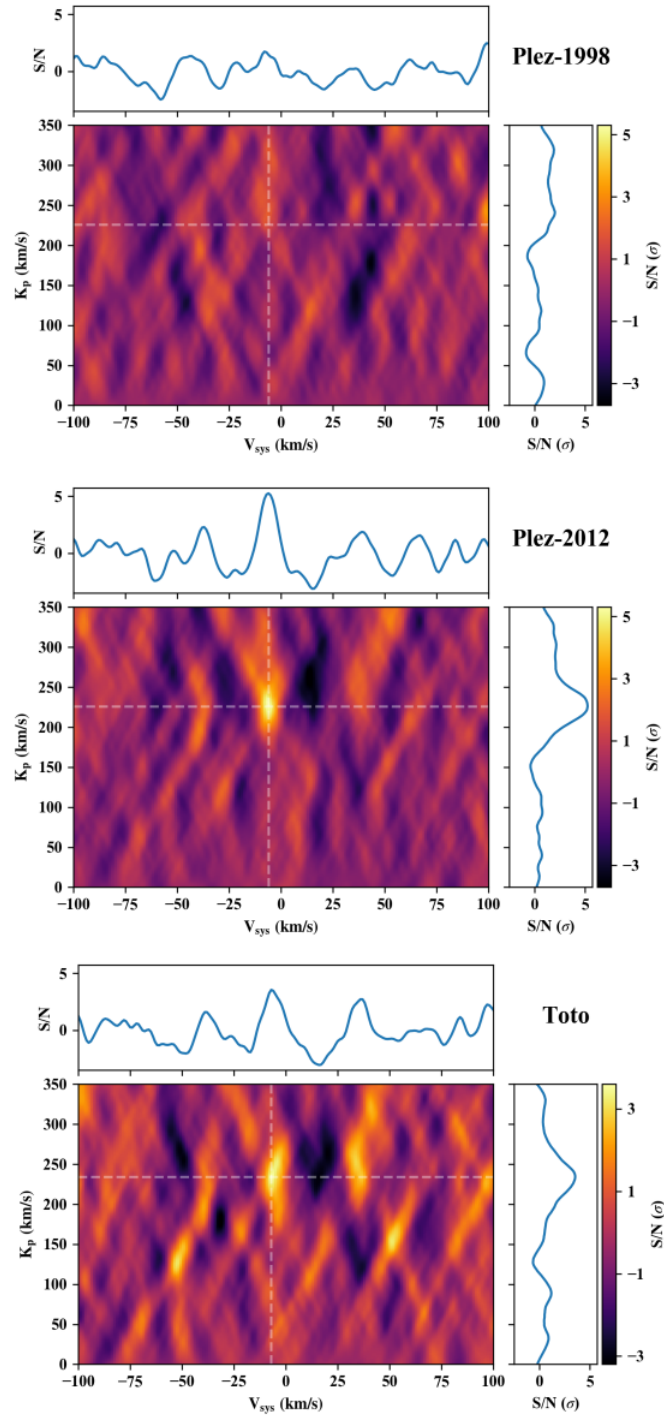
**Figure 4.9**: S/N map of three line lists with 8 SYSREM iterations. The used line list for each model spectrum is shown in upper right of the each S/N map. We note that the color scale of S/N map for Toto is different to make the detected peak easy to see.

Figure 4.9 shows the S/N map with the three line list. S/N values for the detected signals were 5.2 and 3.5. The detection significances calculated by the phase shuffling method were 4.6 and 3.7, respectively. The peak positions of detected signals were $K_p= 226\pm^{17}_{14}$ km s$^{-1}$, $V_{sys}= -6\pm^2_2$ km s$^{-1}$ for Plez-2012, and $K_p= 234\pm^{22}_{30}$ km s$^{-1}$, $V_{sys}= -7\pm^4_2$ km s$^{-1}$ for Toto. These values were consistent with the value of $K_p$ and $V_{sys}$ reported by Nugroho et al. (2017) (see Table 4.3).

| Model | $K_p$ (km s$^{-1}$) | $V_{sys}$ (km s$^{-1}$) | S/N | $\sigma_{\text{shuffle}}$ |
|---|---|---|---|---|
| Plez-2012 | $226.0\pm^{17}_{14}$ | $-6\pm^2_2$ | 5.2 | 4.6 |
| Toto | $234\pm^{22}_{30}$ | $-7\pm^4_2$ | 3.5 | 3.7 |
| Plez-1998 (Nugroho et al. 2017) | $237.5\pm^{13.0}_{5.0}$ | $-1.5\pm^{4.0}_{-10.5}$ | 4.8 | N/A |

Table 4.3:: Positions, S/N, and significance of detected peaks of TiO in the $K_p$–$V_{sys}$ plane. The detection significance was estimated by the phase-shuffling method (Esteves et al. 2017). Values reported by Nugroho et al. (2017) were also shown for comparison.

As seen in Figure 4.9, TiO signal was not detected with model spectrum using Plez-1998.
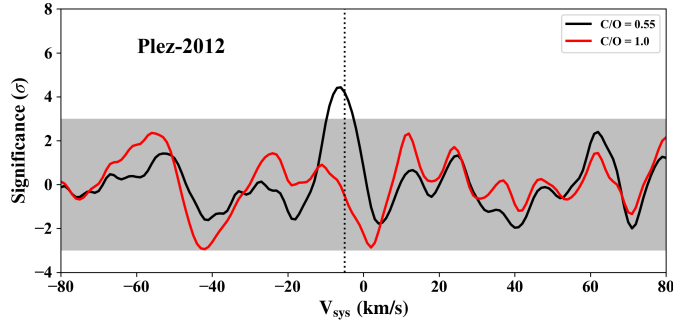
## 4.4    Discussion and Summary



**Figure 4.10**: Results of injection test of TiO with Plez-2012 line list under chemical equilibrium with a C/O value of 0.55 (solar) and 1.0 after 8 SYSREM iterations.

## 4.4.1   Detection of TiO

TiO in the atmosphere of WASP-33b was detected with model spectra using Plez-2012 and Toto, though not with the model spectrum using Plez-1998. This is not surprising because Plez-1998 is not accurate in the majority of the wavelength range of this dataset.[2] The detection significances with model using Plez-2012 and Toto were moderately different (see Figure 4.9). Both line lists have been confirmed to agree with TiO features in the spectra of M-dwarf by several studies including this study (e.g. McKemmish et al. 2019). Piette et al. (2020) pointed out the importance of experimentally-derived energy levels or transition for complex molecule like TiO. Both Plez-2012 and Toto include the experimentally-derived energy levels and transitions (not all). Actually, Plez-2012 is an updated version of Plez-1998 to include the experimentally-derived energy levels. The importance of experimental data was shown by the line list accuracy check in this study. It is possible that some of not experimentally-derived transitions are not enough accurate for high-resolution spectroscopy and affect the detection significance. Since the planetary signal is weak and we considered TiO features only in the model transmission spectrum, our results do not necessarily indicate that Plez-2012 is more suitable for high-resolution spectroscopy than Toto. However, considering Nugroho et al. (2017), TiO have been detected by both of emission spectroscopy and transmission spectroscopy with three kinds of line lists and two dataset. This study showed the robust detection of TiO in the atmosphere of WASP-33b.

We also conducted the injection test of TiO to consider the C/O ratio of WASP-33b with the Plez-2012 line list. Since the TiO signal was detected, we excluded frame 19 and 20 which the injected signal ($K_p$ = -235 km s$^{-1}$, $V_{sys}$ = -5 km s$^{-1}$) was overlapped with the detected signal. As shown in Figure 4.10, if the C/O ratio of the atmosphere of WASP-33b is $\gtrsim$ 1, it would be difficult to detect TiO by our analysis. This suggests the C/O ratio of the atmosphere of WASP-33b is lower than 1. However, note that it is difficult to constrain the formation history from the information that the C/O ratio < 1.

## 4.4.2   Distribution of TiO

Given the detection of TiO features in thermal emission spectrum by Nugroho et al. (2017), TiO exists in both of dayside and the terminator region of WASP-33b's at-

---

[2]The wavelength range of the data used in this study was $\sim$ 500 – 760 nm, and that of Nugroho et al. (2017) was $\sim$ 620 – 880 nm

mosphere. In principle, the altitudes of atmosphere probed by thermal emission and transmission are different; transmission spectroscopy probes upper atmosphere compared with thermal emission spectroscopy. The weight function of thermal emission $W_{thermal}(z)$ is defined in the integral of the Schwarzchild equation as

$$
\begin{aligned}
I(\nu) &= \int_0^z B(\nu, T(z)) \mathrm{e}^{-\tau(\nu,z)} \left| \frac{\partial \tau}{\partial z} \right| dz \\
&= \int_0^z B(\nu, T(z)) W_{thermal}(\nu, z) dz \\
W_{thermal}(\nu, z) &= \mathrm{e}^{-\tau(\nu,z)} \left| \frac{\partial \tau}{\partial z} \right|
\end{aligned}
\tag{4.2}
$$

where $z$ is the altitude. As seen in the above equation, observed spectrum is the integral of black body radiation of each layer weighted by $W_{thermal}(z)$. Therefore, $W_{thermal}(z)$ represents the contribution of the layer with the altitude of $z$ to the observed thermal emission spectrum. Since the transmittance $T(\nu, z)$ from the layer with the altitude of $z$ to the observer at the frequency of $\nu$ is $\mathrm{e}^{-\tau(\nu,z)}$, the weight function is also expressed as

$$
W_{thermal}(\nu, z) = \left| \frac{\partial T(\nu, z)}{\partial z} \right| = \left| \frac{\partial}{\partial z} \mathrm{e}^{-\tau(\nu,z)} \right|
\tag{4.3}
$$

The weight function has a peak at $\tau \sim 1$, therefore we mainly observe the thermal emission from the layer with optical depth $\sim 1$. For transmission spectroscopy, the transmittance of planetary atmosphere at the altitude of $z$ at the frequency of $\nu$ is $\mathrm{e}^{-\tilde{\tau}(\nu,z)}$. Thus, we defined the weight function of transmission spectrum $W_{trans}(z)$ as

$$
\begin{aligned}
W_{trans}(\nu, z) &= \left| \frac{\partial}{\partial z} (\mathrm{e}^{-\tilde{\tau}(\nu,z)}) \right| \\
&= \mathrm{e}^{-\tilde{\tau}(\nu,z)} \left| \frac{\partial \tilde{\tau}}{\partial z} \right|
\end{aligned}
\tag{4.4}
$$

To estimate where we probed by thermal emission spectroscopy and transmission spectroscopy, we calculated the $W_{themal}(\nu, z)$ and $W_{trans}(\nu, z)$ of model atmosphere. For $W_{trans}$, we used the $\tilde{\tau}(\nu, z)$ for Plez-2012 model. We also calculated the optical depth of model dayside atmosphere of WASP-33b. We assumed a 1-D plane parallel atmosphere from $P_0 = 10$ bar to $P_1 = 10^{-15}$ bar. The number of layers was 100 and layers were evenly spaced in the log pressure, which is the same for the model atmosphere of the transmission. The temperatures constantly increase from $T_0 = 2500$ K at $P_0$ to $T_1 = 3500$ K at $P_1$; we assumed a dayside atmosphere with a simple thermal inversion. Then, we calculated the optical depth of thermal emission and converted it to $W_{themal}(\nu, z)$.
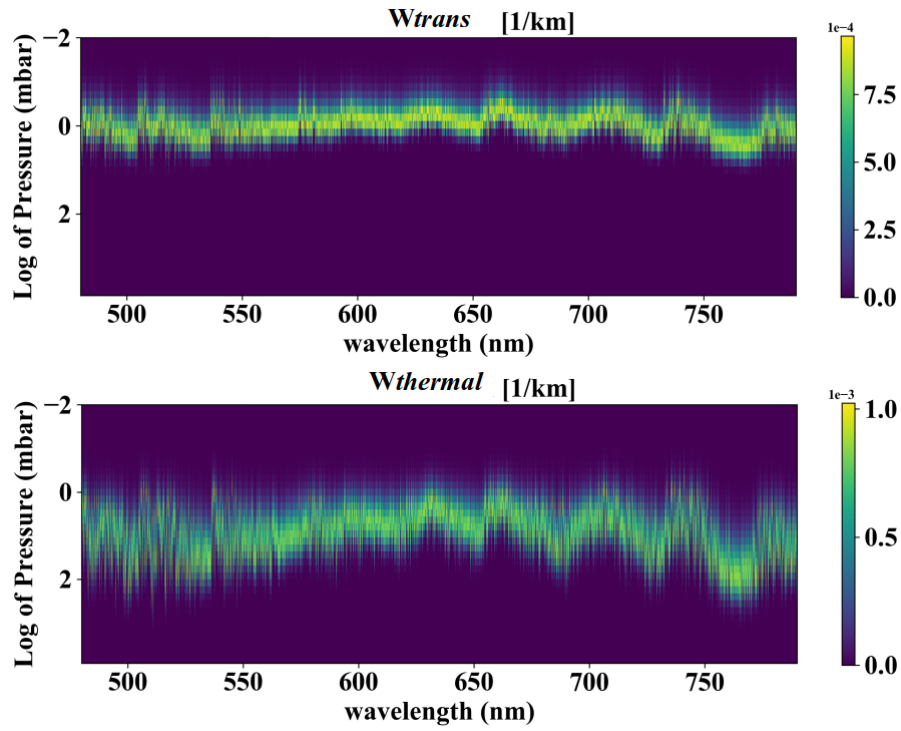
**Figure 4.11**: Weight functions of thermal emission and transmission spectrum.

Figure 4.11 shows the weight functions for model thermal emission and transmission spectrum. The pressure of region probed by transmission spectroscopy is roughly one or two order of magnitude lower than that of thermal emission spectroscopy. Figure 4.12 shows the schematic view of the probed region by this study and that of Nugroho et al. (2017) assuming tidal lock.
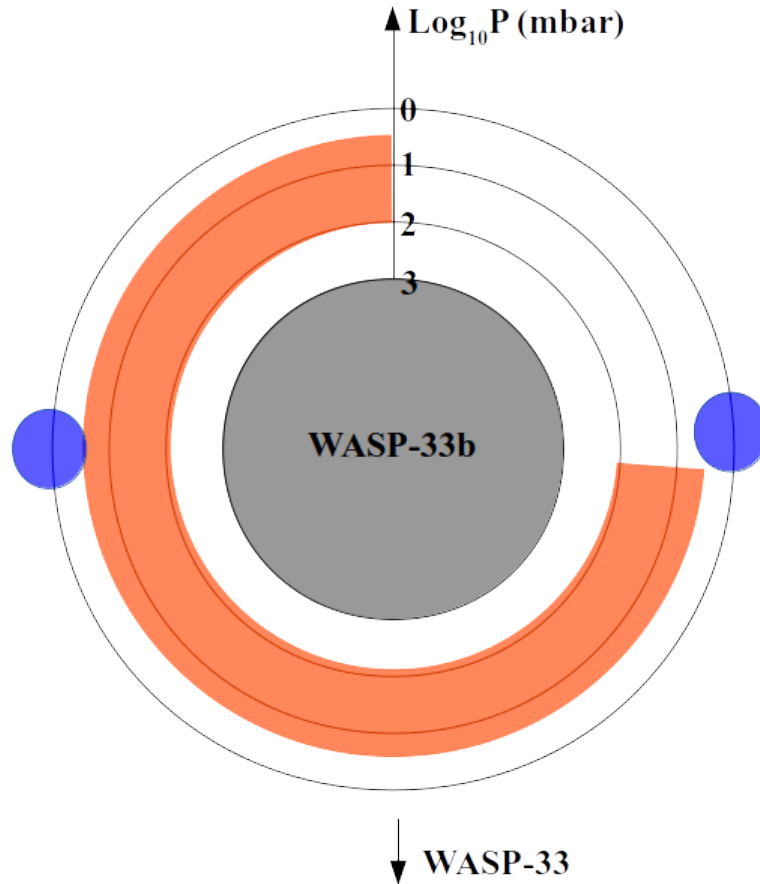
**Figure 4.12**: Schematic view of the probed region of the WASP-33b's atmosphere. We assumed that WASP-33b is tidally locked. Nugroho et al. (2017) observed the orbital phase from 0.23 to 0.56 (see Figure 4.1). Orange region represents the probed region by Nugroho et al. (2017). Blue region represents the probed region by this study. We note that TiO does not necessarily exist in all over the regions.

This study shows the existence of TiO in the terminator of WASP-33b's atmosphere. Now TiO seems to exist widely ($\sim$ 100 mbar to 10 mbar in the dayside and $\sim$ 1 mbar at the terminator) in the atmosphere of WASP-33b. The detected signal with Plez-2012 was blue-shifted from the systemic velocity by $\sim -3.5\pm^2_2$ km s$^{-1}$. Given that WASP-33b is expected to have fast rotational velocity ($\sim$ 6 km s$^{-1}$) and the significance of the blue-shift is $\lesssim 2\sigma$, it is difficult to constrain the origin of this blue-shift . Nevertheless, the amount of blue-shift is consistent with the typical wind speed from dayside to nightside by theoretical studies (a few km s$^{-1}$, e.g. Kataria et al. 2016) and TiO also exists in the dayside atmosphere. Possibly this is the

detection of TiO carried from the dayside by strong winds in the atmospheres of hot-Jupiters. However, further observations and detailed modeling is required to figure out the atmospheric dynamics of WASP-33b.

### 4.4.3 Summary

Up to now, Sedaghati et al. (2017) and Nugroho et al. (2017) have reported the TiO in the atmosphere of WASP-19b and WASP-33b, respectively. Given that Espinoza et al. (2019) reported non-detection of TiO in the atmosphere of WASP-19b, Nugroho et al. (2017) was the only one robust detection of TiO in the planetary atmosphere, though there was a problem concerning line lists. Our results strongly support the TiO detection by Nugroho et al. (2017). Nugroho et al. (2017) detected emission features of TiO, which suggests the existence of a thermal inversion in the atmosphere of WASP-33b. Our confirmation of TiO existence in the atmosphere of WASP-33b will provide important information to understand atmospheric structures of hot-Jupiters.

# Chapter 5

# Conclusion and Future Prospects

## 5.1 Discussion based on the results of the two targets

We have presented the results of high resolution optical transmission spectra of two UHJs: HD149026b and WASP-33b. One obstacle in high resolution spectroscopy is clouds in planetary atmospheres. For cooler hot-Jupiters, it is difficult to constrain the abundance of chemical species from non-detection, because the existence of clouds may obscure features of the chemical species. The high temperatures of UHJs hinder cloud formation. The dayside temperature of HD149026b is $\sim$ 2150 K and that of WASP-33b is $\sim$ 3300 K. We excavated data of UHJs from archived data, and successfully detected planetary signals and obtain information of chemical species of their atmospheres.

The first detection of neutral titanium in the atmosphere of HD149026b demonstrated the diverse chemical composition of hot-Jupiters. The non-detection of TiO is also indicative. Now TiO is only detected in extremely hot-Jupiters like WASP-33b (Nugroho et al. 2017 and this thesis) and possibly WASP-19b (dayside temperature $\sim$ 2500K, Sedaghati et al. 2017, but see Espinoza et al. 2019), and cold-trap effect (Spiegel et al. 2009, Parmentier et al. 2013) is considered as one of the possible explanations for non-detection of TiO in atmospheres of cooler hot-Jupiters. TiO depletion by supersolar C/O ratio has also been suggested (e.g. Madhusudhan 2012), though it is difficult to distinguish these scenarios. Our detection of neutral titanium suggests that titanium is not depleted in the upper atmosphere of HD149026b. Our results observationally showed the possibility that the non-detection of TiO until now might be partially due to a supersolar C/O ratio of planetary atmospheres.

Since most of attempts to detect TiO in planetary atmospheres failed and there were some controversial points in the previous detection of TiO, our detection of TiO in the terminator region atmosphere of WASP-33b proved that TiO can exist in planetary atmospheres.

We have detected neutral titanium in the atmosphere of HD149026b and TiO has not been detected. On the other hand, we have detected TiO in the atmosphere of WASP-33b. Generally, TiO becomes dominant among chemical species that contain titanium as the temperature decreases in chemical equilibrium. Our results indicate that it is important to consider various properties (not only the temperature but also C/O ratio and so on) of atmospheres. Our studies also prove that the investigation of metals and their compounds is a powerful tool to study atmospheres of UHJs. Since the dominant form of metals is affected by the atmospheric environments such as temperature or C/O ratio, we can learn them by detection or non-detection of metals and their compounds. This method becomes available owing to the recent detection of metals in planetary atmospheres and improvement of molecular line lists. We established this method by high resolution spectroscopy.

Since we investigated only two targets, it is difficult to consider universal properties of UHJs' atmospheres. However, we have shown that C/O ratio in HD149026b and WASP-33b would be different by detection and non-detection of TiO. It suggests that these two targets might have been formed by different formation processes. Our results indicate the diverse formation processes of hot-Jupiters. Although it is difficult to determine the formation history of planets from C/O ratio only, our study have shown that investigation of chemical species in planetary atmospheres is important to probe planetary formations.

## 5.2 Summary of this thesis

Atmospheres of hot-Jupiters have been investigated intensively owing to the large planetary signal and interesting their physical properties. Hot-Jupiters are a class of exoplanets which does not exist in our solar system. Chemical compositions of planetary atmosphere will reflect the environment of the place where the planet grew. Chemical compositions also affect atmospheric structures strongly. Therefore, investigating the chemical compositions of atmosphere of hot-Jupiters is important to understand planetary formation and exoplanetary atmosphere. Owing to its high

temperature, UHJs are suitable targets to investigate chemical compositions. High resolution transmission spectroscopy is a powerful tool to characterize planetary atmospheres. Detrending and cross-correlation techniques enable us to detect weak signals of planetary atmospheres.

In chapter 3, we presented the result of transmission spectroscopy of HD149026b. HD149026b is a Saturn-sized gas giant discovered by Sato et al. (2005). The high density of HD149026b suggests the existence of a massive core. We detected the signal of neutral titanium and weak signal of neutral iron. The non-detection of TiO suggests the supersolar C/O ratio of the atmosphere of HD149026b. The supersolar C/O ratio suggests that the planet formed outside the water snowline and migrated to the current orbit. This study will add an important clue to understand the chemical compositions and formation history of hot-Jupiters.

In chapter 4, we presented the detection of TiO in the terminator region atmosphere of WASP-33b. TiO have been considered as a key molecule for a thermal inversion in the atmosphere of hot-Jupiters. Nevertheless, TiO had not been detected despite many attempts to search for TiO in the atmosphere of hot-Jupiters. WASP-33b is one of the hottest exoplanets ever discovered. Nugroho et al. (2017) reported TiO features in thermal emission spectrum of WASP-33b. However, there has been a problem that the signal became weak with updated line lists of TiO, though they were confirmed to be more accurate than old line lists. We detected TiO in the terminator region atmosphere by transmission spectroscopy with two accurate line lists. Given that Nugroho et al. (2017) detected emission features of TiO, there is thermal inversion and TiO exists widely in the atmosphere of WASP-33b.

Based on these results and previous studies of hot-Jupiters, we showed rich diversity of exoplanetary atmospheres. C/O ratio plays an important role in chemical compositions of planetary atmospheres. Abundance of metals and their compounds depends on temperature and C/O ratio, thus investigation of them is an effective method to study exoplanetary atmospheres. Our studies have established this methodology by high resolution transmission spectroscopy. This thesis would be helpful to characterize and understand diverse physical properties of atmospheres of hot-Jupiters.

## 5.3 Future Prospects

Since the signals of exoplanetary atmospheres are weak, it is difficult to study exoplanetary atmospheres. Owing to the large signals in both thermal emission spectroscopy and transmission spectroscopy, UHJs are suitable targets for characterization of exoplanetary atmospheres. Though the number of nearby UHJs is small, observations of their atmospheres will provide us the information of atmospheres of hot-Jupiters and possibly their formation processes. In the era of extremely large telescopes such as Thirty Meter Telescope, the number of targets will increase and we will be able to study atmospheres of many tens of hot-Jupiters statistically.

As described in Section 5.1, investigation of metal and their compounds is a powerful tool to study exoplanetary atmospheres. The comprehensive study of metal and their compounds in planetary atmospheres is a promising approach to investigate the properties of exoplanetary atmospheres (e.g, temperature, C/O ratio). In this thesis, we have only investigated TiO as metal compounds. TiO is one of the most important chemical species for the thermal structure of planetary atmospheres. Thus, the continuous upgrades or the new development of TiO line lists have been conducted, thus accurate line lists are already available (Plez-2012 and Toto, see the result of our check of the line list accuracy in Chapter 4). There are other interesting metal compounds which have a lot of absorption lines at visible wavelengths (e.g. VO, MgH). Although there are published line lists of them, it is not well known whether they are accurate enough for high resolution spectroscopy. We have checked the accuracy of TiO line lists by using a spectrum of an M-dwarf as a template. However, currently it is difficult to apply the same method for other metal compounds due to the lack of appropriate template spectra. Our studies show the importance of the check of line list accuracy and experimentally-derived line lists for high resolution spectroscopy. The improvement of line lists of metal compounds will enable us to study chemical compositions of exoplanetary atmospheres more comprehensively.

As shown in this thesis, high resolution spectroscopy is a fruitful approach for characterization of exoplanetary atmospheres. Especially in thermal emission spectroscopy, the light from the central star is one of the most significant noise sources to search for planetary signals. Recently, the combination of high contrast imaging (HCI) techniques and high resolution spectroscopy is receiving a lot of attentions. Owing to HCI techniques, the light from the central star is significantly suppressed at the position of the planet. This combination enables us to observe atmospheres of directly-imaged planets with high S/N. We have proceeded the REACH project, which combines SCExAO (Jovanovic et al. 2015) and IRD (Kotani et al. 2014) on the Subaru telescope (see Appendix A). This instrument is also helpful to understand the properties of planetary atmospheres.

# Appendix A

# REACH instrument

High resolution spectroscopy is a powerful tool to detect chemical species in the planetary atmosphere as shown in this thesis. Some extremely-stable high resolution spectrographs have been developed to search for low-mass planets by the radial velocity method: CARMENES at the Calar Alto Observatory (Quirrenbach et al. 2014), Subaru/IRD (Kotani et al. 2014), and VLT/ESPRESSO (Pepe et al. 2010). These spectrographs are also suitable instruments to characterize planetary atmospheres by high resolution spectroscopy. In addition, the combination of high dispersion spectroscopy and high contrast imaging technique is a promising approach to characterize planetary atmosphere. Snellen et al. (2014) firstly used this technique with VLT/CRIRES. Adaptive optics (AO) efficiently reduce the contamination by the central star and enable them to observe high resolution spectrum of the directly imaged planet $\beta$ Pic b.

 Rigorous Exoplanetary Atmosphere Characterization with High dispersion coronography (REACH)[1] is a powerful instrument on the Subaru telescope, which is a combination of SCExAO and IRD (Figure A.1). SCExAO is extreme-AO on the Subaru telescope (Jovanovic et al. 2015). Owing to the high contrast of SCExAO and the coronagraph, speckles at the position of the planet are effectively removed, which enables us to detect molecules in the planetary atmosphere easily. SCExAO also enables injection to single mode fiber (SMF) with high coupling efficiency (Jovanovic et al. 2017), which yields high spectral resolution (R $\sim$ 100000) and extremely stable spectroscopy without modal noise. I have developed the connection module of SCExAO and IRD (Figure A.2 and A.3). The light from the central star and the planet is injected to the multi-core single mode fiber at the fiber injection module in SCExAO. Now we assume that the planet light is injected to the central fiber, and star light is

---

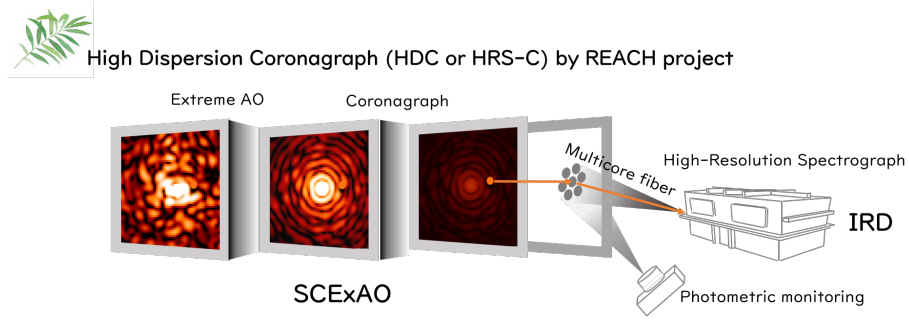[1]http://secondearths.sakura.ne.jp/reach/

**Figure A.1**: Configurations of REACH instrument. SCExAO effectively compensates the wavefront error of incoming light and reduces speckles at the position of the planet. The light from the planet is injected to the single mode fiber leading to IRD. This figure is taken from the web site of REACH.

injected to any of the outside fibers. Since IRD has only two input fibers, we need to switch the fibers leading to IRD. Our switch-yard can connect any of seven output fibers of the multi core fiber to the two fibers leading to IRD. 90 % of light is coupled to IRD, and 10 % of light is coupled to multi mode fiber (MMF) by a beam splitter. Other five output fibers of the multi core fibers are also coupled to MMFs. Output of MMFs are photometrically monitored by another detector, which will be used for real-time speckle nulling and optimization of fiber injection efficiency.

The combination of large telescope diameter (8.2 m), extreme-AO, and extremely stable high-dispersion spectrograph is unique in the world. REACH can probe atmospheres of directly imaged planets which orbit near the star (e.g., HR8799e). Possible target molecules are $CH_4$, CO, HCN, or $NH_3$. For example, we might be able to use $CH_4$, CO, and $NH_3$ as tracers for non-equilibrium chemistry. The abundance of HCN strongly depends on the C/O ratio of the atmosphere, thus HCN might work as a tracer of C/O ratio of planetary atmospheres. REACH can be used in the open use of the Subaru telescope from the S20B semester. REACH will be useful to gain more insight of diverse atmospheric properties of exoplanets.
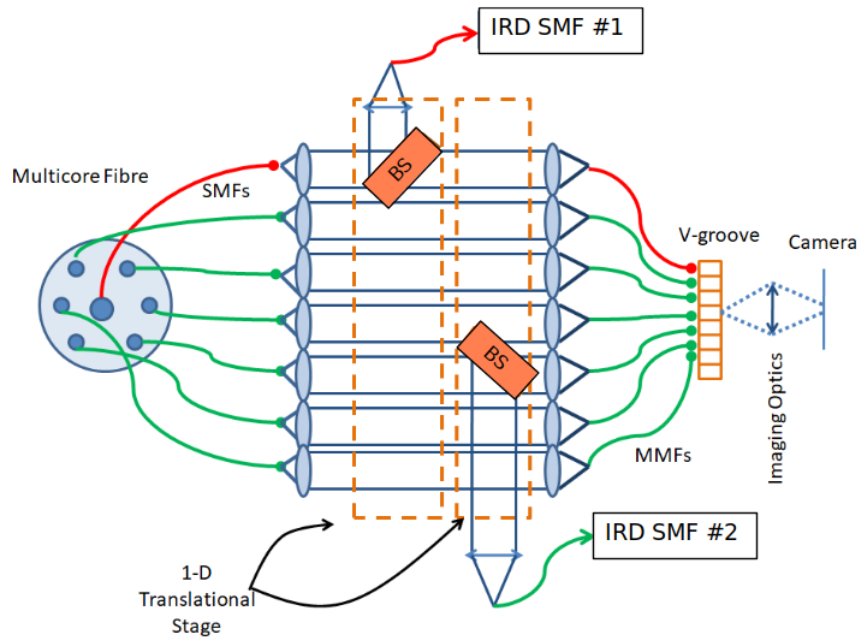
**Figure A.2**: Schematic view of the switch-yard for the connection of SCExAO and IRD. BS means the beam splitter.
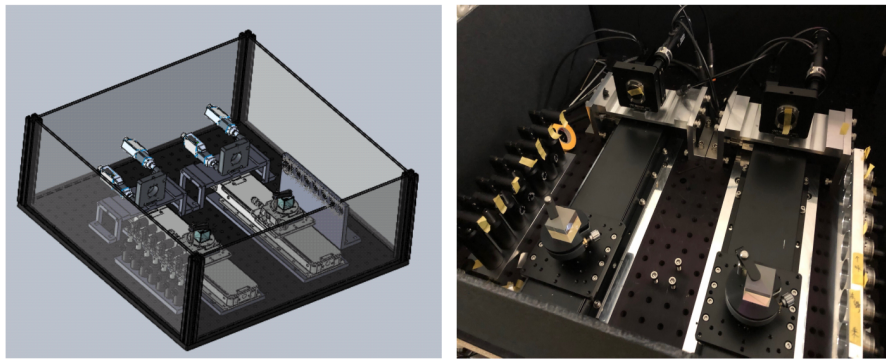


**Figure A.3**: (left) 3D CAD design of the switch-yard. (right) a picture of the switch-yard taken at the IR Nasmyth focus of the Subaru telescope.

# References

Ali-Dib, M., Mousis, O., Petit, J.-M., & Lunine, J. I. 2014, ApJ, 785, 125

Alonso-Floriano, F. J., Sánchez-López, A., Snellen, I. A. G., et al. 2019, A&A, 621, A74

Arcangeli, J., Désert, J.-M., Line, M. R., et al. 2018, ApJ, 855, L30

Baba, H., Yasuda, N., Ichikawa, S.-I., et al. 2002, in Astronomical Society of the Pacific Conference Series, Vol. 281, Astronomical Data Analysis Software and Systems XI, ed. D. A. Bohlender, D. Durand, & T. H. Handley, 298

Baglin, A., Auvergne, M., Barge, P., et al. 2006, in ESA Special Publication, Vol. 1306, The CoRoT Mission Pre-Launch Status - Stellar Seismology and Planet Finding, ed. M. Fridlund, A. Baglin, J. Lochard, & L. Conroy, 33

Ballard, S., Fabrycky, D., Fressin, F., et al. 2011, ApJ, 743, 200

Barklem, P. S., & Collet, R. 2016, A&A, 588, A96

Bate, M. R., Lubow, S. H., Ogilvie, G. I., & Miller, K. A. 2003, MNRAS, 341, 213

Batygin, K., Bodenheimer, P. H., & Laughlin, G. P. 2016, ApJ, 829, 114

Ben-Yami, M., Madhusudhan, N., Cabot, S. H. C., et al. 2020, arXiv e-prints, arXiv:2006.05995

Bento, J., Wheatley, P. J., Copperwheat, C. M., et al. 2014, MNRAS, 437, 1511

Birkby, J. L., de Kok, R. J., Brogi, M., et al. 2013, MNRAS, 436, L35

Birkby, J. L., de Kok, R. J., Brogi, M., Schwarz, H., & Snellen, I. A. G. 2017, AJ, 153, 138

Boley, A. C., Granados Contreras, A. P., & Gladman, B. 2016, ApJ, 817, L17

## REFERENCES

Bonomo, A. S., Desidera, S., Benatti, S., et al. 2017, A&A, 602, A107

Borucki, W. J., Koch, D., Basri, G., et al. 2010, Science, 327, 977

Brewer, J. M., & Fischer, D. A. 2016, ApJ, 831, 20

Brewer, J. M., Fischer, D. A., & Madhusudhan, N. 2017, AJ, 153, 83

Brogi, M., de Kok, R. J., Birkby, J. L., Schwarz, H., & Snellen, I. A. G. 2014, A&A, 565, A124

Brogi, M., Giacobbe, P., Guilluy, G., et al. 2018, A&A, 615, A16

Brogi, M., Snellen, I. A. G., de Kok, R. J., et al. 2012, Nature, 486, 502

Brogi, M., Snellen, I. A. G., de Kok, R. J., et al. 2013, ApJ, 767, 27

Burrows, A., & Sharp, C. M. 1999, ApJ, 512, 843

Butler, R. P., Wright, J. T., Marcy, G. W., et al. 2006, ApJ, 646, 505

Cabot, S. H. C., Madhusudhan, N., Hawker, G. A., & Gandhi, S. 2019, MNRAS, 482, 4422

Casasayas-Barris, N., Pallé, E., Yan, F., et al. 2018, A&A, 616, A151

—. 2019, A&A, 628, A9

Chakrabarty, A., & Sengupta, S. 2019, AJ, 158, 39

Charbonneau, D., Brown, T. M., Latham, D. W., & Mayor, M. 2000, ApJ, 529, L45

Charbonneau, D., Brown, T. M., Noyes, R. W., & Gilliland, R. L. 2002, ApJ, 568, 377

Charbonneau, D., Allen, L. E., Megeath, S. T., et al. 2005, ApJ, 626, 523

Coelho, P., Barbuy, B., Meléndez, J., Schiavon, R. P., & Castilho, B. V. 2005, A&A, 443, 735

Collier Cameron, A., Guenther, E., Smalley, B., et al. 2010, MNRAS, 407, 507

Cooper, C. S., & Showman, A. P. 2006, ApJ, 649, 1048

Dalgarno, A., & Williams, D. A. 1962, ApJ, 136, 690

D'Angelo, G., & Bodenheimer, P. 2016, ApJ, 828, 33

REFERENCES

D'Angelo, G., Kley, W., & Henning, T. 2003, ApJ, 586, 540

de Kok, R. J., Brogi, M., Snellen, I. A. G., et al. 2013, A&A, 554, A82

Deming, D., Seager, S., Richardson, L. J., & Harrington, J. 2005, Nature, 434, 740

Deming, D., Wilkins, A., McCullough, P., et al. 2013, ApJ, 774, 95

Diamond-Lowe, H., Stevenson, K. B., Bean, J. L., Line, M. R., & Fortney, J. J. 2014, ApJ, 796, 66

Ehrenreich, D., Lovis, C., Allart, R., et al. 2020, Nature, 1

Endl, M., Caldwell, D. A., Barclay, T., et al. 2014, ApJ, 795, 151

Espinoza, N., Rackham, B. V., Jordán, A., et al. 2019, MNRAS, 482, 2065

Esteves, L. J., de Mooij, E. J. W., Jayawardhana, R., Watson, C., & de Kok, R. 2017, AJ, 153, 268

Evans, T. M., Sing, D. K., Kataria, T., et al. 2017, nat, 548, 58

Fabrycky, D., & Tremaine, S. 2007, ApJ, 669, 1298

Fischer, D. A., Laughlin, G., Butler, R. P., et al. 2004, arXiv e-prints, astro

Fortney, J. J., Lodders, K., Marley, M. S., & Freedman, R. S. 2008, ApJ, 678, 1419

Gibson, N. P., Aigrain, S., Barstow, J. K., et al. 2013, MNRAS, 436, 2974

Gibson, N. P., Merritt, S., Nugroho, S. K., et al. 2020, MNRAS, 493, 2215

Grimm, S. L., & Heng, K. 2015, ApJ, 808, 182

Hansen, C. J., Schwartz, J. C., & Cowan, N. B. 2014, MNRAS, 444, 3632

Hawker, G. A., Madhusudhan, N., Cabot, S. H. C., & Gandhi, S. 2018, ApJ, 863, L11

Hayashi, C., Nakazawa, K., & Nakagawa, Y. 1985, in Protostars and Planets II, ed. D. C. Black & M. S. Matthews, 1100–1153

Haynes, K., Mandell, A. M., Madhusudhan, N., Deming, D., & Knutson, H. 2015, ApJ, 806, 146

Hébrard, G., Collier Cameron, A., Brown, D. J. A., et al. 2013, A&A, 549, A134

Helling, C. 2019, Annual Review of Earth and Planetary Sciences, 47, 583

## REFERENCES

Herman, M. K., de Mooij, E. J. W., Jayawardhana, R., & Brogi, M. 2020, arXiv e-prints, arXiv:2006.10743

Hirano, T., Gaidos, E., Winn, J. N., et al. 2020, ApJ, 890, L27

Hoeijmakers, H. J., de Kok, R. J., Snellen, I. A. G., et al. 2015, A&A, 575, A20

Hoeijmakers, H. J., Ehrenreich, D., Heng, K., et al. 2018, Nature, 560, 453

Hoeijmakers, H. J., Ehrenreich, D., Kitzmann, D., et al. 2019, A&A, 627, A165

Holman, M., Touma, J., & Tremaine, S. 1997, Nature, 386, 254

Holman, M. J., Fabrycky, D. C., Ragozzine, D., et al. 2010, Science, 330, 51

Howard, A. W., Marcy, G. W., Johnson, J. A., et al. 2010, Science, 330, 653

Howell, S. B., Sobeck, C., Haas, M., et al. 2014, PASP, 126, 398

Hubeny, I., Burrows, A., & Sudarsky, D. 2003, ApJ, 594, 1011

Husser, T. O., Wende-von Berg, S., Dreizler, S., et al. 2013, A&A, 553, A6

Ikoma, M., Guillot, T., Genda, H., Tanigawa, T., & Ida, S. 2006, ApJ, 650, 1150

Ikoma, M., Nakazawa, K., & Emori, H. 2000, ApJ, 537, 1013

Irwin, J. B. 1959, AJ, 64, 149

John, T. L. 1988, A&A, 193, 189

Jovanovic, N., Martinache, F., Guyon, O., et al. 2015, PASP, 127, 890

Jovanovic, N., Schwab, C., Guyon, O., et al. 2017, A&A, 604, A122

Kanagawa, K. D., Muto, T., Okuzumi, S., et al. 2018, ApJ, 868, 48

Kataria, T., Sing, D. K., Lewis, N. K., et al. 2016, apj, 821, 9

Kitzmann, D., Heng, K., Rimmer, P. B., et al. 2018, ApJ, 863, 183

Knutson, H. A., Charbonneau, D., Allen, L. E., Burrows, A., & Megeath, S. T. 2008, ApJ, 673, 526

Knutson, H. A., Howard, A. W., & Isaacson, H. 2010, ApJ, 720, 1569

Kopparapu, R. k., Kasting, J. F., & Zahnle, K. J. 2012, ApJ, 745, 77

REFERENCES

Kotani, T., Tamura, M., Suto, H., et al. 2014, in Society of Photo-Optical Instrumentation Engineers (SPIE) Conference Series, Vol. 9147, procspie, 914714

Kozai, Y. 1962, AJ, 67, 591

Kreidberg, L. 2015, PASP, 127, 1161

Kreidberg, L., Line, M. R., Parmentier, V., et al. 2018, AJ, 156, 17

Kurucz, R. L. 1970, SAO Special Report, 309

—. 2018, Astronomical Society of the Pacific Conference Series, Vol. 515, Including All the Lines: Data Releases for Spectra and Opacities through 2017, 47

Kuzuhara, M., Tamura, M., Kudo, T., et al. 2013, ApJ, 774, 11

Lagrange, A. M., Bonnefoy, M., Chauvin, G., et al. 2010, Science, 329, 57

Lépine, S., Hilton, E. J., Mann, A. W., et al. 2013, AJ, 145, 102

Lidov, M. L. 1962, Planet. Space Sci., 9, 719

Lin, D. N. C., & Papaloizou, J. 1986, ApJ, 309, 846

Line, M. R., Knutson, H., Wolf, A. S., & Yung, Y. L. 2014, ApJ, 783, 70

Line, M. R., Liang, M. C., & Yung, Y. L. 2010, ApJ, 717, 496

Lissauer, J. J., Marcy, G. W., Rowe, J. F., et al. 2012, ApJ, 750, 112

Lothringer, J. D., & Barman, T. 2019, ApJ, 876, 69

Maciejewski, G., Fernández, M., Aceituno, F., et al. 2018, Acta Astronomica, 68, 371

Madhusudhan, N. 2012, ApJ, 758, 36

Madhusudhan, N., Amin, M. A., & Kennedy, G. M. 2014a, ApJ, 794, L12

Madhusudhan, N., Knutson, H., Fortney, J. J., & Barman, T. 2014b, in Protostars and Planets VI, ed. H. Beuther, R. S. Klessen, C. P. Dullemond, & T. Henning, 739

Madhusudhan, N., & Seager, S. 2009, ApJ, 707, 24

Mansfield, M., Bean, J. L., Line, M. R., et al. 2018, AJ, 156, 10

Marois, C., Macintosh, B., Barman, T., et al. 2008, Science, 322, 1348

*REFERENCES*

Marois, C., Zuckerman, B., Konopacky, Q. M., Macintosh, B., & Barman, T. 2010, Nature, 468, 1080

Mayor, M., & Queloz, D. 1995, Nature, 378, 355

Mayor, M., Pepe, F., Queloz, D., et al. 2003, The Messenger, 114, 20

Mazeh, T., Tamuz, O., & Zucker, S. 2007, Astronomical Society of the Pacific Conference Series, Vol. 366, The Sys-Rem Detrending Algorithm: Implementation and Testing, ed. C. Afonso, D. Weldrake, & T. Henning, 119

Mbarek, R., & Kempton, E. M.-R. 2016, The Astrophysical Journal, 827, 121

McKemmish, L. K., Masseron, T., Hoeijmakers, H. J., et al. 2019, Monthly Notices of the Royal Astronomical Society, 488, 2836

Merritt, S. R., Gibson, N. P., Nugroho, S. K., et al. 2020, arXiv e-prints, arXiv:2002.02795

Mizuno, H. 1980, Progress of Theoretical Physics, 64, 544

Molaverdikhani, K., Helling, C., Lew, B. W. P., et al. 2020, A&A, 635, A31

Moses, J. I., Madhusudhan, N., Visscher, C., & Freedman, R. S. 2013, ApJ, 763, 25

Moses, J. I., Visscher, C., Fortney, J. J., et al. 2011, ApJ, 737, 15

Nagasawa, M., Ida, S., & Bessho, T. 2008, ApJ, 678, 498

Naoz, S., Farr, W. M., Lithwick, Y., Rasio, F. A., & Teyssandier, J. 2011, Nature, 473, 187

Narita, N., Sato, B., Hirano, T., & Tamura, M. 2009, PASJ, 61, L35

Narita, N., Suto, Y., Winn, J. N., et al. 2005, PASJ, 57, 471

Narita, N., Takahashi, Y. H., Kuzuhara, M., et al. 2012, PASJ, 64, L7

Noguchi, K., Aoki, W., Kawanomoto, S., et al. 2002, PASJ, 54, 855

Nugroho, S. K., Gibson, N. P., de Mooij, E. J. W., et al. 2020, arXiv e-prints, arXiv:2003.04856

Nugroho, S. K., Kawahara, H., Gibson, N. P., de Mooij, E. J. W., & Watson, C. A. 2019, High-resolution TiO signature in the emission spectrum of WASP-33b: New result using updated TiO line lists, Poster Presentation in Exoclimes

REFERENCES

Nugroho, S. K., Kawahara, H., Masuda, K., et al. 2017, AJ, 154, 221

Öberg, K. I., Murray-Clay, R., & Bergin, E. A. 2011, ApJ, 743, L16

O'Donovan, F. T., Charbonneau, D., Harrington, J., et al. 2010, ApJ, 710, 1551

Pál, A., Bakos, G. Á., Torres, G., et al. 2008, ApJ, 680, 1450

Parmentier, V., Showman, A. P., & Lian, Y. 2013, A&A, 558, A91

Parmentier, V., Line, M. R., Bean, J. L., et al. 2018, A&A, 617, A110

Pepe, F. A., Cristiani, S., Rebolo Lopez, R., et al. 2010, in Society of Photo-Optical Instrumentation Engineers (SPIE) Conference Series, Vol. 7735, Proc. SPIE, 77350F

Pepper, J., Pogge, R. W., DePoy, D. L., et al. 2007, PASP, 119, 923

Piette, A. A. A., Madhusudhan, N., McKemmish, L. K., et al. 2020, arXiv e-prints, arXiv:2006.04807

Pino, L., Désert, J.-M., Brogi, M., et al. 2020, ApJ, 894, L27

Plez, B. 1998, A&A, 337, 495

Pollacco, D. L., Skillen, I., Collier Cameron, A., et al. 2006, PASP, 118, 1407

Pollack, J. B., Hubickyj, O., Bodenheimer, P., et al. 1996, Icarus, 124, 62

Queloz, D., Eggenberger, A., Mayor, M., et al. 2000, A&A, 359, L13

Quirrenbach, A., Amado, P. J., Caballero, J. A., et al. 2014, in Society of Photo-Optical Instrumentation Engineers (SPIE) Conference Series, Vol. 9147, Proc. SPIE, 91471F

Rafikov, R. R. 2005, ApJ, 621, L69

Rasio, F. A., & Ford, E. B. 1996, Science, 274, 954

Ricker, G. R., Winn, J. N., Vanderspek, R., et al. 2015, Journal of Astronomical Telescopes, Instruments, and Systems, 1, 014003

Sánchez-López, A., Alonso-Floriano, F. J., López-Puertas, M., et al. 2019, A&A, 630, A53

Sato, B., Kambe, E., Takeda, Y., Izumiura, H., & Ando, H. 2002, PASJ, 54, 873

REFERENCES

Sato, B., Fischer, D. A., Henry, G. W., et al. 2005, ApJ, 633, 465

Schreier, F., Gimeno García, S., Hochstaffl, P., & Städt, S. 2019, Atmosphere, 10, 262

Schwarz, H., Brogi, M., de Kok, R., Birkby, J., & Snellen, I. 2015, A&A, 576, A111

Schwenke, D. W. 1998, Faraday Discussions, 109, 321

Sedaghati, E., Boffin, H. M. J., MacDonald, R. J., et al. 2017, Nature, 549, 238

Sharp, C. M., & Burrows, A. 2007, The Astrophysical Journal Supplement Series, 168, 140

Sheppard, K. B., Mandell, A. M., Tamburo, P., et al. 2017, ApJ, 850, L32

Sing, D. K., Lecavelier des Etangs, A., Fortney, J. J., et al. 2013, MNRAS, 436, 2956

Sing, D. K., Lavvas, P., Ballester, G. E., et al. 2019, AJ, 158, 91

Snellen, I. A. G., Brandl, B. R., de Kok, R. J., et al. 2014, Nature, 509, 63

Snellen, I. A. G., de Kok, R. J., de Mooij, E. J. W., & Albrecht, S. 2010, Nature, 465, 1049

Spiegel, D. S., Silverio, K., & Burrows, A. 2009, ApJ, 699, 1487

Stassun, K. G., Collins, K. A., & Gaudi, B. S. 2017, AJ, 153, 136

Steffen, J. H., & Agol, E. 2005, MNRAS, 364, L96

Stock, J. W., Kitzmann, D., Patzer, A. B. C., & Sedlmayr, E. 2018, MNRAS, 479, 865

Tajitsu, A., Aoki, W., Kawanomoto, S., & Narita, N. 2010, Publications of the National Astronomical Observatory of Japan, 13, 1

Tamuz, O., Mazeh, T., & Zucker, S. 2005, MNRAS, 356, 1466

Todorov, K., Deming, D., Harrington, J., et al. 2010, ApJ, 708, 498

Toomre, A. 1964, ApJ, 139, 1217

Turner, J. D., de Mooij, E. J. W., Jayawardhana, R., et al. 2020, ApJ, 888, L13

Valenti, J. A., Butler, R. P., & Marcy, G. W. 1995, PASP, 107, 966

*REFERENCES*

Venot, O., Hébrard, E., Agúndez, M., et al. 2012, A&A, 546, A43

Vogt, S. S., Marcy, G. W., Butler, R. P., & Apps, K. 2000, ApJ, 536, 902

Wakeford, H. R., & Sing, D. K. 2015, A&A, 573, A122

Watson, C. A., & Marsh, T. R. 2010, MNRAS, 405, 2037

Wheatley, P. J., Collier Cameron, A., Harrington, J., et al. 2010, arXiv e-prints, arXiv:1004.0836

Winn, J. N., Johnson, J. A., Albrecht, S., et al. 2009, ApJ, 703, L99

Winn, J. N., Suto, Y., Turner, E. L., et al. 2004, PASJ, 56, 655

Wolf, A. S., Laughlin, G., Henry, G. W., et al. 2007, ApJ, 667, 549

Wong, I., Knutson, H. A., Kataria, T., et al. 2016, ApJ, 823, 122